Automatic Optimization of Treatment Dosimetry to Improve Visual Outcomes in Episcleral Plaque Brachytherapy

by

Gawon Han

A thesis submitted in partial fulfillment of the requirements for the degree of

Master of Science

in

Medical Physics

Department of Oncology
University of Alberta

Abstract

Ocular plaque brachytherapy is an effective treatment option for medium-sized ocular melanomas, showing equivalent survival relative to enucleation, while providing added benefits of eye preservation and possible vision retention. Currently the treatment planning system for plaque brachytherapy, known as Plaque Simulator, generates treatment plans using uniform seed strengths which requires the planner to modify the plan by manually adjusting the seed strengths and locations to reduce doses to the critical structures while maintaining the desired tumor coverage. This demands planning expertise, can be time-consuming, and may not always provide the best possible plan. To overcome these challenges, this thesis applies an automated dose optimization algorithm, known as simulated annealing (SA) algorithm, to inverse plan plaque brachytherapy treatments. Firstly, the SA algorithm was verified by solving two problems: 1) dose optimization using uniform loading, and 2) maximizing dose uniformity across tumor base with differential loading. The first problem allowed to verify the correct implementation of the tumor and seed geometry, dose calculation, and the general steps of the SA algorithm. Using the SA algorithm, uniform seed strengths to deliver the prescription dose to tumor apex were obtained and were manually input into Plaque Simulator to compare the resulting dose to apex for various tumor and plaque sizes. The difference in dose to apex between the two systems were found to agree within 4.5% for all scenarios and arises due to the differences in the TG-43 dosimetry parameters and seed coordinates used in both systems. The second problem evaluated the potential of the algorithm to find minima in the energy function using differential seed strengths. The algorithm from the first problem was modified to find differential seed strengths that can maximize dose uniformity across the tumor base. Averaging over different plaque sizes, the reduction in basal dose variation for 3.5, 5, and 8 mm heights from using uniform strengths, were found to be 33.1%, 33.3%, and 27.1%, respectively. Lastly, the problem of finding differential seed strengths to reduce doses to the critical structures while maintaining desired tumor coverage was investigated. The SA algorithm was used to reduce dose to a single point of interest (POI), and then two POIs representative of critical structures; the algorithm was found to be able to reduce doses, to a degree that depends on the tumor and plaque size used. The algorithm was then further developed to handle shifted plaques and elliptical tumor base shapes in its modelling, which have been verified by benchmarking each feature as well as the two together in optimization. Moreover, by applying the algorithm to numerous clinical scenarios, it was verified that implementing the developed optimization routine into clinical cases is practical.

Preface

This project was supervised by Dr. G. Menon (primary supervisor) and Dr. M. Larocque (co-supervisor). I was responsible for the data collection and analysis for Chapters 3 and 4. G. Menon and M. Larocque assisted with development of the algorithms, data interpretation, and provided editorial comments. Components of Chapter 3 were published as the Research Day abstract: G. Han, M. Larocque, E Weis, and G. Menon, "Automatic optimization of treatment dosimetry to improve visual outcomes in episcleral plaque brachytherapy," *Ophthalmology & Visual Sciences Research Day*, p. 15 (2018), and also as the conference abstract: G. Han, M. Larocque, and G. Menon, "Automatic optimization of treatment dosimetry to improve visual outcomes in episcleral plaque brachytherapy," *Journal of the European Society for Radiotherapy and Oncology*, vol. 129, Suppl 1, S78-S79 (2018). Components of Chapter 4 were published as the Research Day abstract: G. Han, M. Larocque, E Weis, and G. Menon, "Automatic optimization of treatment dosimetry to improve visual outcomes in episcleral plaque brachytherapy," *Ophthalmology & Visual Sciences Research Day*, p. 9 (2019).

The fundus images of choroidal melanoma patients were used with ethics approval by the Health Research Ethics Board of Alberta (HREBA) Cancer Committee, Project Name: "Preclinical evaluation of heterogeneity corrections in brachytherapy treatment planning," Project Number: HREBA.CC-16-0657.

Acknowledgements

I would like to acknowledge and sincerely thank my primary supervisor, Dr. Geetha Menon, and co-supervisor, Dr. Matthew Larocque, for their excellent guidance, insight, patience and encouragement throughout this project. I would like to thank Dr. Menon for her supervision in every possible way, always willing to offer help, and providing me with many advices and opportunities to learn throughout the program. I also want to thank Dr. Larocque for his help in developing the algorithms, familiarizing with Plaque Simulator, and providing lots of insightful comments in all aspects of this project. Their supervision was far beyond what I expected and this work would have not been possible without their support.

I would also like to acknowledge and thank my supervisory committee, Dr. Ezekiel Weis and Dr. Gino Fallone, for their guidance and support. I want to thank Dr. Weis for contributing to this work by providing many helpful comments, inviting me into the operating room to watch the plaque insertion, and being encouraging and excited about various parts of this project. I am also grateful to Dr. Fallone for providing lots of great comments during the presentations. I also want to thank Dr. Don Robinson for being my "arms-length" examiner.

I also want to thank others who helped with various components of this project; Dr. Terence Riauka for sharing his ideas about re-injection of heat in simulated annealing, and Dr. Hali Morrison for always being available to answer my questions related to dose uncertainty and Plaque Simulator. Also, I would like to thank the medical physicists and the students in this department; to the physicists for instructing my courses and labs, and to Hongwei Sun, Braden Chow, Aaron Purchase, and many others for making this an enjoyable journey.

I would also like to acknowledge the financial support for this project, including the Mark Marshall Department of Ophthalmology and Visual Sciences Translational Research Award and travel awards from the Canadian Organization of Medical Physicists and the University of Alberta. These sources of funding allowed me to focus on research and to present part of this work at conferences.

Lastly, I would like to thank my family and friends for always being there for me, supporting me through every step, helping me endure stressful times, and celebrating successes together.

Table of Contents

List of Figures

List of Tables

List of Abbreviations

AAPM	American Association of Physicists in Medicine
ABS	American Brachytherapy Society
CCI	Cross Cancer Institute
CLRP	Carleton Laboratory for Radiotherapy Physics
COMS	Collaborative Ocular Melanoma Study
CT	Computed tomography
EBRT	External beam radiotherapy
GTV	Gross tumor volume
HR	Heat re-injection
MBDCA	Model-based dose calculation algorithm
MC	Monte Carlo
MCNP	Monte Carlo N-Particle
MRI	Magnetic resonance imaging
POI	Point of interest
PTV	Planning target volume
ROPES	Radiation Oncology Physics and Engineering Services
SA	Simulated annealing
TG	Task group
TPS	Treatment planning system
TTT	Transpupillary thermotherapy

Chapter 1 Introduction

1.1 Ocular cancers

According to the Canadian Cancer Society, cancer is the leading cause of death in Canada, with nearly 1 in 2 people expected to be diagnosed with cancer during their lifetime and 1 in 4 people dying from it [1]. Ocular cancers comprise only a small portion of this statistic, with an incidence rate of approximately 6 cases per million person-years [2]. Nevertheless, ocular tumors are potentially life threatening due to local failures or metastatic spread [3]. Ocular tumors present a therapeutic challenge due to the sensitive tissues involved and the necessity to eradicate the tumor while minimizing visual loss [3]. Hence treatments for these tumors are often aimed at conserving the eye with as much useful vision as possible while minimizing any risk to life [3].

1.1.1 Anatomy of the eye

The globe of the eye is made up of three layers: the outermost layer consists of the cornea and the sclera, the middle layer is the uvea, and the innermost layer is the retina (Figure 1.1) [4]. Though the cornea and sclera are extensions of the same layer of tissue, they have separately distinct functions. The cornea is a transparent dome-shaped tissue that functions as a window and allows light to enter the eye. It protects the pupil, the iris, and the inside of the eye from penetration by foreign bodies and is the first and most powerful element in the eye's focusing system. As light passes through the cornea, it is partially refracted before reaching the lens. The curvature of the cornea, which is spherical during infancy and changes with age, gives it focusing power. The sclera, which is essentially the backward continuation of the cornea, is a tough white outer coating of fibrous tissue that covers the entire eyeball except for the cornea to provide a firm protection of the eyeball. The muscles that move the eye are also attached to the sclera. The uvea consists of the choroid, the ciliary body, and the iris. The choroid, which is the posterior part of the uvea, is a layer of blood vessels and connective tissue sandwiched between the sclera and the retina. It supplies blood and nutrients to the retina and nourishes all of the other structures within the eye. The ciliary body, which is the forward continuation of the choroid, includes the ciliary muscles and the ciliary epithelium. The ciliary muscles are attached to the lens and contract or relax to change the lens shape and curvature, and the ciliary epithelium secretes the fluid, aqueous humor, in the eye. The most anterior portion of the uvea is the iris. It is a ring-shaped membrane that surrounds an opening in the center, the pupil. The iris contains muscles that allow the pupil to dilate and constrict to regulate the amount of light that enters the eye.

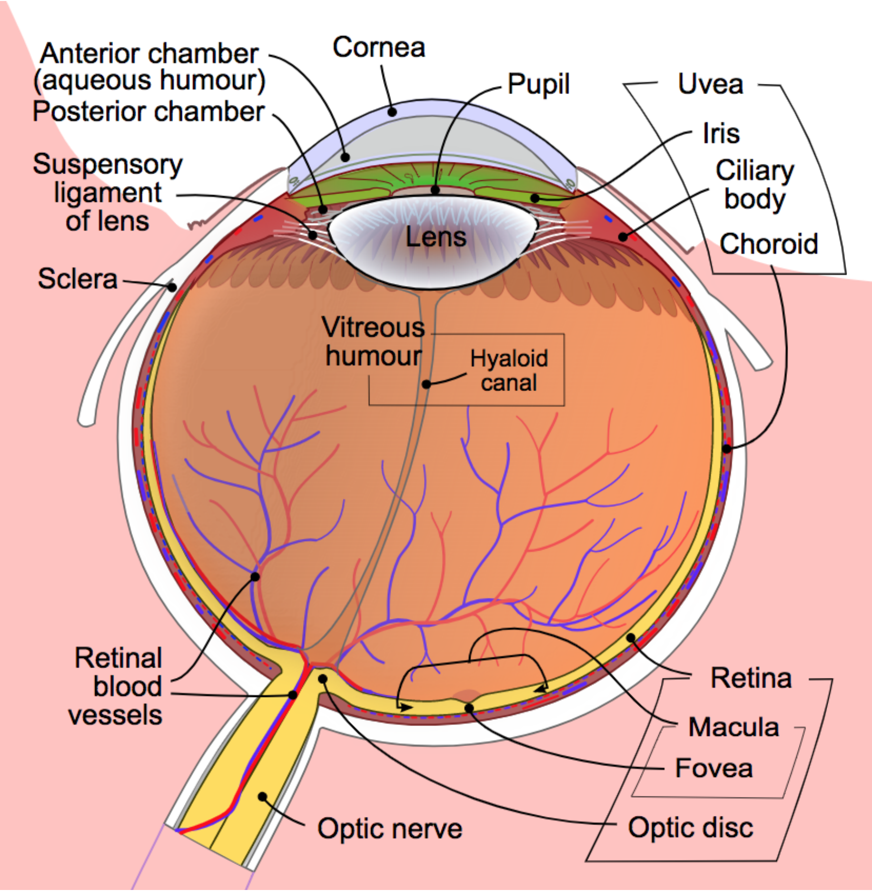

Figure 1.1 Diagram of the human right eye (figure from https://en.wikipedia.org/wiki/Eye).

The retina is the light-sensitive tissue that lines the inside surface of the eye. Cells in the retina convert incoming light into electrical impulses and these electrical impulses are carried by the optic nerve to the brain, which finally interprets them as visual images. The macula is the small sensitive area in the center of the retina that is responsible for clear central vision. The fovea is located in the center of the macula and allows visual resolution of objects with the highest level of detail. The optic disc, also known as the optic nerve head, is a small region within the retina in which there are no photoreceptors; hence there is no image detection in this area. It represents the beginning of the optic nerve, which carries sensory nerve impulses from the ganglion cells of the retina toward the visual centres in the brain. The vast majority of optic nerve fibres convey information regarding central vision. Within the cavities enclosed by the three layers of the eyeball, there are the aqueous humor, the lens behind the iris, and the vitreous body, which fills the large cavity behind the lens and iris. The lens is composed of transparent, flexible tissue that can change its curved shape to focus on both close and far objects. Together with the cornea, the lens helps to focus light and images on the retina.

1.1.2 Types of ocular cancers

Ocular cancers can be classified into two types: intraocular and conjunctival [3,5]. Intraocular tumors include uveal melanoma (arising in the iris, choroid, or ciliary body), the most common malignant primary tumor, and other types such as retinoblastoma and lymphoma. Uveal melanoma develops from melanocytes, the cells in the eye that produce the pigment melanin [5]. 80% of uveal melanomas form in the choroid, while 12% form in the ciliary body, and 8% in the iris [6]. The overall 5-year survival rate for uveal melanoma is 62% but varies based on tumor size and other prognostic factors including cell type, location of the anterior margin of the tumor, and degree of ciliary body involvement [7,8]. Lymphoma is the second most common type of ocular cancer and it arises from lymphocytes, a type of white blood cell that fights viruses, bacteria, or abnormal cells including cancer cells [5]. The overall 5-year survival rate for patients with lymphoma is 69% [8]. Retinoblastoma is the most common ocular cancer in children, which starts in the cells of the retina [5]. Though the overall 5-year survival rate for children with retinoblastoma is 95%, it depends on several factors including whether the cancer has metastasized from the eye to other parts of the body [8].

1.1.3 Types of treatments

The primary treatment method for cancer includes surgery, chemotherapy, and radiation therapy, which can be used in combination or independently depending on the clinical scenario [9]. Primary management of ocular cancers includes observation, surgery, radiation therapy, and transpupillary thermotherapy (TTT) [10].

Surgical resection in the case of ocular cancers involves either the removal of parts or all of the affected eye (enucleation) depending on the size and spread of the tumor [10]. Enucleation is appropriate for patients with a large tumor (>18 mm in diameter and 10 mm in thickness), a blind painful eye, tumors that surround or invade the optic nerve head, or eyes with neovascular glaucoma [11,12]. Local resection is suitable for iris melanomas, select ciliary body melanomas, or small anterior choroidal melanomas [13]. Although local resection is aimed at conserving the eye and useful vision while removing the tumor, several studies have found higher local recurrence rates with transscleral resection than with brachytherapy or enucleation [14,15,16].

Radiation therapy, which utilizes ionizing radiation (mainly high-energy photons, protons, or electrons) to destroy cancer cells, can be delivered in two ways: external beam radiotherapy (EBRT) or brachytherapy. EBRT, the more common type of radiation treatment, delivers radiation from outside the body using machines such as linear accelerators, while brachytherapy delivers radiation using small radioactive sources or electronic x-ray sources placed inside or near the tumor. Typically, ocular cancers are treated using photons and protons for EBRT, and plaques loaded with radioactive sources for brachytherapy treatments. Brachytherapy has a strong advantage over EBRT as it allows radioactive sources to be placed in close proximity to the tumor thereby delivering highly concentrated dose to small areas with a quick dose fall-off in the surrounding normal tissues. These characteristics of brachytherapy make it a suitable treatment option for ocular cancers that are relatively small in area with several surrounding critical structures (such as optic nerve, lens, iris). Details of the development of ocular plaque brachytherapy are discussed in the next section.

TTT is a treatment that delivers infrared light through the pupil using a diode laser to heat and kill the tumor [17,18]. Long-term results of TTT as a primary therapy have been poor, with poor local control rates, visual outcomes, and the long-term possibility of recurrence with high metastatic risk [19,20]. Thus, it is mainly used as an adjuvant treatment after brachytherapy as the two treatments are complementary: TTT is most effective at the apex of the tumor and brachytherapy is most effective at the base [17,19 ,21].

1.2 Ocular plaque brachytherapy

Up until 1980s, enucleation was the most common management of ocular melanomas [22]. However, in 1985, the Collaborative Ocular Melanoma Study (COMS) group provided the first standardized methods for performing plaque brachytherapy for treatments of ocular melanomas [23]. A 12-year follow-up study conducted by the same group demonstrated that survival rate of patients treated with plaque brachytherapy was no different from that of enucleation [24]. With its added benefits of eye preservation and possible vision retention, plaque brachytherapy gained favor and started to be used more commonly than enucleation. In plaque brachytherapy, a metal disc (or plaque) with radioactive seeds is surgically sutured in close proximity to the tumor on the external surface of the eye to irradiate the tumor for a predetermined time period to deliver the required treatment dose (Figure 1.2).

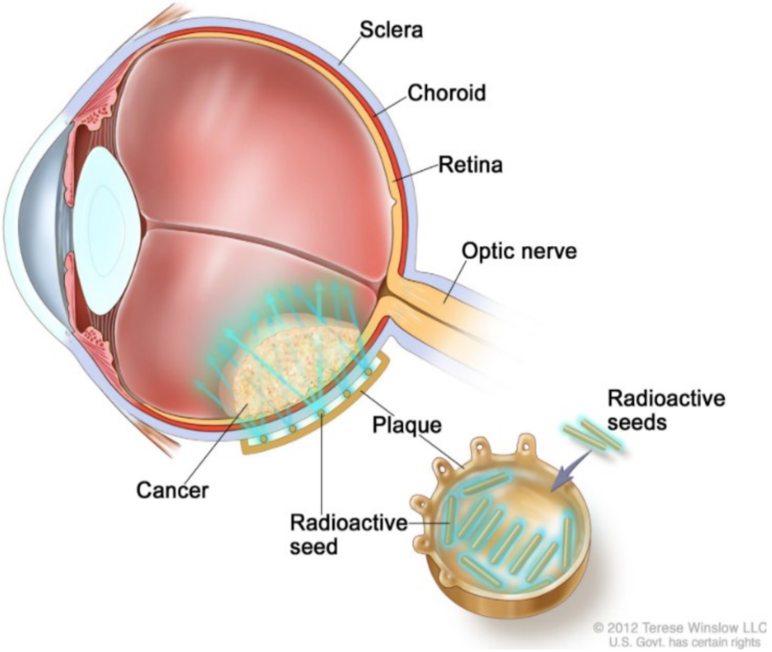

Figure 1.2 Diagram of the COMS eye plaque fully in contact with the eye surface for plaque brachytherapy treatment (image adapted from https://www.melanomanetwork.ca/wp-content/uploads/2015/04/140622-MNC_UvealGuideBooklet_FIN2_lr1.pdf with permission from Terese Winslow LLC).

1.2.1 Radionuclides and plaque types used in ocular brachytherapy

For plaque brachytherapy, various radionuclides and plaque types of different sizes are available for treatment. The choice of an appropriate radionuclide for a specific brachytherapy treatment depends on several relevant physical and dosimetric characteristics, such as energy, half-life, half-value layer, source strength, and inverse square fall-off of dose with distance from the source [25]. High-energy photon emitters, such as Ir-192, Co-60, and Au-198 are rarely used in plaque brachytherapy because of the deeper penetration of the emitted photons which would deliver higher doses to the critical structures in the eye and surrounding normal tissue and also requires more radiation safety precautions [25]. Therefore, low-energy photon emitters are the common choice for plaque brachytherapy treatments due to their low penetration into the surrounding tissues, and thus reduced dose to critical structures of the eye. The most commonly used radioactive source is I-125, mainly due to its use in the COMS trials. This work was performed using the model IAI-125A seed (IsoAid LLC, Port Richey, FL; Figure 1.3). Other photon emitters used for plaque brachytherapy include Pd-103 and Cs-131. Though less commonly used in comparison to photons, beta emitting sources have also been used for plaque brachytherapy and these include: Ru-106 (most commonly used) and Sr-90/Y-90 [25]. A list of commonly used radionuclides in plaque brachytherapy along with their physical characteristics are shown in Table 1.1.

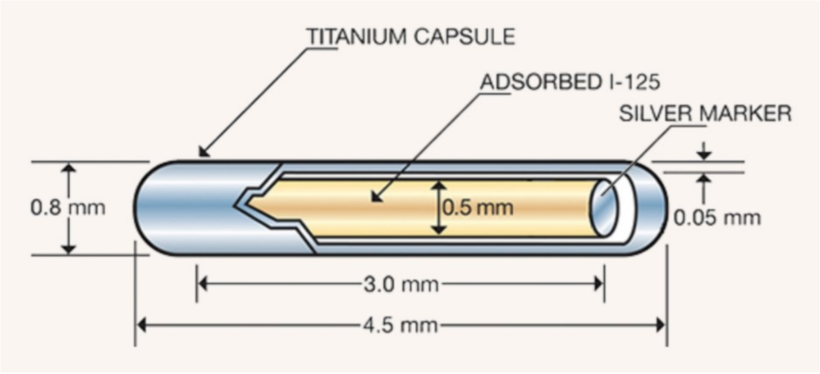

Figure 1.3 Schematic diagram of the model IAI-125A seed depicting the seed design from the seed manufacturer (image reproduced from https://isoaid.com/prod_pages/radioactive_seeds with permission from IsoAid, LLC).

Table 1.1 Physical characteristics of radionuclides commonly used in plaque brachytherapy [26,27].

		Mean energy	Half-life (d)
Photon emitter	I-125	28.4 keV	59.4
	Pd-103	20.7 keV	16.99
	Cs-131	30.4 keV	9.69
Beta emitter	Ru-106	3.54 MeV	371.8

Among the different types of eye plaques currently available, the COMS eye plaque design is the most popular type used in plaque brachytherapy [28]. The COMS plaques are constructed such that the radioactive seeds are sandwiched between a gold alloy (Modulay) outer backing and an inner silicone seed carrier (also called Silastic; Figure 1.4a). The gold backing has a lip or edge shield which encircles the plaque and extends to touch the sclera, and provides collimation of the radiation emitted by the seeds. To help attach the plaque to the eye, there are suture holes on the periphery of the plaque. The seeds are embedded into the grooves of the Silastic which is then glued to the gold backing (Figure 1.4b) [23].

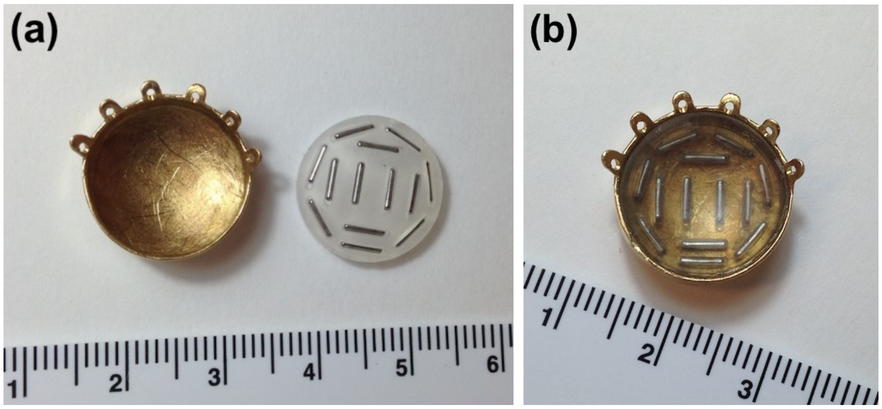

Figure 1.4 16 mm COMS plaque viewed from above: (a) a gold plaque backing (left), and the corresponding Silastic carrier loaded with the I-125 seeds (right), and (b) Silastic carrier fitted in the gold backing with the seeds on the inside surface.

The COMS plaques are available in different diameters ranging from 10 - 22 mm, in 2 mm increments (Figure 1.5a,b) [29]. They also come in notched versions which allow closer placement of the plaque to the tumor that lies near the optic nerve (Figure 1.5c). The plaque size is chosen such that the tumor base and a tumor-free margin of 2 to 3 mm are covered entirely by the plaque [23].

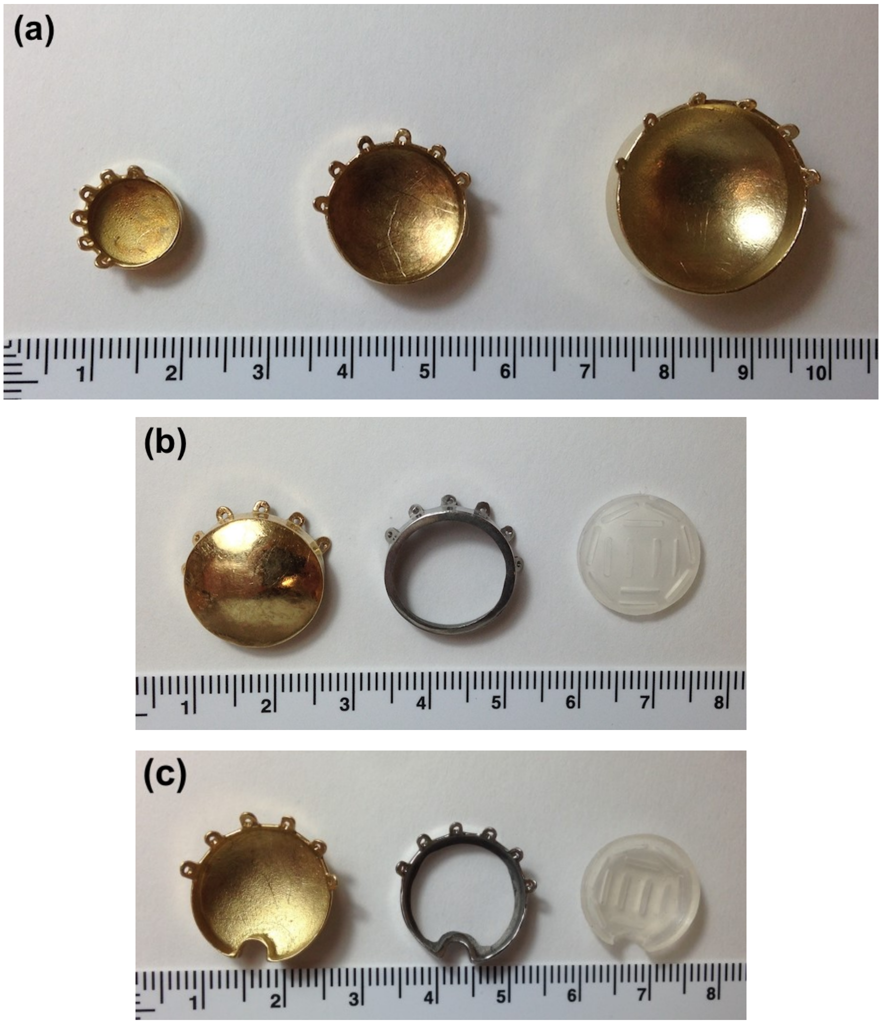

Figure 1.5 COMS plaques, from left to right: (a) 10 mm, 16 mm, and 22 mm plaque backing; (b) 16 mm plaque backing, dummy plaque, and Silastic insert; and (c) 16 mm notched plaque backing, dummy plaque, and Silastic insert.

Other currently available plaques include: Eye Physics plaques, ROPES plaques, OSU-NAG plaques and BEBIG plaques. Eye Physics plaques have seed slots milled into an 18 karat gold alloy backing (Figure 1.6a). They do not have a Silastic insert; the seeds are directly glued into the slots. The slots collimate the radiation from each source to remove laterally directed primary radiation that does not contribute to the tumor dose [30]. OSU-NAG plaques use the same gold alloy as the COMS plaques but does not have a Silastic seed carrier (Figure 1.6b). The seeds are directly glued onto its concave surface at conveniently determined and equally spaced locations. They come in several shapes other than just circular and have larger suture eyelets compared to the COMS plaques [31]. ROPES plaques consist of an acrylic carrier with holes for the seeds combined with a stainless steel backing shield to place the acrylic insert in (Figure 1.6c). Available plaque diameters are 11, 15, and 18 mm with 4, 9 or 10, and 15 seeds, respectively [32]. In BEBIG plaques, a thin film of Ru-106 is encapsulated within a sheet of pure silver, with a total thickness of 1 mm (Figure 1.6d). The plaques are hemispherically shaped with a radius of 12-14 mm and have rounded edges, a homogeneous lead seam and eyelets for suturing to the sclera [33].

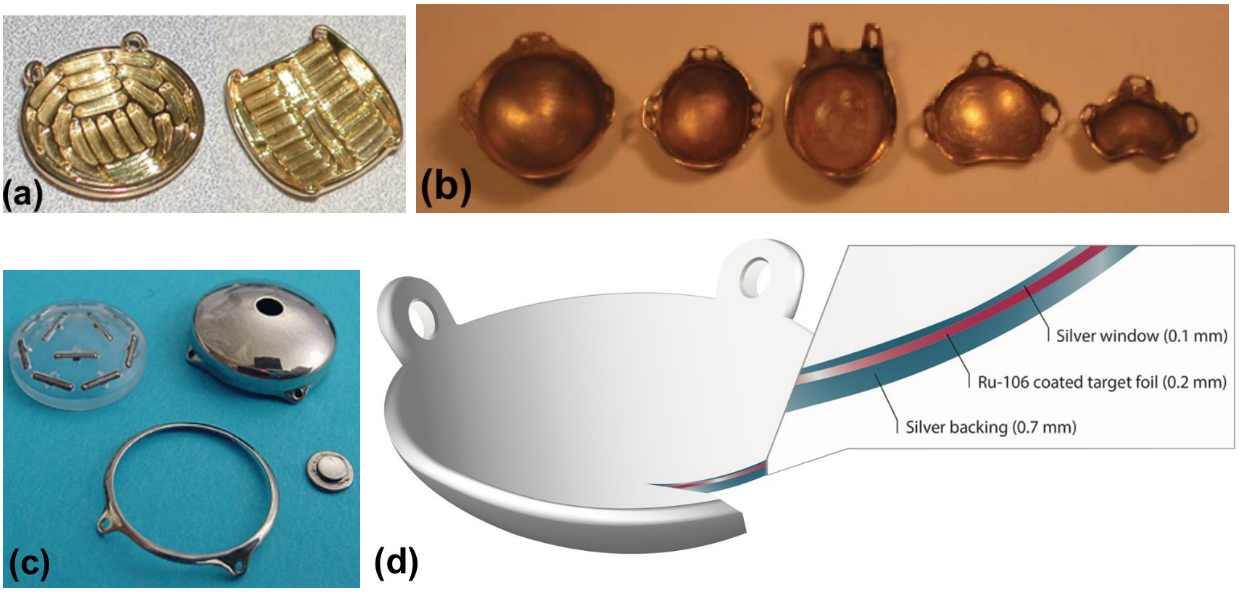

Figure 1.6 (a) Eye Physics 2nd generation plaques: model EP2031 (left) and model EP2025 (right) (images adapted from https://www.eyephysics.com with permission from Astrahan); (b) OSU-NAG eye plaques (figure adapted from Zhang et al. [31]); (c) 15 mm ROPES plaque assembly with acrylic carrier insert with seeds, stainless steel backing, dummy plaque, and ejector pin (figure reproduced with permission from Astrahan [34]); and (d) Ru-106 BEBIG plaque design (figure reproduced from the Ru-106 BEBIG plaque product fact sheet with permission from Eckert & Ziegler BEBIG GmbH [35]).

1.2.2 Treatment methodology

The treatment planning task of generating suitable dosimetry with the plaque involves several steps. Initially, the tumor dimensions (height and basal measurements) and position in the eye must be determined. This is done using multiple imaging modalities including fundus photography, ultrasound, and CT (or MRI) (Figure 1.7).

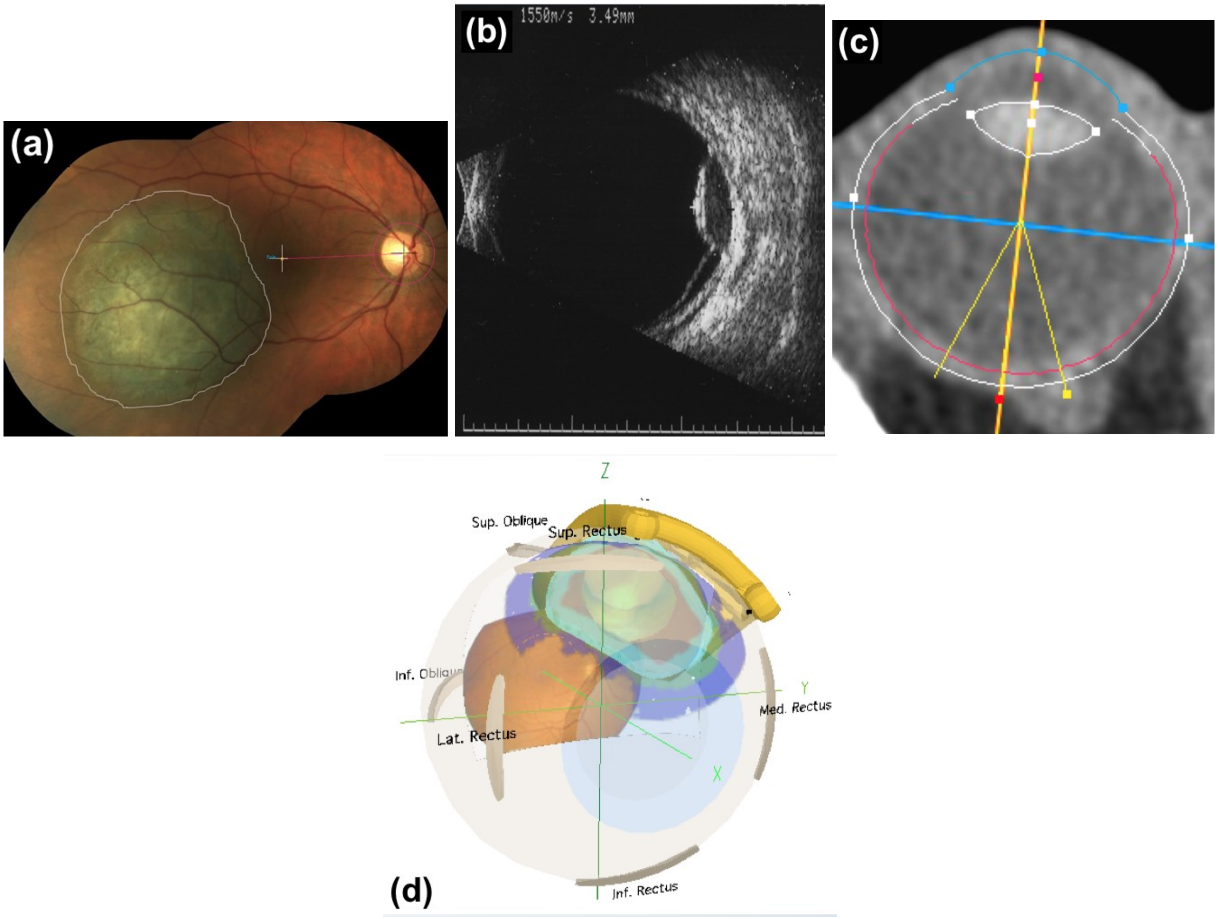

Figure 1.7 (a) Fundus photo showing the tumor (pigmented region contoured by a white line), optic disc (bright region marked by a black crosshair and red circle), and posterior pole (marked by a white crosshair); (b) ultrasound image showing the tumor height in the eye (image adapted with permission from Astrahan [36]); (c) CT image bisecting the eye through the optic nerve (image reproduced with permission from Astrahan [36]); and (d) 3D visualization of the eye by the treatment planning system with the input information (figure adapted with permission from Astrahan [36]).

A fundus image shows the back of the eye which allows the identification of locations of the tumor, optic disc, and posterior pole. Ultrasound imaging provides the measurement of tumor height and basal dimension, and a CT image is employed to obtain the geometry of the globe of the eye. Information from these images are then input into a treatment planning system (TPS) to create a treatment plan that calculates the radioactive seed strength necessary to deliver the desired minimum prescription dose, typically to the tumor apex [23,37]. Treatment planning for plaque brachytherapy using the TPS is discussed in Section 1.2.3. Once the plaque is assembled according to the treatment plan, it is sterilized before insertion. In an operating room, the suture coordinates are mapped onto the eye, and the position of the plaque is verified with the help of a dummy plaque (a plaque of the same design and dimension as the treatment plaque but with no radioactive sources) sutured in place. Once the dummy plaque position is verified relative to the chosen location, the dummy plaque is replaced with the actual plaque, which is attached to the eye surface using the same sutures. The plaque is left in the treatment position for a predetermined treatment time, typically between 4 and 7 days [37].

1.2.3 Treatment planning system – Plaque Simulator

Currently the only commercially available TPS for plaque brachytherapy dose calculations is the Plaque Simulator (Eye Physics, Los Alamitos, CA), which provides interactive 3D treatment simulation by creating 2D and 3D models of both the eye and tumor and also performs isodose calculation and display (Figure 1.8) [36]. In terms of dosimetry, Plaque Simulator uses the American Association of Physicists in Medicine (AAPM) TG-43 formalism in water to perform dose calculations with the option to include corrections for the heterogeneous plaque materials derived from Monte Carlo simulations [38]. Details of the dose calculation formalism are provided in Chapter 2.

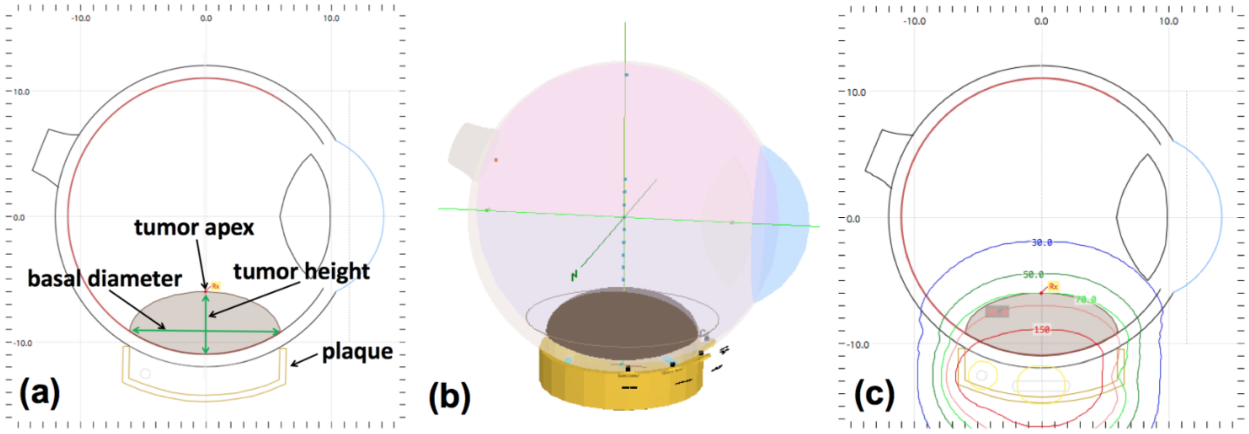

Figure 1.8 Plaque Simulator generated (a) 2D model of the eye, tumor, and plaque with labels of the tumor apex, tumor height, basal diameter, and plaque; (b) 3D model of the eye, tumor, and plaque (image adapted with permission from Astrahan [36]); and (c) isodose lines from a fully loaded plaque (image reproduced with permission from Astrahan [36]).

The four inputs for Plaque Simulator calculations are: plaque size preference and placement, prescription depth, prescription dose, and treatment duration (with the first two determined by the information from the images mentioned in Section 1.2.2). The output from the TPS is the required uniform source strength for all seeds to achieve the prescription dose at the prescription point (typically the tumor apex). Once the system creates a plan with a full and uniformly loaded plaque, one could perform manual optimization of the plan by choosing ideal seed locations to reduce dose to critical structures. Typically, the calculation is performed with a fully loaded plaque; however, with experience, desired seed locations can also be selected as a fifth input.

Although Plaque Simulator is widely used, it has several limitations. Firstly, it is designed to calculate dose distributions using uniform source strengths for all seeds. These uniformly loaded plaques can result in high doses to the critical structures and are not automatically adjustable. This demands manual post-computer planning to determine optimal seed loading in the plaque, plaque repositioning, and determination of differential source strengths that can provide the required prescription dose while reducing critical structure irradiation. This process can be time-consuming, requires experience, and may not always find the best possible plan. Moreover, the system does not account for tissue inhomogeneities as it calculates dose in a homogeneous water medium, which is a source of dose calculation inaccuracy.

1.2.4 Clinical outcomes

The COMS study showed that plaque brachytherapy using I-125 for medium-sized tumors results in an overall survival rate at 5- and 10-year of 81% and 65%, respectively [24]. Also, local control rate was 89.7% and mortality rates with metastasis at 5 and 10 years were 10% and 18%, respectively [24]. Larger tumors (≥ 5 mm height) appeared to have worse survival outcomes [39]. The most common site of metastasis is the liver and there are currently no effective treatment options after metastasis [40]. Potential side effects of plaque brachytherapy include: decreased visual acuity, cataract formation, retinopathy, glaucoma, and optic neuropathy [41]. The side effects are closely related to doses received by the critical structures of the eye. For instance, lens dose is related to the formation of cataract, and dose to optic disc, macula, and inner sclera are related to reduction in visual acuity [41]. Tolerance doses (TD) to the critical structures of the eye are shown in Table 1.2. TD 5/5 indicates the probability of 5% complication at five years from treatment and TD 50/5 is the probability of 50% complication at five years.

Table 1.2 Tolerance doses of the critical structures in the eye.

Critical structure	D_{max} (Gy)	TD 5/5 (Gy)	TD 50/5 (Gy)
Cornea	10-20 [42]		
Sclera	900 [42]		
Retina	< 50 [43,44]	45-50 [45]	55 [45]
Optic nerve	< 55 [43]	> 55 [45]	> 65 [45]
Lens	< 10 [44]	10 [45]	18 [45]
Macula	< 50 [46]		

Plaque brachytherapy treatments also show superior clinical outcomes compared to other treatment modalities. For instance, comparative studies between I-125 plaque brachytherapy and proton EBRT have shown that both modalities yield good local tumor control and visual outcomes; however, proton EBRT resulted in higher secondary enucleation rates than plaque brachytherapy [47,48]. A more recent study by Lin *et al.* showed, for the propensity-score matched cohort of patients with choroid melanoma, a 5-year overall survival of 77% vs. 51% for plaque brachytherapy and proton EBRT, respectively [49]. Also, compared to stereotactic radiotherapy – an EBRT technique that uses numerous precisely focused radiation beams to treat tumors with a high dose of radiation, often used for patients who are not suitable for treatment with plaque brachytherapy or enucleation – Georgopoulos *et al*. observed a faster and more pronounced reduction in tumor thickness using plaque brachytherapy, and similar two-year local control rates of 94-98% for both plaque brachytherapy and stereotactic radiotherapy [50].

1.3 Thesis overview

Currently the TPS used in ocular plaque brachytherapy treatment planning is designed to create treatment plans using uniform radioactive seed strengths at the user defined plaque seed locations. Any changes to individual seed strengths must be performed manually. The purpose of this research project is to develop and apply an automated dose optimization algorithm for ocular plaque brachytherapy treatments. This algorithm will find an optimal distribution of differential seed strengths in order to provide improved dose conformity, delivering an effective treatment for intraocular tumors while increasing the likelihood of eye preservation and vision sparing relative to traditional manual planning.

In this thesis, Chapter 1 provides an introduction to ocular cancers and plaque brachytherapy, describing how treatment and planning are performed clinically. The objective of the thesis has also been presented. In Chapter 2, dose optimization in plaque brachytherapy is introduced, describing the dose calculation formalism, various optimization methods currently used in radiotherapy, and the simulated annealing (SA) algorithm to be used for optimization in this work. Chapter 3 provides details of the implementation of SA algorithm in plaque brachytherapy planning. Starting with the modelling of tumor and seed geometry in software, verification of the SA algorithm by solving two general problems are described which are: dose optimization using uniform loading, and maximizing dose uniformity across tumor base with differential loading. Through the first problem, the correct implementation of the seed geometry, dose calculation, as well as the general steps of the SA algorithm are to be verified. Furthermore, the second problem would allow to verify whether the algorithm can find minima in the energy function with using differential loading. In Chapter 4, the final problem of optimizing for differential seed strengths to reduce doses to the critical structures of the eye with achievement of the tumor coverage is to be tackled. The development of the SA algorithm for this specific problem is described in detail, including the introduction of points of interest to represent the critical structures, objective function, and cooling schedule. For a more sophisticated algorithm, additional features that were developed in the algorithm including plaque shifting and elliptical tumor base shapes in modelling are also described. Lastly, application of the algorithm to various clinical cases is presented for verification of the practicality of clinical implementation of the algorithm. Finally, Chapter 5 provides a summary of this thesis and potential future work.

1.4 References

[1] Canadian Cancer Statistics Advisory Committee. Canadian Cancer Statistics 2018. Toronto, ON: Canadian Cancer Society; 2018. Available at: cancer.ca/Canadian-Cancer-Statistics-2018-EN (accessed [October, 2018]).

[2] Weis E, Salopek TG, McKinnon JG, et al. Management of uveal melanoma: a consensus-based provincial clinical practice guideline. *Curr Oncol*. 2016;23(1):e57-64.

[3] Stannard C, Sauerwein W, Maree G, Lecuona K. Radiotherapy for ocular tumours. *Eye (Lond)*. 2012;27(2):119-27.

[4] Rogers K. *The eye: The physiology of human perception (the human body), 1st ed.* New York, NY: Britannica Educational Publishing; 2011.

[5] Canadian Cancer Society. Cancerous tumours of the eye. http://www.cancer.ca/en/cancer-information/cancer-type/eye/eye-cancer/cancerous-tumours/?region=on. Accessed June, 2018.

[6] Alberta Health Services Uveal melanoma clinical practice guideline CU-015 version 1. ; 2014:1-28.

[7] Edge SB, Byrd DR, Compton CC, Fritz AG, Greene FL, Trotti A et al. (eds). Malignant melanoma of the uvea. In: *AJCC Cancer Staging Manual*, 7th edn. Springer: New York, NY, USA, 2010, pp 547–559.

[8] Cancer.Net. Cancer types-statistics, https://www.cancer.net/cancer-types, Accessed October, 2018.

[9] Radiological Society of North America. Introduction to cancer therapy (radiation oncology). https://www.radiologyinfo.org/en/info.cfm?pg=intro_onco. Updated 2017. Accessed June, 2018.

[10] Cancer.Net. Eye cancer: Treatment options. https://www.cancer.net/cancer-types/eye-cancer/treatment-options. Updated 2015. Accessed June, 2018.

[11] Nag S, Quivey JM, Earle JD, Followill D, Fontanesi J, Finger PT; American Brachytherapy Society. The American Brachytherapy Society recommendations for brachytherapy of uveal melanomas. *Int J Radiat Oncol Biol Phys*. 2003;56(2):544-555.

[12] Shields JA, Shields CL. *Intraocular tumors: An atlas and textbook, 3rd ed.* Philadelphia, PA: Wolters Kluwer, Lippincott Willians & Wilkins; 2015.

[13] Char DH, Miller T, Crawford JB. Uveal tumour resection. *Br J Ophthalmol*. 2001;85(10):1213-1219.

[14] Yang J, Manson DK, Marr BP, Carvajal RD. Treatment of uveal melanoma: where are we now?. *Ther Adv Med Oncol*. 2018;10:1758834018757175. Published 2018 Feb 21. doi:10.1177/1758834018757175.

[15] Puusaari I, Damato B, Kivela T. Transscleral local resection versus iodine brachytherapy for uveal melanomas that are large because of tumour height. *Graefes Arch Clin Exp Ophthalmol*. 2007;245(4):522-533.

[16] Bechrakis NE, Petousis V, Willerding G, et al. Ten-year results of transscleral resection of large uveal melanomas: Local tumour control and metastatic rate. *Br J Ophthalmol*. 2010;94(4):460-466.

[17] American Cancer Society. Laser therapy for eye cancer. https://www.cancer.org/cancer/eye-cancer/treating/laser-therapy.html. Updated 2016. Accessed June, 2018.

[18] Dithmar S. Transpupillary thermotherapy. In: Age-related macular degeneration. Springer, Berlin, Heidelberg; 2004:159-167.

[19] Bell DJ, Wilson MW. Choroidal melanoma: natural history and management options. *Cancer Control.* 2004;11(5):296-303.

[20] Tarlan B, Kıratlı H. Uveal Melanoma: Current Trends in Diagnosis and Management. *Turk J Ophthalmol*. 2016;46(3):123-137.

[21] Bartlema YM, Oosterhuis JA, Journée-De Korver JG, Tjho-Heslinga RE, Keunen JE. Combined plaque radiotherapy and transpupillary thermotherapy in choroidal melanoma: 5 years' experience. *Br J Ophthalmol*. 2003;87(11):1370-1373.

[22] Mahendraraj K, Lau C, Lee I, Chamberlain RS. Trends in incidence, survival, and management of uveal melanoma: A population-based study of 7,516 patients from the surveillance, epidemiology, and end results database (1973–2012). *Clinical Ophthalmology*. 2016;10:2113-2119.

[23] Collaborative Ocular Melanoma Study Group. Ch 12: Radiation therapy. In: *COMS manual of procedures.* National Technical Information Service, Springfield, VA; 1995.

[24] Collaborative Ocular Melanoma Study (COMS) Group. The COMS randomized trial of iodine 125 brachytherapy for choroidal melanoma: V. Twelve-year mortality rates and prognostic factors: COMS report no. 28. *Arch Ophthalmol*. 2006;124(12):1684–1693.

[25] Podgorsak EB. *Radiation oncology physics: A handbook for teachers and students.* Vienna (Austria): International Atomic Energy Agency; 2005.

[26] Khan FM, Gibbons JP. *Khan's the physics of radiation therapy.* Philadelphia (USA): Williams & Wilkins; 2014.

[27] NUDAT 2.7, National Nuclear Data Centre, Brookhaven National Laboratory. http://www.nndc.bnl.gov/chart/decaysearchdirect.jsp?nuc=125I&unc=nds. Accessed September, 2018.

[28] Zhang H, Martin D, Chiu-Tsao ST, Meigooni A, Thomadsen BR. A comprehensive dosimetric comparison between 131Cs and 125I brachytherapy sources for COMS eye plaque implant. *Brachytherapy*. 2010;9(4):362-372.

[29] Chiu-Tsao ST, Astrahan MA, Finger PT, et al. Dosimetry of ^{125}I and ^{103}Pd COMS eye plaques for intraocular tumors: Report of Task Group 129 by the AAPM and ABS. *Med Phys.* 2012;39(10): 6161-6184.

[30] Zimmermann LW, Amoush A, Wilkinson DA. Episcleral eye plaque dosimetry comparison for the Eye Physics EP917 using Plaque Simulator and Monte Carlo simulation. *J Appl Clin Med Phys*. 2015;16(6):226-239.

[31] Zhang H, Davidorf F, Qi Y, Comparison of 16 mm OSU-Nag and COMS eye plaques. *J Appl Clin Med Phys.* 2012;13(3):166-178.

[32] Poder J, Annabell N, Geso M, Alqathami M, Corde S. ROPES eye plaque dosimetry: commissioning and verification of an ophthalmic brachytherapy treatment planning system. *J Phys: Conf Ser.* 2013;444(1) 012102.

[33] Eye Physics Ver. 6 User Guide. BEBIG plaque information. https://www.eyephysics.com/PS/PS6/UserGuide/BEBIGPlaquesMenu.html. Accessed October, 2018.

[34] Eye Physics Ver. 6 User Guide. Assembling the ROPES Plaque. https://www.eyephysics.com/PS/PS5/UserGuide/AssembleROPES.html. Accessed October, 2018.

[35] Eckert & Ziegler BEBIG GmbH. Ru-106 eye applicators. https://www.bebig.com/fileadmin/bebig_neu/user_uploads/Products/Ophthalmic_Brachytherapy/Fact_sheet_Ru-106_Eye_Applicators_Rev.05_English.pdf. Accessed October, 2018.

[36] Eye Physics Ver. 6 User Guide. Plaque Simulator. https://www.eyephysics.com/PS/Index.html. Accessed October, 2018.

[37] The American Brachytherapy Society - Ophthalmic Oncology Task Force. The American brachytherapy society consensus guidelines for plaque brachytherapy of uveal melanoma and retinoblastoma. *Brachytherapy*. 2014;13(1):1-14.

[38] Nath R, Anderson LL, Luxton G, Weaver KA, Williamson JF, Meigooni AS. Dosimetry of interstitial brachytherapy sources: recommendations of the AAPM Radiation Therapy

Committee Task Group No. 43. American Association of Physicists in Medicine. *Med Phys.* 1995;22(2):209-234.

[39] Perez BA, Mettu P, Vajzovic L, Rivera D, Alkaissi A, Steffey BA, Cai J, Stinnett S, Dutton JJ, Buckley EG, Halperin E, Marks LB, Mruthyunjaya P, Kirsch DG. Uveal melanoma treated with iodine-125 episcleral plaque: An analysis of dose on disease control and visual outcomes. *Int J Radiat Oncol Biol Phys.* 2014;89(1):127-136.

[40] Gonsalves CF, Eschelman DJ, Thornburg B, Frangos A, Sato T. Uveal Melanoma Metastatic to the Liver: Chemoembolization With 1,3-Bis-(2-Chloroethyl)-1-Nitrosourea. *AJR Am J Roentgenol.* 2015;205(2):429-433.

[41] Wagner A, Chen A, Cook T, Faber D, Winward K, Sause W. Outcomes and control rates for I-125 plaque brachytherapy for uveal melanoma: A community-based institutional experience. *ISRN Ophthalmol.* 2014;2014:1-7.

[42] Ober M, Servodidio CA, Abramson D. Ocular complications due to cancer treatment. In *Survivors of Childhood and Adolescent Cancer: A Multidisciplinary Approach*. Edited by Schwartz CL, Hobbie WL, Constine LS, Ruccione KS. Heidelberg: Springer; 2005:81–94.

[43] Emami B. Tolerance of normal tissue to therapeutic Radiation. *Rep Radiother Oncol.* 2013;1(1):123-127.

[44] Scoccianti S, Detti B, Gadda D, Greto D, Furfaro I, Meacci F, Simontacchi G, Brina LD, Bonomo P, Giacomelli I, Meattini I, Mangoni M, Cappelli S, Cassani S, Talamonti C, Bordi L, Livi L. Organs at risk in the brain and their dose-constraints in adults and in children: A radiation oncologist's guide for delineation in everyday practice. *Radiother Oncol.* 2015;114(2):230-238.

[45] Durkin SR, Roos D, Higgs B, Casson RJ, Selva D. Ophthalmic and adnexal complications of radiotherapy. *Acta Ophthalmol Scand*. 2007;85(3):240-250.

[46] Puusaari I, Heikkonen J, Kivela T. Effect of radiation dose on ocular complications after iodine brachytherapy for large uveal melanoma: Empirical data and simulation of collimating plaques. *Invest Ophthalmol Vis Sci*. 2004;45(10):3425-3434.

[47] Hungerford JL, Foss A, Whelahan I, Errington RD, Kacperek A, Kongerud J. Side effects of photon and proton radiotherapy for ocular melanoma. *Front Radiat Ther Oncol*. 1997;30:287-293.

[48] Wilson MW, Hungerford JL. Comparison of episcleral plaque and proton beam radiation therapy for the treatment of choroidal melanoma. *Ophthalmology*. 1999;106(8):1579-1587.

[49] Lin AJ, Rao YJ, Acharya S, Schwarz J, Rao PK, Grigsby P. Patterns of care and outcomes of proton and eye plaque brachytherapy for uveal melanoma: Review of the National Cancer Database. *Brachytherapy.* 2017;16(6):1225-1231.

[50] Georgopoulos M, Zehetmayer M, Ruhswurm I, Toma-Bstaendig S, Segur-Eltz N, Sacu S, Menapace R. Tumour regression of uveal melanoma after Ruthenium-106 brachytherapy or stereotactic radiotherapy with gamma knife or linear accelerator. *Ophthalmologica*. 2003;217(5): 315-319.

Chapter 2 Dose optimization in plaque brachytherapy

2.1 Introduction

In order to create a treatment plan that can achieve the best possible tumor coverage and sparing of surrounding healthy tissues, the fundamental process of dose optimization must be performed strategically during planning. As various dose optimization methods exist, a careful choice must be made in selecting an effective approach specific to the particular type of radiotherapy treatment. This chapter describes the dose calculation formalism and the optimization methods currently used in plaque brachytherapy and the simulated annealing algorithm proposed to be used for optimization in this study.

2.1.1 Dose calculation: TG-43 formalism

The American Association of Physicists in Medicine's (AAPM) Task Group 43 (TG-43) report is the consensus standard for photon brachytherapy dose calculations [1]. In the basic TG-43 formalism, the dose rate at any point $P(r,\theta)$, as shown in Figure 2.1, in a homogeneous water medium is given by [1]:

$$\dot{D}(r,\theta)_{TG-43} = S_K \cdot \Lambda \cdot \frac{G_L(r,\theta)}{G_L(r_0,\theta_0)} \cdot g_L(r) \cdot F(r,\theta), \qquad \text{(Eq. 2.1)}$$

where r is the distance from the source centre to P, r_0 is the reference distance (1 cm) along the perpendicular axis, θ is the polar angle relative to the source long-axis, θ_0 is the reference angle (90°), S_K is the source strength (U or $\mathrm{cGy \cdot cm^2 \cdot h^{-1}}$), Λ is the dose rate constant ($\mathrm{cGy \cdot h^{-1} \cdot U^{-1}}$), $G_L(r,\theta)$ is the geometry function ($\mathrm{cm^{-2}}$), $g_L(r)$ is the radial dose function (unitless) and $F(r,\theta)$ is the anisotropy function (unitless). The subscript 'L' denotes that the line source approximation is used.

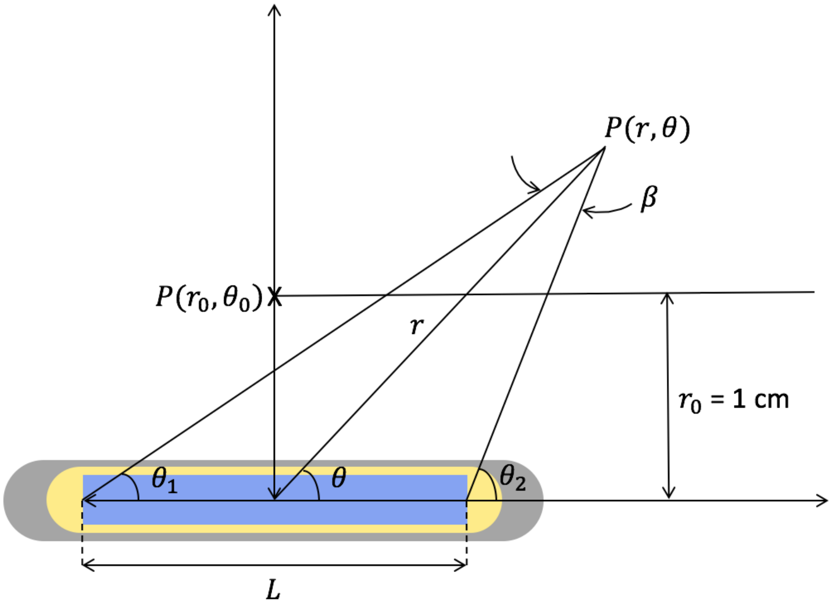

Figure 2.1 Illustration of coordinate system used in the TG-43 dose calculation formalism. β is the angle subtended by the two ends of the active source at point P. The reference point is represented by $P(r_0,\theta_0)$.

As the TG-43 formalism given by Eq. 2.1 does not account for plaque heterogeneities, the resulting dose differences can be greater than 10% [2]. Hence, the AAPM TG-129 report recommends the use of material heterogeneity corrections, especially to account for the reduced backscatter due to the gold backing and the increased attenuation through the Silastic insert [2]. Plaque Simulator, a commercial eye plaque treatment planning system, uses the TG-43 formalism for dose calculation, with two correction factors to correct for the plaque heterogeneities: $T(r)$ and $t(d,\mu)$ [3]. $T(r)$ accounts for scatter and attenuation by the gold-alloy backing and 1 mm path length in Silastic insert. $t(d,\mu)$, with μ being the linear attenuation coefficient, accounts for the additional path length, d>1 mm, in the Silastic insert that is unaccounted for in $T(r)$, and is calculated from the ratio of attenuation through the Silastic insert and water [3]:

$$t(d,\mu) = e^{-\mu_{Silastic}d} / e^{-\mu_{water}d}. \qquad \text{(Eq. 2.2)}$$

In the Plaque Simulator, when both $T(r)$ and $t(d,\mu)$ are used, they are combined into one factor as $T(r,d,\mu)$. In addition, another factor, $A(R)$, is also employed in Plaque Simulator to account for the reduced backscatter due to the air interface in front of the eye, where R is the distance from the eye-air interface at the dose calculation point. On incorporating all the correction factors, the net dose rate is then given as:

$$\dot{D}(r,\theta,d,\mu) = \dot{D}(r,\theta)_{TG-43} \cdot T(r) \cdot t(d,\mu) \cdot A(R). \qquad \text{(Eq. 2.3)}$$

However, this formalism does not account for patient tissue heterogeneities, which have also been found to impact dosimetry significantly (up to 10% for the tumor and up to 27% for critical structures in the eye) [4,5]. This has led to the use of model-based dose calculation algorithms (MBDCAs), which can model radiation transport in non-water media (such as tissues, applicators, air-tissue interfaces), characterizing a more accurate reconstruction of the dose distribution actually delivered to the patient. The AAPM TG-186 report provides specific guidance for adopting MBDCAs for brachytherapy [4]. However, this option of using MBDCAs is not available in Plaque Simulator. Also, plaque brachytherapy planning is conventionally done using a plaque where all seed positions are occupied (fully loaded), and all seeds are typically of equal strength (uniformly loaded). Plaque Simulator allows the user to manually select seed positions (partial loading) and also manually adjust individual seed strengths (non-uniform loading). As this process is not automated, it is tedious and time-consuming. Therefore, automated optimization of both the loading pattern and seed strengths has the potential to greatly improve planning for plaque brachytherapy.

2.1.2 Inverse planning and objective function

In the conventional manual trial-and-error treatment planning known as “forward planning”, the treatment parameters are first chosen and then the resulting dose distribution is calculated and evaluated by an experienced planner. Though this approach is often sufficient for uncomplicated cases, the adjustment of dose distributions to respect different dose constraints on various targets and organs at risk in a reasonable calculation time frame for clinical application, is often beyond human capabilities [6]. A solution to this issue is to take the “inverse planning” approach. Inverse planning is a general treatment planning method where one starts with the desired dose distribution or clinical objectives, and then determines the treatment parameters that will achieve it [6]. Anatomical information obtained from planning images is integrated with clinical dosimetric requirements, including tumor coverage and normal tissue sparing, to optimize the dose distribution. Therefore, the main advantage of the inverse planning approach is that all clinical requirements are simultaneously and automatically taken into account in the planning process, and could potentially result in better treatments (higher tumor control probability and lower normal tissue complication probability), unlike with the forward planning approach [6].

In general, inverse planning in radiotherapy uses pre-defined target doses, dose-volume constraints, and other importance factors such as weightings for the target and surrounding healthy tissues in the optimization process to generate a treatment plan that best agrees with all the input criteria. As there are often multiple clinical objectives that compete against each other, like the dosimetric constraints for tumor and healthy tissues, they are combined and transformed into a single mathematical function called "objective function". The objective function essentially converts a given treatment plan into a single score that quantifies how closely the calculated dose distribution matches user-defined criteria [7]. The goal of the inverse planning process is then to find a solution that optimizes the objective function. Although there is no guarantee that the multiple objectives can simultaneously be fulfilled, specific trade-offs between the objectives can be achieved by carefully varying the choice of importance factors. Some examples of objectives are to minimize the sum of $\left|D_{plan} - D_{Rx}\right|$ (with D_{plan} being the calculated dose and D_{Rx} being the prescription dose) and to maximize the minimum dose to planning target volume (PTV) [7].

2.1.3 Optimization methods

There are various dose optimization methods that can be applied to solve for an inverse problem, most of which use iterative numerical techniques. In general, optimization problems are expressed as minimization problems in which the minimum of the objective function is sought. One major class of optimization techniques is known as "deterministic" method [8,9]. These techniques find solutions by searching for a result that reduces the value of an objective function in a 'downhill' fashion during each iteration (Figure 2.2a); they may use derivatives of the objective function to determine the size and direction of the next step. These techniques are fast but a solution may get trapped in a local extremum since the derivative at any extremum is zero. Some examples of common deterministic methods include: steepest descent, conjugate gradient, and Nelder-Mead simplex methods. Another major class of optimization method is called "stochastic" [8,9]. These are iterative techniques that basically throw a dice to find new positions in the search space at each iteration step, and thus use randomness in the search process (Figure 2.2b) [8]. As shown in Figure 2.2b, stochastic methods do not move strictly downhill and therefore, in contrast to deterministic methods, they allow possible escape from local minima. They are generally slower but may be advantageous if local minima exist and/or if analytic derivatives of the objective function cannot be computed [9]. Some examples of these methods are: simulated annealing and genetic algorithms.

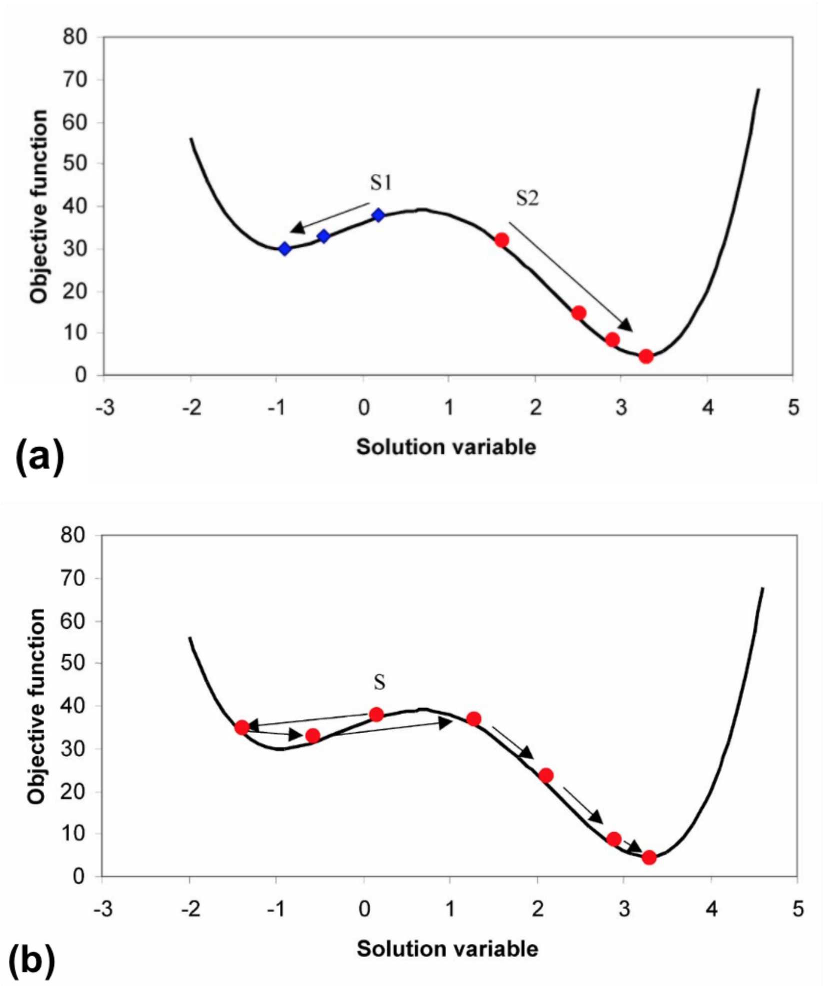

Figure 2.2 Graphical representation of optimization process for (a) deterministic and (b) stochastic method. Dots represent different energy states (objective function values); starting at point S1, S2 or S, a solution moves in solution space following the arrows which indicate acceptances of energy states (figures adapted from Ezzell with permission from AAPM [9]).

2.2 Simulated annealing

Simulated annealing (SA) is a stochastic method that introduces an element of randomness into the search process. First introduced by Kirkpatrick *et al.* in 1983 [10], SA was proven to be useful through its various applications in inverse planning for radiotherapy and is the most widely used algorithm in EBRT [11,12]. Also, it has been applied in other numerous studies, such as gynecological [13,14], and prostate cancer brachytherapy [15,16].

SA is analogous to the natural process of physical annealing of solids. Physical annealing is referred to as tempering certain alloys of crystal by heating above the melting point, holding the temperature, and then cooling very slowly until solidification into a perfect crystalline structure, or until the structure is frozen at a minimum energy configuration [17]. This physical/chemical process produces high-quality materials. The simulation of this process is known as SA. Analogy is such that the defect-free crystal state corresponds to the global minimum energy configuration, the physical material states correspond to problem solutions, the energy of a state to cost of a solution, and the temperature to a control parameter [17]. Hence, in SA, an optimal solution to an objective function is searched in a fashion analogous to a crystal cooling from its initially high temperature and settling into its lowest energy state [18]. An effective temperature is introduced into the system being optimized, to simulate and control the cooling process as in a physical system. SA process begins from a high effective temperature to "melt" the system, and then gradually lowers the temperature until the system "freezes" beyond which no further changes occur [10]. At each temperature, the simulation must proceed long enough, with many iterations, for the system to reach a steady state [10]. The temperature is slowly decreased by following a cooling schedule which shortens the steps and reduces the likelihood of uphill moves of a solution in solution space. Thus, SA does not strictly move downhill but allows for controlled uphill steps during iterations to broaden the search for a better solution, essentially enabling escape from local extrema. If only those configurations that lower the cost function (more specific term for objective function; used to predict the cost associated with a certain action and thus it has to be minimized) of the system are accepted (as in "down-hill" methods), it is analogous to rapid quenching from high temperatures to T=0, that usually results in metastable solutions [10]. Rapid cooling also results in a system frozen into a metastable state far from the optimal configuration, which is avoided in SA [10].

Besides the advantage of having the capability to escape local extrema, SA is also desirable due to its relative simplicity [19]. A typical SA algorithm is easier to implement than other modern optimization techniques. Moreover, by its nature, SA is well-suited for complex many-dimensional cost functions, including those without a closed functional form [19].

On the other hand, there are also drawbacks for SA. Due to its stochastic nature, there is no guarantee that the best solution found by the SA algorithm is the true minimum, either local or global. Also, since all SA solutions are stochastic in nature, multiple solutions are not repeatable unless the same set of random numbers is used [19]. Successive solutions to the same problem will differ in a statistical manner, and this difference varies inversely with the speed of the cooling schedule [19]. The computational burden is also high for large problems, such as for optimizing a large number of beam intensity profiles in EBRT, which may require long execution times. However, with improving computing speeds and capability, SA is becoming increasingly useful [19].

2.2.1 SA algorithm

In this study, a SA algorithm was applied as an optimization method to solve for inverse problems in plaque brachytherapy planning. This section provides a general description of the SA algorithm showing only the basic steps; more details of the algorithm will be given in Chapter 3. Starting with an initial source strength S_K, a random transition to S_K is generated at each iteration i. The algorithm then calculates the resulting objective function value (called "energy" hereafter). For evaluating the new transition, the energy difference $\mathit{\Delta} E = E(i) - E(i-1)$ is calculated. If $\mathit{\Delta} E < 0$, or the new energy is lower than the old energy, the transition is always accepted. If $\mathit{\Delta} E > 0$, the transition is still accepted with a probability P given by:

$$P(\mathit{\Delta} E, T) = \exp\left(-\frac{\mathit{\Delta} E}{k_B T}\right), \qquad \text{(Eq. 2.4)}$$

where T is the effective temperature, and k_B is the Boltzmann constant. If P is greater than a random number between 0 and 1, the new transition is accepted and is used to create the next step.

Otherwise, it is rejected and the old state is retained. This concept of random acceptance of a solution is illustrated in Figure 2.3. This procedure is repeated, at the same temperature, until a large enough number of acceptances or attempts is reached. Then, the temperature is decreased according to the cooling schedule chosen by the user. Determining an optimal cooling schedule for a problem is a necessary step in applying SA to a problem, and will be described more in detail in Chapter 3. Next, this process of iterating for random transitions to S_K for i times and then changing the temperature is repeated until a sufficiently low temperature is reached, at which time the system is considered "frozen". Annealing process is then terminated. A flowchart that shows the general steps of the SA algorithm is displayed in Figure 2.4.

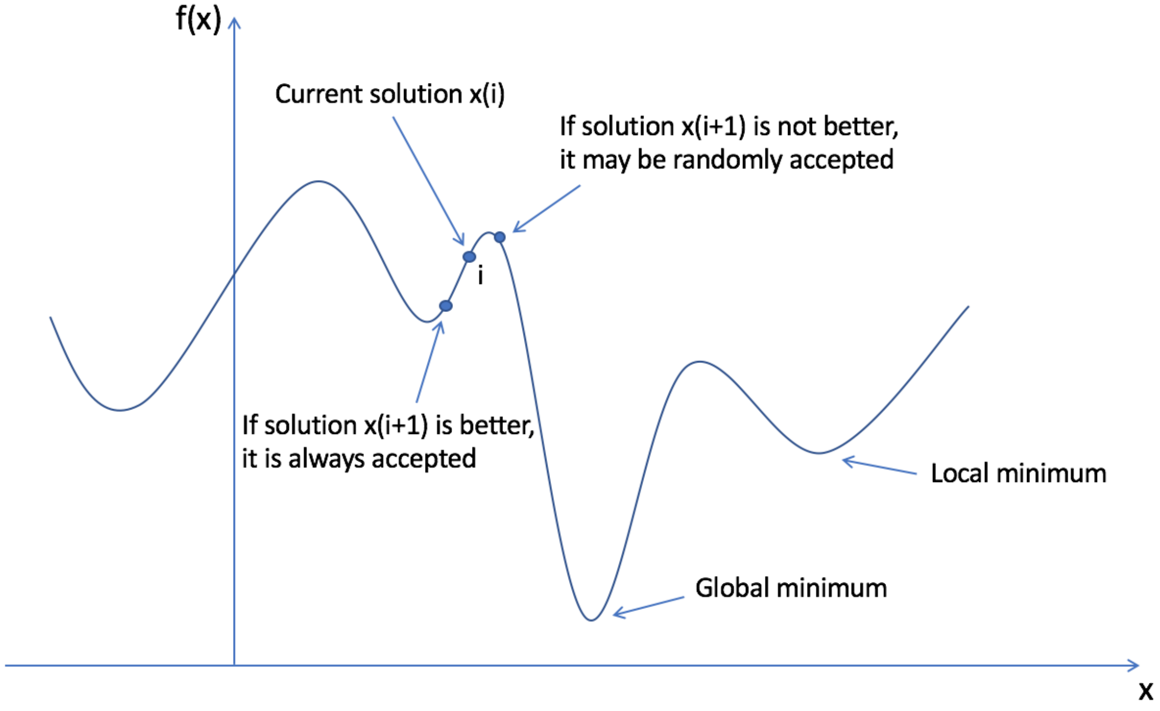

Figure 2.3 Graphical representation of the general SA optimization process depicting the process of accepting a solution. f(x) is the objective function that is evaluated at a solution x.

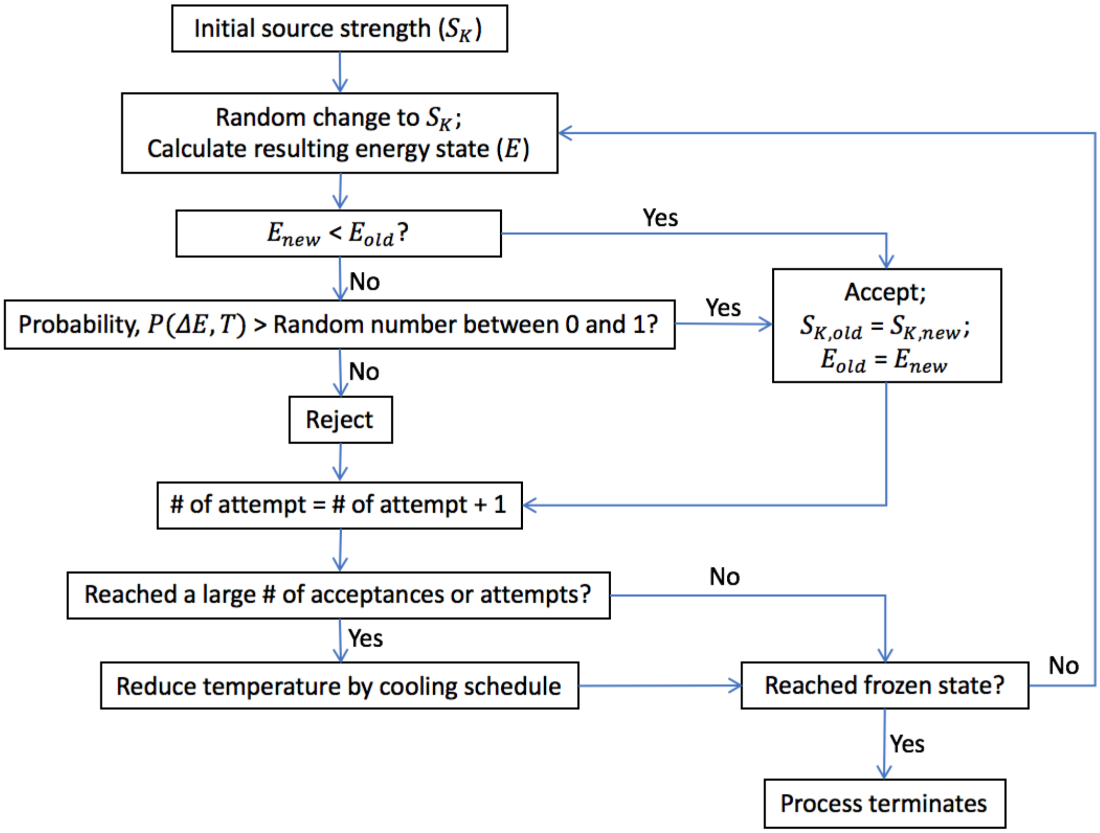

Figure 2.4 A flowchart showing the general steps of the SA algorithm.

2.2.2 Applications of the SA algorithm in radiotherapy

In the past, SA has been used in numerous applications for inverse treatment planning for radiotherapy. Many studies have applied SA in EBRT [11,12]. Webb in 1991 used SA in three-dimensional conformal treatment planning using radiation fields defined by a multileaf collimator for optimizing the choice of beam weights to minimize dose to organs at risk whilst aiming towards a uniform dose distribution in the target volume [11]. It was shown that using the SA technique, either an optimal set of single beam weight per field could be generated if there is just a target volume, or two beam weights per field with spatially modulated intensity could be generated if there are both a target volume and organs at risk in the beam's line of sight. SA was first applied to brachytherapy by Sloboda in 1992, who used the algorithm in the inverse planning of a vaginal treatment [13]. In his application, which consisted of several variations of a hypothetical low-dose rate vaginal vault planning problem, SA algorithm was used to generate a set of integer weights, one for each available source position within a vaginal vault applicator, which are interpreted in terms of configuration occupancy numbers for static source arrangements and relative dwell times for single stepping sources. The algorithm found solutions of high quality for all problem variants. Moreover, there also have been numerous studies that applied the SA algorithm to prostate brachytherapy [15,16]. Lessard *et al.* developed an anatomy-based dose optimization algorithm for high-dose rate brachytherapy of the prostate using fast SA and dedicated objective function reflecting clinical prescription and constraints [15]. The algorithm was used to optimize the dwell times of seeds inside catheters which get inserted in the prostate. The focus of the investigation was on evaluating the capability of the algorithm to meet the physician's prescription and constraint instead of on the technical limitations. Consequently, it was found that the physician's control on the treatment was improved. The developed algorithm was found to be able to automatically and rapidly (<1 minute of computation time) generate dwell time distribution that achieves highly conformal dose coverage to the target volume which can avoid inducing overdosage of urethra and normal tissues surrounding the prostate.

In this work, the SA algorithm was applied to inverse planning of ocular brachytherapy for the first time. As a final output of the investigation, the developed algorithm finds an optimal distribution of differential seed strengths in order to improve dose conformity, increasing the likelihood of eye preservation and vision sparing relative to conventional manual planning. Since this is a challenging problem that requires implementations of various components, we first began by implementing the plaque geometry, dose calculations, as well as verifying the functionality of the annealing algorithm for a general problem which is described in the next chapter.

2.3 References

[1] Nath R, Anderson LL, Luxton G, Weaver KA, Williamson JF, Meigooni AS. Dosimetry of interstitial brachytherapy sources: recommendations of the AAPM Radiation Therapy Committee Task Group No. 43. American Association of Physicists in Medicine. *Med Phys.* 1995;22(2):209-234.

[2] Chiu-Tsao ST, Astrahan MA, Finger PT, et al. Dosimetry of ^{125}I and ^{103}Pd COMS eye plaques for intraocular tumors: Report of Task Group 129 by the AAPM and ABS. *Med Phys.* 2012;39(10): 6161-6184.

[3] Astrahan MA. Improved treatment planning for COMS eye plaques. *Int J Radiat Oncol Biol Phys*. 2005;61(4):1242.

[4] Beaulieu L, Tedgren AC, Carrier JF, et al. Report of the task group 186 on model-based dose calculation methods in brachytherapy beyond the TG-43 formalism: Current status and recommendations for clinical implementation. *Med Phys*. 2012;39(10):6208-6236.

[5] Morrison H, Menon G, Larocque MP, Veelen B, Niatsetsk Y, Weis E, Sloboda RS. Advanced Collapsed cone Engine dose calculations in tissue media for COMS eye plaques loaded with I-125 seeds. *Med Phys.* 2018;45(7):3349-3360.

[6] University of California, San Francisco (UCSF), Department of Radiation Oncology. Inverse planning simulated annealing (IPSA). https://radonc.ucsf.edu/inverse-planning-simulated-annealing-ipsa. Updated 2015. Accessed January 23, 2019.

[7] Shepard D. IMRT optimization algorithms. *The American Association of Physicist in Medicine (AAPM)* [Available: https://www.aapm.org/meetings/amos2/pdf/49-14369-92189-877.pdf]. 2007.

[8] Bortfeld T. Optimized planning using physical objectives and constraints. *Semin Radiat Oncol*. 1999;9(1):20-34.

[9] Ezzell GA. Optimization in brachytherapy. *Ch22, AAPM Brachytherapy Society Summer School*, July 2005, Seattle WA; 415-34.

[10] Kirkpatrick S, Gelatt CD, Vecchi MP. Optimization by simulated annealing. *Science*. 1983;220(4598):671-680.

[11] Webb S. Optimization by simulated annealing of three- dimensional conformal treatment planning for radiation fields defined by a multileaf collimator. *Phys Med Biol*. 1991;36(9):1201-1235.

[12] Dias J, Rocha H, Ferreira B, Lopes Mdo C. Simulated annealing applied to IMRT beam angle optimization: A computational study. *Phys Med*. 2015;31(7):747-756.

[13] Sloboda RS. Optimization of brachytherapy dose distributions by simulated annealing. *Med Phys*. 1992;19(4):955-964.

[14] Kubicky CD, Yeh BM, Lessard E, et al. Inverse planning simulated annealing for magnetic resonance imaging-based intracavitary high-dose-rate brachytherapy for cervical cancer. *Brachytherapy*. 2008;7(3):242-247.

[15] Lessard E, Pouliot J. Inverse planning anatomy-based dose optimization for HDR-brachytherapy of the prostate using fast simulated annealing algorithm and dedicated objective function. *Med Phys*. 2001;28(5):773-779.

[16] Jacob D, Raben A, Sarkar A, Grimm J, Simpson L. Anatomy-based inverse planning simulated annealing optimization in high-dose-rate prostate brachytherapy: Significant dosimetric advantage over other optimization techniques. *Int J Radiat Oncol Biol Phys*. 2008;72(3):820-827.

[17] Du KL, Swamy M. Simulated annealing. In: *Search and optimization by metaheuristics.* Switzerland: Birkhäuser; 2016:29-36.

[18] Metropolis N, Rosenbluth AW, Rosenbluth MN, Teller AH, Teller E. Equation of state calculations by fast computing machines. *Journal of Chemical Physics*. 1953;21(6):1087-1092.

[19] Morrill SM, Lam KS, Lane RG, Langer M, Rosen II. Very fast simulated reannealing in radiation-therapy treatment plan optimization. *Int J Radiat Oncol Biol Phys*. 1995;31(1):179-188.

Chapter 3 Implementation of simulated annealing algorithm in plaque brachytherapy planning

3.1 Introduction

A fully-functioning dose optimization algorithm requires several distinct components. Tumor and source geometry must be properly modelled. The dose distribution resulting from this source geometry must be correctly calculated according to accepted methodology. An optimizer must be able to adjust source strengths and evaluate potential solutions using a user-determined objective function, and iterate towards better solutions. Proper functioning of the overall algorithm assumes correct implementation of each subcomponent. Therefore, prior to developing a complex dose optimization algorithm for a desired application, initial implementation and verification of the basic parts of the algorithm must be evaluated. This process also allows one to assess its suitability for full implementation.

In this study, the simulated annealing (SA) algorithm is being investigated for application in ocular plaque brachytherapy. This chapter describes the initial implementation of the SA algorithm for inverse planning in plaque brachytherapy, and reports on the potential of the algorithm in tackling two test problems: 1) dose optimization using uniform seed strengths, and 2) maximizing dose uniformity across tumor base using differential seed strengths. The first problem essentially allows the user to verify the correct implementation of the COMS plaque geometry, the TG-43 dose calculation, as well as the general steps used in the SA algorithm. The second problem serves as a tool for verifying that the algorithm can find the minima in the energy function when using differential seed strengths since improvements in uniformity are easy to verify both visually and numerically. Hence, investigating these two test problems served to verify the correspondence with Plaque Simulator and proper functionality of the optimization scheme before solving the actual problem of improving the sparing of critical structures of the eye with achievement of tumor coverage which is described in Chapter 4.

In the first part of this chapter, a full eye model was built in the developed algorithm and the COMS plaque geometry was added. Also, dose calculations using the TG-43 formalism were implemented.

In the second part, the SA algorithm was applied to solve for uniform seed strength that achieves the prescription dose to tumor apex. The resulting dose to apex was then compared to that given by Plaque Simulator, the clinical planning software, to verify the correspondence in dose calculations. In the last part, a new algorithm was developed to generate different seed strength for each seed in a plaque such that the resultant dose variation across the basal dose is reduced as much as possible. For verification, the resultant dose profile along the tumor base was compared to that from Plaque Simulator as well as dose to apex was checked for both methods to ensure that dose renormalization for desired dose at the apex is achieved.

3.2 Methods and Materials

Treatment details:

For this study, the COMS plaques were utilized, which have diameters ranging from 10 to 22 mm [1]. Tumors of different basal dimensions (planning target volume (PTV) base (= gross tumor volume (GTV) base + 2 mm margin); equal to plaque diameters) and heights (3.5, 5, and 8 mm, representative of small, medium, and tall tumors, respectively) treated with a prescription dose of 70 Gy, delivered over 4 days, to the prescription point (tumor apex, which at our institution is taken to be at a minimum height of 3.5 mm i.e. any tumors with smaller heights are increased to 3.5 mm) were considered in all cases. The radioactive source used in this study was the Advantage I-125 seed (model IAI-125A, IsoAid LLC, Port Richey, FL), which is available for clinical use with source strengths from 0.9 to 15 U. The SA algorithm routines for solving the problems were developed using the Matlab software (v2017b, The MathWorks Inc., Natick, MA).

3.2.1 Modelling of tumor and seed geometry

Before solving any problem, a modelling tool was needed through which the tumor and plaque of interest, as well as the resulting tumor dose distribution, could be visualized in order to run various simulations that would assist in solving the problems. An example of a desirable visualization is shown in Figure 3.1, which includes a tumor on the inner sclera, locations of seeds, and resultant dose distribution.

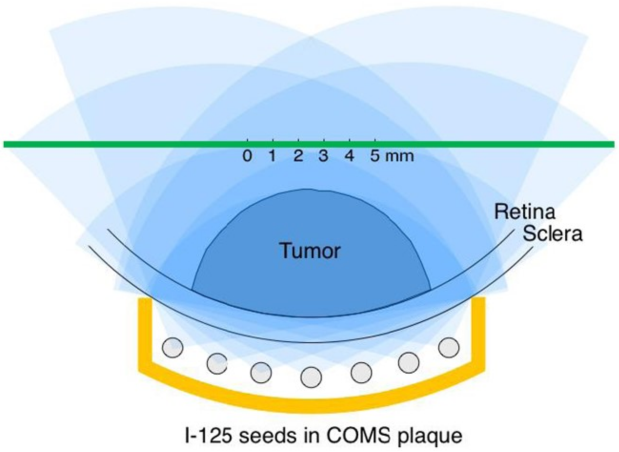

Figure 3.1 A visualization of an ocular tumor and seeds within a plaque that was desired to be modelled in the algorithm (image reproduced from https://www.eyephysics.com/PS/Index.html with permission from Astrahan).

Using the coordinate system specified in the TG-129 document (Figure 3.2), the eye was approximated as a perfect sphere with a radius of 11.3 mm (from the centre of the eye to inner sclera), and the tumor was taken as the upper hemisphere of an ellipsoid whose base (defined by semi-major and semi-minor axes that are halves of the GTV basal dimensions) was approximated to have a spherical curvature that coincides with that of the inner scleral surface [1].

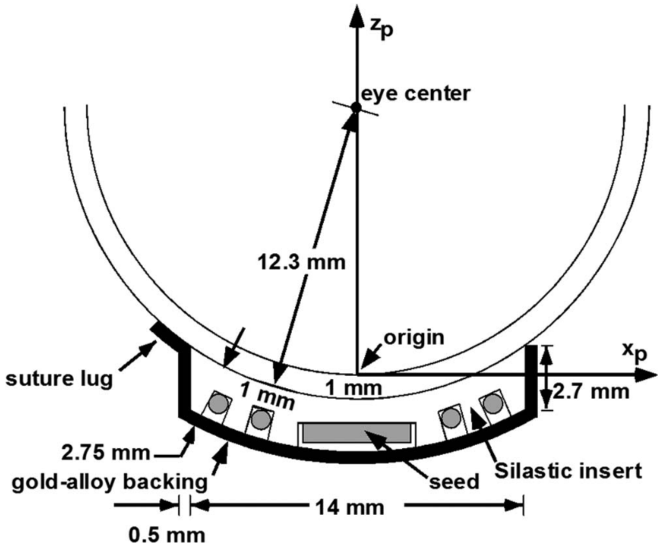

Figure 3.2 Coordinate system used in the TG-129 report (image reproduced from Chiu-Tsao, et al. with permission from Medical Physics [1]).

The basal shape was initially taken as being circular for simplicity but was later generalized to be elliptical (see Section 4.2.2.1). The 2 mm tumor basal margin, which is the arc length along the spherical surface, was also added to the GTV basal dimensions. The height of tumor apex was used to define the height of the half ellipsoid (used to construct the tumor volume). To construct the 3D tumor structure, points were defined using parametric equations of an ellipsoid [2]:

$$\begin{aligned} x &= a \cdot \cos(\theta) \cdot \sin(\phi) \\ y &= b \cdot \sin(\theta) \cdot \sin(\phi) \\ z &= c \cdot \cos(\phi), \end{aligned} \qquad \text{(Eq. 3.1)}$$

for the lateral part (i.e. PTV excluding the base), and using equations of a sphere (Eq. 3.1 with $a=b=c$) for the basal part. In (Eq. 3.1), a, b, and c are the lengths of the semi-axes, θ is the polar angle and ϕ is the azimuthal angle of the point (x, y, z) of the ellipsoid. These points were then plotted together to form the 3D tumor volume. Furthermore, the seed coordinates of the COMS plaques were taken directly from the TG-129 report [1]. For dose calculations, the point at the tumor apex and the points defined for the PTV base were taken as dose calculation points in general (additional dose points were defined when necessary).

3.2.2 Test 1: Evaluation of SA algorithm for dose optimization using uniform seed strengths

In Plaque Simulator, uniform strength for all seeds is directly calculated given the prescription dose and seed geometry. In the algorithm, this calculation can also be done directly instead of using an optimization process, to verify dose calculation against Plaque Simulator. However, optimization was used instead (to find the known uniform seed strength) in order to verify the general steps of the SA algorithm along with dose calculation. In other words, this part served as a test to compare the correspondence with Plaque Simulator before complexity is introduced in the optimization routine. In this problem, the basic SA algorithm was written to generate an optimization routine to solve for uniform source strength for all seeds within a plaque that best achieves the prescription dose to tumor apex (Figure 3.3).

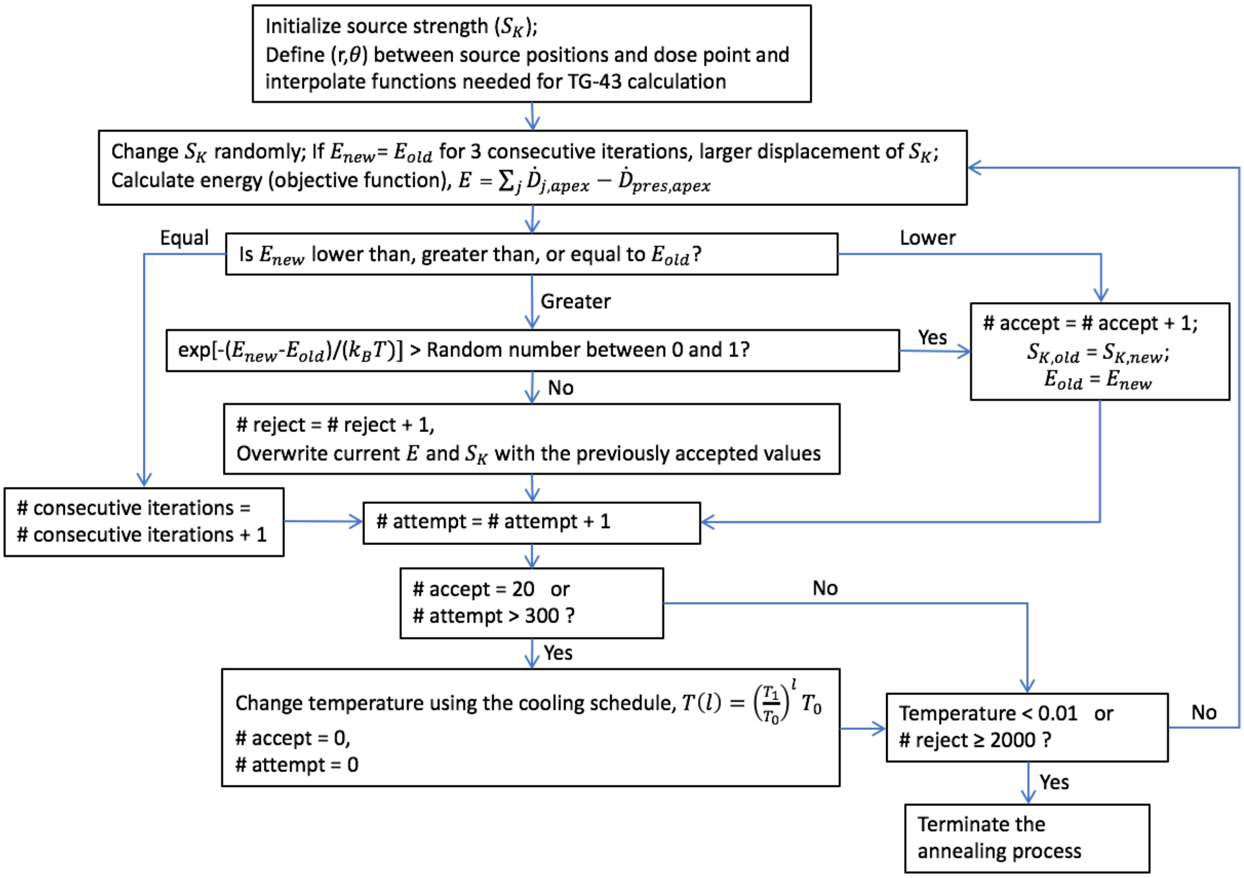

Figure 3.3 The SA algorithm applied to solve for uniform seed strength S_K to deliver the prescription dose at the apex for a plaque brachytherapy treatment.

Starting with an initial source strength S_K, a random transition to S_K is generated at each iteration k. The algorithm then calculates the resulting energy, $E = \sum_j \dot{D}_{j,apex} - \dot{D}_{pres,apex}$, which is the difference between the calculated and prescribed dose rate at apex, with j being a seed position. For evaluating the new transition at k-th iteration, the energy difference $\Delta E = E(k) - E(k-1)$ is calculated. If $\Delta E < 0$, or the new energy is lower than the old energy, the transition is always accepted. If $\Delta E > 0$, or the new energy is higher, the transition is still accepted with a probability,

$$P(\Delta E, T) = \exp\left(-\frac{\Delta E}{k_B T}\right), \qquad \text{(Eq. 3.1)}$$

where T is the effective temperature and k_B is the Boltzmann constant. If P is greater than a random number between 0 and 1, the new transition is accepted and is used to make the next step.

Otherwise, it is rejected and the old state is retained. This procedure is repeated, at the same temperature, until a large enough number of acceptances or attempts is reached. Then, the temperature is decreased by a cooling schedule chosen by the user. Among the many attempts that have been made to derive and suggest effective schedules, the logarithmic cooling scheme introduced by Geman and Geman [3],

$$T(l) = \frac{c}{\log(1+l)}, \qquad \text{(Eq. 3.2)}$$

has a special theoretical importance with l being the step count for temperature and c being a constant that is independent of l. They proved that, for c greater than or equal to the depth (energy barrier) of the deepest local minimum, this schedule will lead the system to the global minimum state in the limit of infinite time. However, due to its extremely slow temperature decrease, this schedule is not practical for the current problem. Hence in this study, a fast cooling schedule proposed by Kirkpatrick *et al.* [4] was chosen, which cools exponentially as:

$$T(l) = \left(\frac{T_1}{T_0}\right)^l T_0, \qquad \text{(Eq. 3.3)}$$

where T_0 is the initial effective temperature, and T_1 is the effective temperature at the first decreased step. This schedule involves first ‘melting’ the system at an initial high effective temperature T_0, then repeatedly lowering the temperature by a constant factor $\frac{T_1}{T_0}$ ($0 < \frac{T_1}{T_0} < 1$), taking enough steps at each temperature to keep the system close to equilibrium, until the system approaches the lowest energy state. For this particular problem, it was found empirically that varying the $\frac{T_1}{T_0}$ ratio, which determines the steepness of the exponential curve for the temperature cooling, had no significant impact on the result for S_K; it was hence chosen to be 0.1 - 0.9. This procedure of iterating for random transitions to S_K for k times and then changing the temperature is repeated until a sufficiently low temperature is reached, at which the system is considered “frozen”. The annealing process is then terminated. The relevant technical issues for implementing the SA algorithm are addressed below.

Initial temperature, T_0

The initial effective temperature was chosen empirically to be a high value, such as T_0=5-10, in order to “melt” the system. At this temperature, most configurations are accepted even if they increase the energy from the previous iteration.

Initial source strength, S_K

It was empirically found that there was no significant change in the resultant solution for using any value of initial S_K, such as from 0 to 100 U. However, since the commercially available range for S_K is 0.9 to 15 U, a value within this range was used as the initial S_K.

Random displacement generation

The random transition of S_K at each step was chosen to be a decreasing number times a normally distributed random number (with mean 0 and standard deviation 1). This decreasing number, starting from 1, was set to exponentially decrease in every iteration. This initially gives relatively larger displacements to keep the solutions off local extrema, and then smaller displacements as iterations proceed to avoid metastable solutions that result from continuously using wide steps. If a solution is initially too far away from the optimal value, having larger displacements in the beginning of the search will help bring it closer to the optimal value. Also, if the resultant new energies equal the old energies for three consecutive iterations, which indicate that the current solution may be too far away from the optimal solution, the displacement was increased to 10% of the initial S_K to give a bigger jump to the solution. The random transition was then dropped back to the original smaller range. This approach has been proven effective in other brachytherapy optimization problems [5].

Stopping criteria

Stopping criteria are required for: (a) making random transitions to S_K at each temperature and (b) the entire annealing process. For (a), at each temperature, the simulation must proceed long enough for the system to reach a steady state and therefore, sufficient S_K transitions are attempted such that either there are 20 accepted transitions, or the number of attempts exceeds 300. This stopping criterion has worked well in other applications, and experimental verification in this chapter will confirm that it is effective within this current optimization scheme [5]. For (b), theory suggests a final temperature equal to zero at which point the system is “frozen” [6]. In practice, it is not necessary to let the temperature reach zero because as it approaches zero, the probability of accepting a worse configuration is negligible, being almost the same as that for the temperature being equal to zero [6]. Hence, the stopping criteria can either be a suitably low temperature (e.g. $10^{-15} \leq T \leq 10^{-2}$) or when the system is considered “frozen” at the current temperature, i.e. new configurations are being rejected for a large number of times (≥ 2000) [5,6].

This SA algorithm was run to generate the uniform seed strengths which were then manually input into Plaque Simulator to compare the resulting dose to apex for various plaque sizes and tumor heights.

3.2.3 Test 2: Maximizing dose uniformity across tumor base

Maximizing dose uniformity across tumor base is a clinically relevant problem as there is often significant variation in the basal dose with resultant hot spots when equal seed strengths are used. These hot spots may lead to unnecessarily high maximum doses to sclera. In this problem, the objective was to determine a different source strength for each seed within a plaque such that dose uniformity across the PTV base is maximized while the prescription dose is delivered to the prescription point. The SA algorithm was modified to solve this problem and the steps involved are shown as a flowchart in Figure 3.4.

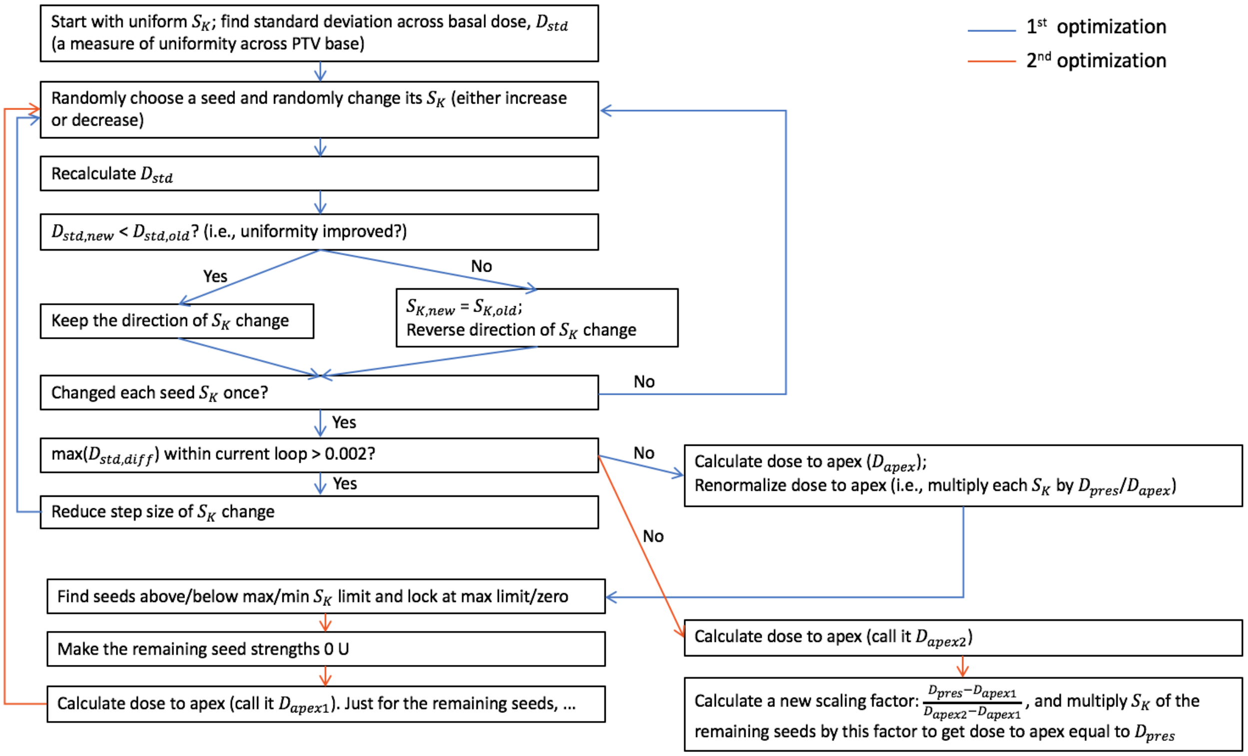

Figure 3.4 The algorithm developed for maximizing basal dose uniformity using differential seed strengths for plaque brachytherapy.

Starting with uniform strengths, the initial standard deviation (as a measure of uniformity) of basal dose is calculated. Then, a seed is randomly chosen and its strength is randomly changed. The new standard deviation of basal dose is calculated and if it is better than that in the previous iteration, the new strength is accepted and if not, it is rejected and the direction of the strength change is reversed. After iterating for each seed once, the step size of the strength change is reduced and the process is repeated until uniformity does not improve anymore (i.e. difference in standard deviation between two consecutive iterations is less than or equal to 0.002%). After renormalizing the dose to apex, if any seed has reached the seed strength limit (minimum 0.9 U, maximum 15 U), the second optimization process is initiated to impose the limit. Those seeds that have reached the limit are locked (i.e. they are not included in the iterations anymore), and the first optimization process is performed again on the rest of the seeds. When uniformity does not improve anymore, dose is renormalized to the apex by scaling those seeds that were re-optimized. The algorithm was run for plaque sizes of 12, 16, and 22 mm and tumor heights of 3.5, 5, and 8 mm and, for verification, the resulting dose profile along the PTV base was generated and compared with that from Plaque Simulator, which was generated by manually inputting the source strengths obtained by the algorithm. Moreover, the resulting dose to apex using the algorithm and Plaque Simulator were examined to ensure that the prescription dose of 70 Gy was being achieved.

3.3 Results and Discussion

3.3.1 Modelling of tumor and seed geometry

The tumor and plaque models were built for use in the simulations (Figure 3.5). The tumor and the seeds of a plaque are visualized as a 3D plot when the user inputs plaque size, tumor height, and tumor basal dimensions. Also, if seed strengths and treatment length are specified, the resulting dose distribution over the PTV base is calculated and plotted along with the tumor and the seeds.

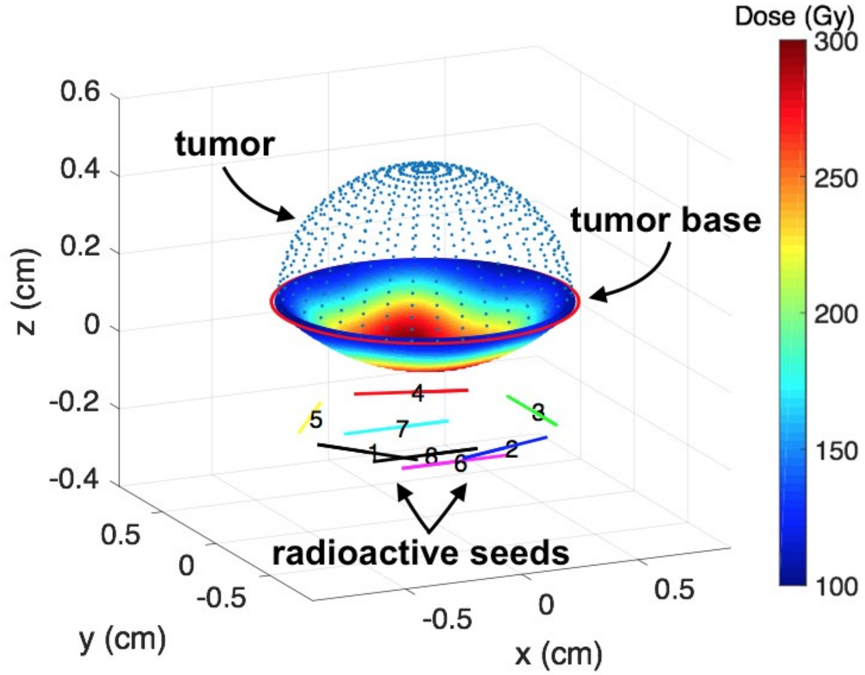

Figure 3.5 3D depiction of a 5 mm tall tumor model and the seed geometry for a 12 mm plaque. The lip of the plaque (red line around the PTV base) and the basal dose distribution using uniform seed strengths are shown.

3.3.2 Test 1: Evaluation of SA for dose optimization using uniform seed strengths

Dose normalization using uniform strength is a task that Plaque Simulator can easily perform. Hence it is useful for benchmarking the algorithm for functionality and correspondence with Plaque Simulator before any further development of the algorithm. Through this test, the correspondence in dose calculations with Plaque Simulator could also be verified.

Figure 3.6 shows the percent difference between the dose to apex from the SA algorithm and Plaque Simulator. All differences were found to be within 4.5%. The minimum difference was 0.2% for the 16 mm plaque and 3.5 mm tumor height, the maximum was 4.4% for the 22 mm plaque and 5 mm tumor height, and the median of all cases was found to be 1.7%. For the 3.5 and 5 mm tumor heights, the difference was observed to increase, with some inconsistency, for increasing plaque size. For the 8 mm tumor height, differences were found to be very similar for all plaque sizes.

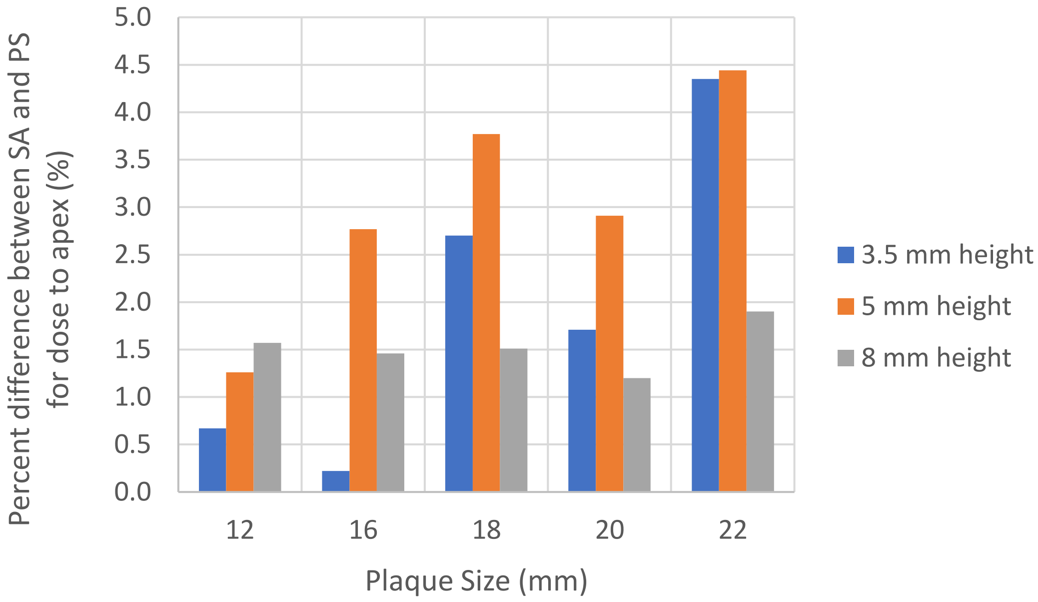

Figure 3.6 A plot of percent dose difference at the apex between SA algorithm and Plaque Simulator as a function of plaque size for three different tumor heights.

The observed dose differences can be attributed to differences in the values of the TG-43 dosimetry parameters. The values or sources of the values of dosimetry parameters used in this work and in

Plaque Simulator are shown in Table 3.1 and Figure 3.7. Plaque Simulator performs dose calculations using the TG-43 formalism (Eq. 2.1), which relies on tabulated data based on experimental measurements (using thermoluminescent dosimeters) and Monte Carlo (MC) simulation (obtained using the Monte Carlo N-Particle (MCNP) code, a general purpose MC particle transport code) [7,8]. The dose rate constant (Λ) was determined by taking an average of the experimental measurement and MC values, and its overall uncertainty was found to be 4.8% [7]. The data for the radial dose function ($g(r)$) and anisotropy function ($F(r,\theta)$) were taken from the MC simulation values obtained using the MCNP code for radial distances, r and polar angles, θ. These data tables for $g(r)$ and $F(r,\theta)$ have a coarse resolution and thus, Plaque Simulator uses an interpolation/extrapolation scheme which adds further uncertainties. On the other hand, this work used the values of the above dosimetry parameters from Taylor and Rogers [9] as presented in the Carleton Laboratory for Radiotherapy Physics (CLRP) TG-43 parameter database [10], which are entirely from MC simulation values obtained using the egs_brachy code, a MC-based user code for rapid brachytherapy dose calculations [11]. These data were calculated with a finer resolution than the TG-43 tables, which provides more accuracy. For the MC simulation values in both sources of data, the involved uncertainty is not only statistical, but also involves several others (source construction, source movable internal components, source emissions/photon spectrum, measurement phantom geometry and composition, radiation transport code, interaction and scoring cross sections, and energy deposition scoring algorithms) as described in the TG-138 document [12]. The uncertainty in each of these is fairly low, usually <1% [13]. The combined uncertainty for the dose rate 1 cm along the transverse axis of the IAI-125A I-125 seed has been found to be >1% [13]. Specifically, the uncertainties for Λ and $g(r)$ have been found to be about 1.2% and 1.6%, respectively [13]. Overall, the CLRP data is considered more accurate and thus was used in this work. In Figure 3.7, the radial dose function and anisotropy function (at r=0.5 cm) used in each system are plotted for comparison. The data from the two sources are generally in good agreement, however, some deviations are observed. For $g(r)$ (Figure 3.7a), there is some noticeable deviation close to the seed (r <0.5 cm) and also farther away from the seed ($r \geq 6$ cm). Also, for $F(r,\theta)$ (Figure 3.7b), a noticeable deviation is found at $\theta \leq 10^\circ$; this discrepancy is thought to be due to differences in the simulated endweld thickness of the seed used in the calculations (0.24 mm in Plaque Simulator and 0.10 mm in the SA algorithm) [13]. Also, the $g(r)$ and $F(r,\theta)$ used in Plaque Simulator were each normalized by a geometry function that had differences from the standard line source approximation close to the source [14]; this may explain the deviations observed close to the seed. Another source of discrepancy for both parameters is the use of different simulation conditions in each MC code, such as cross-section library and photon energy spectrum [13]. It is also evident in the figure that the Plaque Simulator data has a coarser resolution, as mentioned earlier. These differences potentially contributed to the differences observed in the doses to apex shown in Figure 3.6.

Table 3.1 Comparison of the values or sources of the values of dosimetry parameters used in Plaque Simulator and in the SA algorithm.

	Plaque Simulator	SA algorithm	% Difference
Dose rate constant Λ (cGyh^{-1}U^{-1})	0.981 [8]	0.924 [9]	5.81
Radial dose function $g(r)$	TG-43, IAI-125A [8]	CLRP, IAI-125A [10]	Figure 3.7a
Anisotropy function $F(r,\theta)$	TG-43, IAI-125A [8]	CLRP, IAI-125A [10]	Figure 3.7b

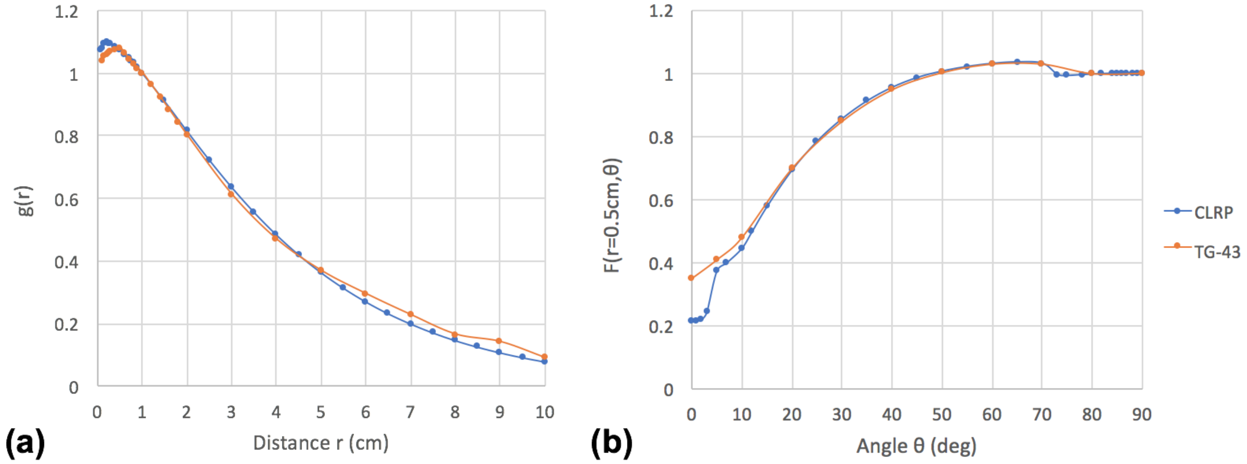

Figure 3.7 Comparison of dosimetry parameters (a) radial dose function $g(r)$, and (b) anisotropy function $F(r = 0.5\ cm, \theta)$, used in the SA algorithm (CLRP data) and Plaque Simulator (TG-43 data).

Another source for the inconsistency observed between the SA algorithm and Plaque Simulator, is due to the different COMS seed coordinates used in both calculations. This work used the seed coordinates provided in the TG-129 document; those used by Plaque Simulator are slightly different from these seed coordinates because the seed coordinates in each of the TG-129 and

Plaque Simulator were independently determined using measurements from scanned images of the plaque inserts [1,15]. Using the seed coordinates from Plaque Simulator in the SA algorithm, the difference in dose to apex (using a fully loaded plaque) was found to be within 1%, thus adding to the observed differences.

Plaque Simulator dosimetry has been compared against multiple MC models and a model-based dose calculation algorithm, as well as experimental measurements [16,17,18,19]. In one example, Plaque Simulator calculated doses agreed with Gafchromic film measurements within 5% (being greater or smaller at different depths with no consistent pattern) along the plaque's central axis for most depths and plaque sizes analyzed [19]. Therefore, the observed difference of 4.5% seen in this work can be considered to be reasonable; inherent differences are expected to exist between the calculated and actual dose even if the exact values (dosimetry parameters and seed coordinates) used by Plaque Simulator were taken.

3.3.3 Test 2: Maximizing dose uniformity across tumor base

When using equal seed strengths, there often results regions of hot spots on sclera that are clinically undesirable; this can be avoided by using differential seed strengths that would largely increase dose uniformity across the PTV base while delivering the prescription dose to the tumor apex. Solving this problem can also serve as a worthy tool for assessing future changes to the algorithm as it would provide the foundation for solving more complex problems.

2D basal dose distribution for a 5 mm tall tumor treated with a 12 mm plaque (to treat a tumor with a basal diameter of 8 mm + 2 mm margin) obtained by using uniform (Test 1) and differential seed strengths (Test 2) are shown in Figures 3.8a and 3.8b, respectively. Similarly, basal dose distributions for an 8 mm tall tumor treated with a 16 mm plaque are shown in Figures 3.8c and 3.8d. For both cases, dose profiles along the PTV base at x=0 (along the y-axis) using uniform and differential loading are shown in Figure 3.9. To quantify the reduction in dose variation, standard deviation in the tumor basal dose was calculated when using differential seed strengths for various plaque sizes and tumor heights, and compared with that obtained using uniform seed strengths (Table 3.2). Average reduction in dose variation for 3.5, 5 and 8 mm heights were found to be 33.1%, 33.3%, and 27.1%, respectively. The differential seed strengths calculated by the SA algorithm for the cases shown in Figure 3.8 were manually input into Plaque Simulator for comparison of dosimetry. The dose profiles along the PTV base at x=0 (along the y-axis) for a 5 mm tall tumor treated with a 12 mm plaque, and an 8 mm tall tumor treated with a 16 mm plaque given by the two systems are shown in Figure 3.10. Additionally, dose to apex using the algorithm and Plaque Simulator for the specified tumor and plaque sizes are displayed in Table 3.3.

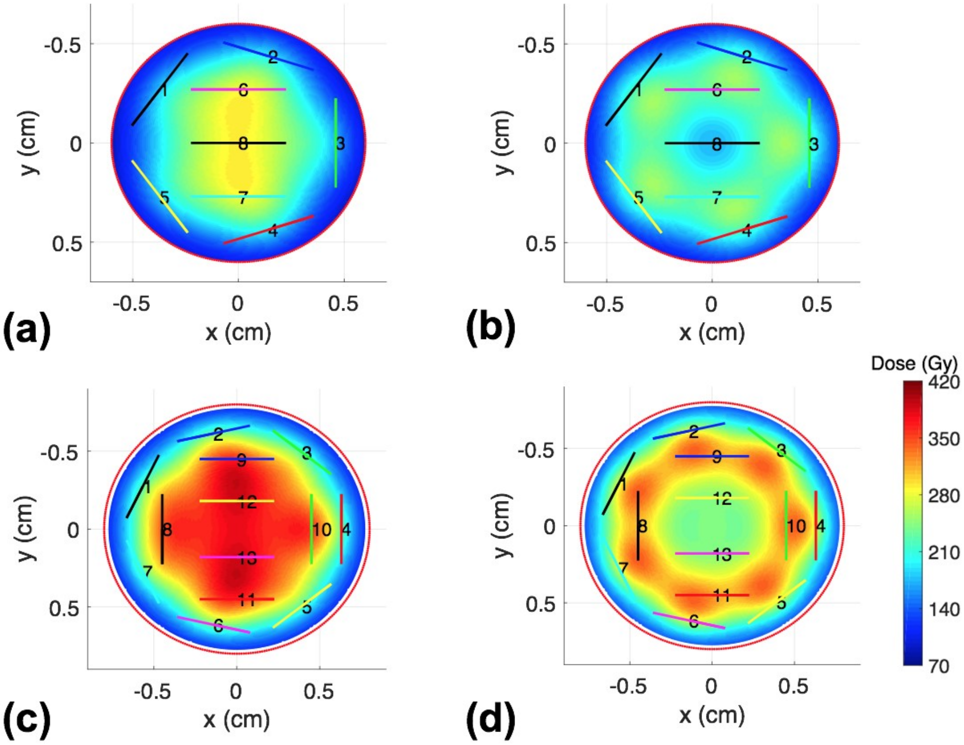

Figure 3.8 2D views of the basal dose distribution, generated using the developed algorithm for (a,b) a 5 mm tall tumor treated with a 12 mm plaque, and (c,d) an 8 mm tall tumor treated with a 16 mm plaque are shown for cases using uniform seed strengths (a,c) and differential seed strengths (b,d) for maximizing basal dose uniformity.

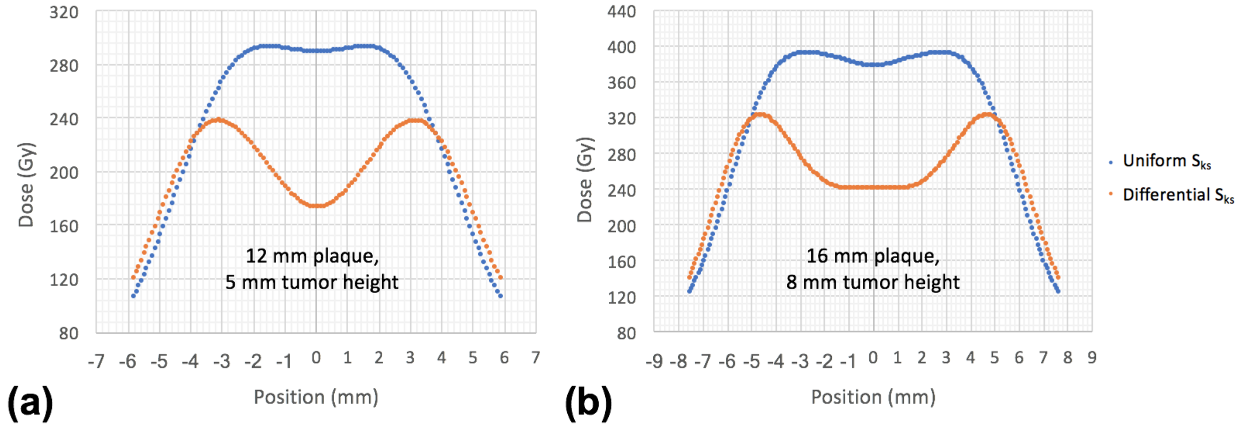

Figure 3.9 Dose profiles, calculated using the SA algorithm, along the PTV base at x=0 using uniform and differential loading for (a) a 5 mm tall tumor with a 12 mm plaque, and (b) an 8 mm tall tumor with a 16 mm plaque.

Table 3.2 Standard deviation in the tumor basal dose (%) for different plaques sizes and tumor heights using uniform and differential seed strengths.

Tumor height	Plaque size	% standard deviation in tumor basal dose			Average
		12 mm	16 mm	22 mm	
3.5 mm	uniform strengths	31.2	33.4	42.3	35.6
	differential strengths	20.4	23.1	28.0	23.8
	average reduction				**33.1%**
5 mm	uniform strengths	31.2	33.4	42.3	35.6
	differential strengths	20.4	23.1	27.9	23.8
	average reduction				**33.3%**
8 mm	uniform strengths	31.2	33.4	42.3	35.6
	differential strengths	27.2	22.8	27.9	26.0
	average reduction				**27.1%**

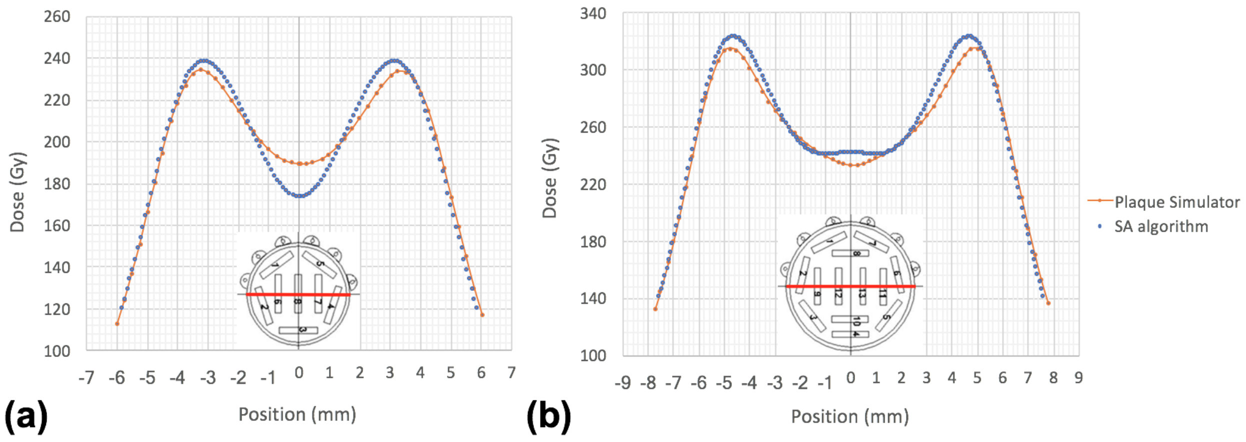

Figure 3.10 Dose profiles along the PTV base at x=0 for (a) a 5 mm tall tumor treated with a 12 mm plaque, and (b) an 8 mm tall tumor treated with a 16 mm plaque, resulting from the use of differential seed strengths for maximizing basal dose uniformity given by the developed algorithm and input into Plaque Simulator (inset plaque figures adapted from Chiu-Tsao, *et al*. [1]).

Table 3.3 Dose to apex using the developed algorithm and Plaque Simulator for various tumor and plaque sizes.

Tumor height (mm)	Plaque size (mm)	Dose to apex (Gy)		% Difference
		Algorithm	Plaque Simulator	
3.5	12	70.1	68.4	2.37
	16	69.9	69.0	1.29
	22	69.9	74.1	5.95
5	12	69.9	71.5	2.29
	16	70.1	72.5	3.42
	22	70.0	73.5	5.00
8	12	70.0	71.4	2.06
	16	69.9	71.1	1.72
	22	69.9	71.6	2.43

From Figures 3.8, 3,9 and Table 3.2, it can be confirmed both visually and numerically that the basal dose uniformity was significantly improved with the use of seeds of different strengths. For both cases shown in Figures 3.8 and 3.9, uniform loading resulted in a hot region towards the center of the base as this region received increased overall contributions from all the seeds. However, with differential loading, this hot region in the center was significantly reduced and the overall basal doses became more uniform as the optimizer redistributed the strengths of the central seeds to the peripheral ones. As well, the resulting dose distribution for both cases is symmetric across the centre of the base; this pattern is also reasonable for the optimizer to obtain because as the optimizer tried to reduce hot spots in the central region, the S_K of each peripheral seed was brought to about the same magnitude as the other seeds. If the loading of the peripheral seeds was asymmetric, it would create hot spots in the peripheral region of the base compared to those obtained in the figures. This is because the loaded seeds together need to deliver the desired dose to the apex (on the central axis of the plaque) and if there is a seed of lower strength, it must be compensated by other seed/s being stronger, which would increase the basal dose variation. Hence, these results verify the proper operation of the developed algorithm. Furthermore, as shown in Table 3.2, the fact that the reduction of hot spots was observed for all tumor heights and plaque sizes tested, proves the consistency of the results and thus the strength of the developed algorithm.

The dose profiles in Figure 3.10 reveal that doses given by the SA algorithm and Plaque Simulator are generally very similar except for deviations observed around the two peaks and the center. These deviations are expected to arise from those differences discussed previously for Test 1, i.e. due to the differences in the seed coordinates and the TG-43 parameters. But as mentioned, we believe our results to be more accurate. The dose difference observed at the center (0 mm) in Figure 3.10a is larger than in Figure 3.10b; this could be due to the dissimilarity in the seed groove positions in both plaques as shown in the plaque diagrams included in Figure 3.10. Moreover, the dose values in Table 3.3 being all relatively close to the prescription dose of 70 Gy, confirm that the algorithm always renormalized dose to apex for all cases. The slight deviations from 70 Gy for the algorithm (maximum of 0.14%) are due to the round-off errors in Matlab which converts fractional numbers into finite numbers and thus has a limited accuracy [20]. As there was a series of computations in the algorithm to calculate dose to apex, these inaccuracies added up to yield the observed deviations. The deviations of Plaque Simulator from the algorithm (maximum of 5.95%) are expected to have arisen again from the discussed differences between the SA algorithm and Plaque Simulator.

Through this test problem, it was confirmed that the developed optimization scheme correctly handles differential seed strengths, dose renormalization for desired dose at the tumor apex, and the ability of imposing limits on seed strengths. As can be seen in the steps of the algorithm, this test problem is a relatively intuitive one, with not many complicated steps involved and, therefore, serves as an acceptable test of both the dose calculation and the general framework of the optimizer. With these confirmations, the algorithm was considered acceptable for incorporating additional complexities to solve our ultimate problem of sparing critical structures while maintaining desired tumor coverage.

3.4 References

[1] Chiu-Tsao ST, Astrahan MA, Finger PT, *et al*. Dosimetry of ^{125}I and ^{103}Pd COMS eye plaques for intraocular tumors: Report of Task Group 129 by the AAPM and ABS. *Med Phys.* 2012;39(10): 6161-6184.

[2] Weisstein EW. *CRC concise encyclopedia of mathematics * 2nd ed. CRC Press; 2002:875-876.

[3] Geman S, Geman D. Stochastic relaxation, gibbs distributions, and the bayesian restoration of images. *Ieee Transactions on Pattern Analysis and Machine Intelligence*. 1984;6(6):721-741.

[4] Kirkpatrick S, Gelatt CD, Vecchi MP. Optimization by simulated annealing. *Science*. 1983;220(4598):671-680.

[5] Ren J. *Implementation of MR image-guided adaptive brachytherapy for cervix cancer* [master's thesis]. Edmonton, Alberta: University of Alberta; 2011.

[6] Yaghini M. Simulated annealing part 1: Basic concepts. http://webpages.iust.ac.ir/yaghini/Courses/AOR_881/Simulated%20Annealing_01.pdf. Updated 2009. Accessed March 30, 2019.

[7] Rivard MJ, Coursey BM, DeWerd LA, *et al*. Update of AAPM task group no. 43 report: A revised AAPM protocol for brachytherapy dose calculations. *Med Phys*. 2004;31(3):633-674.

[8] Rivard MJ, Butler WM, DeWerd LA, *et al*. Supplement to the 2004 update of the AAPM task group no. 43 report. *Med Phys*. 2007;34(6):2187-2205.

[9] Taylor REP, Rogers DWO. An EGSnrc Monte Carlo-calculated database of TG-43 parameters. *Med Phys*. 2008;35:4228–4241.

[10] Taylor REP, Rogers DWO. The CLRP TG-43 parameter database for brachytherapy. http://www.physics.carleton.ca/clrp/seed_database. Accessed March 31, 2019.

[11] Chamberland M, Taylor R, Rogers D, Thomson RM. Egs_brachy: A versatile and fast monte carlo code for brachytherapy. *Phys Med Biol*. 2016;61(23):8214-8231.

[12] DeWerd LA, Ibbott GS, Meigooni AS, *et al*. A dosimetric uncertainty analysis for photon-emitting brachytherapy sources: Report of AAPM task group no. 138 and GEC-ESTRO *Med Phys*. 2011;38(2):782-801.

[13] Aryal P, Molloy JA, Rivard MJ. A modern monte carlo investigation of the TG-43 dosimetry parameters for an 125I seed already having AAPM consensus data. *Med Phys*. 2014;41(2):021702.

[14] Solberg TD, DeMarco JJ, Hugo G, Wallace RE. Dosimetric parameters of three new solid core I-125 brachytherapy sources. *J Appl Clin Med Phys*. 2002;3(2):119-134.

[15] Eye Physics Ver. 6 User Guide. Plaque Simulator. https://www.eyephysics.com/PS/Index.html. Accessed May, 2019.

[16] Rivard MJ, Chiu-Tsao ST, Finger PT, *et al*. Comparison of dose calculation methods for brachytherapy of intraocular tumors. *Med Phys*. 2011;38(1):306-316.

[17] Morrison H, Menon G, Larocque MP, *et al.* Initial evaluation of advanced collapsed cone engine dose calculations in water medium for I-125 seeds and COMS eye plaques. *Med Phys*. 2018;45(3):1276-1286.

[18] Krintz A, Hanson WF, Ibbott GS, Followill DS. Verification of plaque simulator dose distributions using radiochromic film [abstract]. *Med Phys*. 2002;29(6):1220-1221.

[19] Acar H, Chiu-Tsao ST, Ozbay I, Kemikler G, Tuncer S. Evaluation of material heterogeneity dosimetric effects using radiochromic film for COMS eye plaques loaded with 125I seeds (model I25.S16). *Med Phys*. 2013;40(1):011708.

[20] Moler CB. *Numerical computing with MATLAB.* Philadelphia: SIAM; 2004.

Chapter 4 Seed strength optimization to improve critical structure sparing

4.1 Introduction

During ocular plaque brachytherapy, it is possible that the nearby critical structures, such as the optic nerve, retina, and lens, may receive high radiation doses. This can lead to significant radiation side effects such as decreased visual acuity, retinopathy, and cataract formation [1], which can negatively affect the quality of life of patients following brachytherapy. Therefore, extra effort must be used to reduce doses to critical structures along with the aim of achieving desired tumor coverage. It has been shown in Chapter 3 that the SA algorithm is able to solve simple problems in ocular brachytherapy, suggesting its potential for use in more complicated problems. In this chapter, the approach taken for solving the problem of reducing doses to critical structures, while achieving the necessary tumor coverage, using differential seed strengths and position in the plaque is presented. In addition, the algorithm was further developed to handle other features including plaque shifts and elliptical tumor base shapes. Lastly, to verify the practicability of the final algorithm, its application to various clinical cases was investigated.

4.2 Methods and Materials

4.2.1 Optimization of differential seed strengths to improve sparing of critical structures with tumor coverage

The objective of this part was to improve dosimetry by reducing dose to the critical structures of the eye while delivering the prescription dose (at minimum) to the planning target volume (PTV; including the gross tumor volume (GTV) + 2 mm margin), using the SA algorithm to optimize for differential seed strengths (S_{Ks}) and positions. The first aim was to deliver at least 70 Gy to both the tumor apex and the entire PTV base. While ensuring this is achieved, the next aim was to reduce dose to critical structures. The developed algorithm is shown in Figure 4.1 (the details of the red boxes, where the concept of heat re-injection is used, will be discussed later).

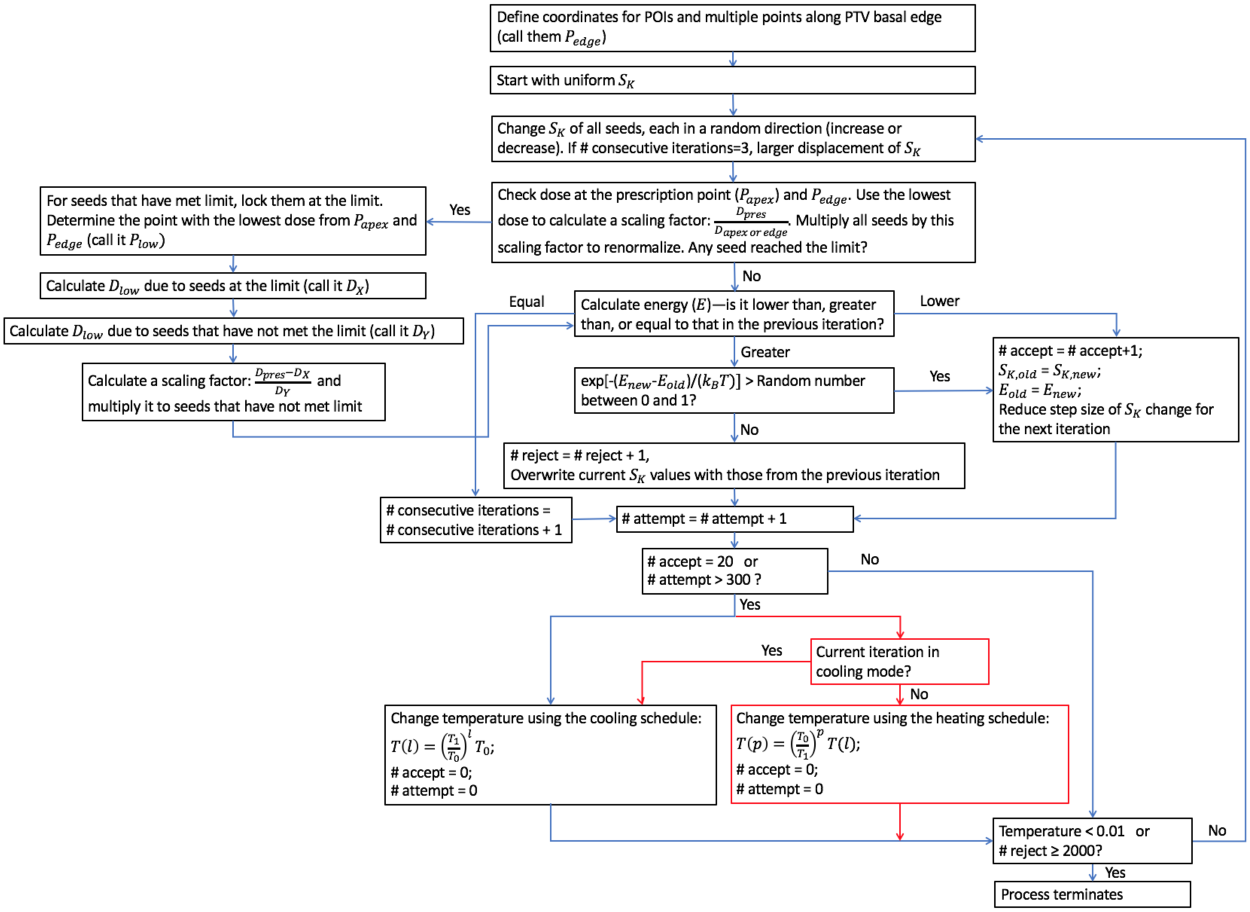

Figure 4.1 SA algorithm (black boxes) applied to solve for the problem of reducing doses to critical structures of the eye while achieving the desired target coverage. Additional steps for re-injection of heat are indicated by the red boxes and arrows.

Initially, the points of interest (POIs; each representing a critical structure) just outside the PTV, and points along the basal edge of PTV (P_{edge} at every 15 degrees along the edge; used to renormalize dose to one of these points later) are defined. Then a suitable plaque size is selected to adequately cover the PTV. Starting with uniform S_{Ks} (obtained in Test 1: dose optimization using uniform strengths (Chapter 3); these initial S_{Ks} for this algorithm, however, do not necessarily need to be obtained by the algorithm from Test 1 but need to be some equal numbers) new differential S_{Ks} are randomly generated by either increasing or decreasing the old S_{Ks}. By checking dose at the apex and P_{edge}, dose is renormalized to the point with the lowest dose (apex or one of P_{edge}) to ensure that the apex and the base points receive 70 Gy at minimum; a scaling factor $\frac{D_{pres}}{D_{apex\ or\ edge}}$ is multiplied to all seeds to scale the strengths. As done in Test 2, if any seed exceeded the commercial strength limit after renormalization, those seeds were set to the limit, their strengths locked at this limit, and the excess strength redistributed to the seeds that have not met the limit. The point with the lowest dose is determined either from P_{apex} and P_{edge}, which is called P_{low} (dose to P_{low} is called D_{low}). D_{low} due to seeds at the limit (D_X) as well as D_{low} due to seeds that have not reached the limit (D_Y) are computed to calculate a scaling factor, $\frac{D_{pres}-D_X}{D_Y}$. This scaling factor is then applied to the seeds that have not reached the limit. Next, the resulting energy is calculated; if it is lower than that in the previous iteration, the current strength configuration is accepted and the step size of strength change is reduced for the next iteration. If the energy is greater than the previous one, the probability of $exp\left(-\frac{\Delta E}{k_B T}\right)$ is calculated and the solution accepted if it is larger than a random number between 0 and 1, or rejected otherwise (see Chapter 3). If the energy is equal to the previous energy, the number of consecutive rejections is increased by one; if the number of consecutive rejections reaches 3, the displacement of S_{Ks} is increased by 10% of the initial S_K to provide a bigger jump. Then, the number of attempts is increased by one. If the number of acceptances equals 20 or the number of attempts is greater than 300, the temperature is changed either by the cooling schedule or the heating schedule (re-injection of heat to the system) depending on whether the current iteration is in the cooling mode or heating mode. Finally, if the temperature is less than the minimum temperature of 0.01 or the number of rejections is $\geq$ 2000, at which point the system is considered frozen, the annealing process terminates or else, the process iterates until these stopping criteria are met. More details of the algorithm are discussed below.

Introduction of POIs

POIs were introduced in the model to represent the critical structures of the eye. Inclusion of the critical structures of the eye in the optimization process is essential as it allows the reduction of dose to those structures. Initially, a single POI was introduced. Subsequently, a second POI was added in the optimization routine to characterize more complex cases for optimization. Two POIs of significant clinical interest are the optic disc and fovea, therefore the geometry of the two POIs was chosen to represent these two structures. The location of each POI was defined by using the predicted distance between the structures, typically 4 mm between the optic disc and fovea (refer to Figure 1.1 for the eye's anatomy) [2].

Random displacement generation

As in Test 1 (Chapter 3), the random transition of S_K at each step was chosen to be a decreasing number multiplied by a normally distributed random number (with mean 0 and standard deviation 1). For this problem, this decreasing number was set to exponentially decrease in each iteration:

$$step\ size(n) = C^n, \qquad \text{(Eq. 4.1)}$$

where n is some small number (e.g. n = 0.005, 0.01, …, 20) that increases with the iteration number k, and C is a constant between 0 and 1 that defines the steepness of the exponential curve. The value of C was empirically chosen to be 0.5 - 0.9. This range was chosen following initial investigations where it was found that (i) if C < 0.5, the step size deceases too quickly as k increases and becomes negligibly small towards the end of the search, and (ii) if C > 0.9, the step size decreases too slowly or would be almost constant as k increases.

Objective function

For the case of a single POI, the objective function was simply defined to be the dose to the POI:

$$E = D_{POI} \qquad \text{(Eq. 4.2)}$$

This equation means that the solution is deemed to be an improvement if the dose to the POI decreases. For the case of two POIs, the objective function was defined to incorporate the optimization objective (amount of dose that the optimizer tries to reduce to) and weighting factor for each critical structure:

$$E = \begin{cases} w_1 \cdot \left(D_{POI,1} - D_{obj,1}\right) + w_2 \cdot \left(D_{POI,2} - D_{obj,2}\right), & if\ D_{POI,1} > D_{obj,1}\ and\ D_{POI,2} > D_{obj,2} \\ w_1 \cdot \left(D_{POI,1} - D_{obj,1}\right), & if\ D_{POI,1} > D_{obj,1}\ and\ D_{POI,2} < D_{obj,2} \\ w_2 \cdot \left(D_{POI,2} - D_{obj,2}\right), & if\ D_{POI,1} < D_{obj,1}\ and\ D_{POI,2} > D_{obj,2} \\ 0, & if\ D_{POI,1} < D_{obj,1}\ and\ D_{POI,2} < D_{obj,2}, \end{cases}$$

(Eq. 4.3)

where w_1 and w_2 are the importance weighting factors, $D_{POI,1}$ and $D_{POI,2}$ are the calculated doses, and $D_{obj,1}$ and $D_{obj,2}$ are the optimization objectives for POIs 1 and 2, respectively. This means that energy is decreased when dose to a POI is reduced down to the optimization objective, but not further i.e. for reductions lower than the objective. The objective and weight of each POI can be adjusted by the user if he/she is not satisfied with the produced dose distribution.

For an arbitrary number of POIs (j), this equation can be expanded as:

$$E = \sum_{i=1}^{j} w_i \cdot (D_{POI,i} - D_{obj,i}). \tag{Eq. 4.4}$$

When $D_{POI,i} < D_{obj,i}$, the term $w_i \cdot (D_{POI,i} - D_{obj,i})$ in the above equation is dropped. When all optimization objectives are achieved, E becomes 0. With this function, the optimizer works harder to reduce doses to those POIs: (i) with lower optimization objectives, (ii) situated closer to the seeds receiving higher doses, and (iii) with larger weighting factors. This approach of difference of dose to a structure and its acceptable dose as the objective function has been previously investigated in numerous studies and found to be suitable [3,4]. This is one example of an objective function; there are also other approaches for defining an objective function [5,6]. Although this study only included cases of one and two POIs, the developed algorithm can optimize for an arbitrary number of POIs using Eq. 4.4, which involves a simple modification to the developed Matlab code.

Re-injection of heat

Although the SA algorithm provides a good chance of finding a global minimum by incorporating the probability of accepting worse solutions in the search and thereby allowing escape from local minima, there is no guarantee that it will find a global minimum. As the search starts with a high temperature, there is a greater chance of accepting a worse solution that will allow the search to move out of local minima. However, as the search continues and temperature decreases, it results in a lower chance of uphill moves. This may not lead to an optimal solution if some local minima are encountered towards the end of the search when the temperature is relatively low. There have been attempts to overcome this shortcoming of the conventional SA algorithm by controlling and changing temperature adaptively instead of continuously decreasing it and was shown that this approach is able to find better solutions compared to the conventional SA method [7,8,9]. In the experiment by Dowsland, two functions were considered to control the temperature; the first is a cooling function that reduces the temperature, whereas the second is a heating function that gradually increases the temperature when needed [7]. This approach of re-injecting heat into the system showed an improvement in the results compared to those obtained using only the cooling schedule that lowers the temperature by a constant factor [7].

To test the effect of re-injecting heat into the system, optimization for a single POI was performed both with and without re-injection of heat. The process without heat re-injection is similar to that shown in Figure 4.1, except that the red boxes would be excluded. The objective for performing this test with and without heat re-injection was to select the method that gave better results, and in the case that both gave similar results, optimization with heat re-injection would be used to make the optimization routine likely more robust. Heat was re-injected for 50 iterations after every 500 iterations of cooling (i.e. if the iteration number blocks for cooling mode were 1-500, 551-1050, and so on, the heating mode would belong to iterations 501-550, 1051-1100, and so on). During a heating schedule where heat was re-injected, the cooling schedule was reversed:

$$T(p) = \left(\frac{T_0}{T_1}\right)^p T(l) \qquad \text{(Eq. 4.4)}$$

where p is the step count for temperature increase, always starting as 1 when iteration enters a new heating mode. $T(l)$ indicates the temperature used in the last iteration in the previous cooling mode. This schedule, by using the inverse of the constant factor $\frac{T_1}{T_0}$ $(0 < \frac{T_1}{T_0} < 1)$ used for the cooling schedule, provides the direct reverse of the cooling schedule.

4.2.2 Additional investigation: plaque shift, elliptical tumor base and application to clinical cases

To expand the capabilities of the optimization routine, more features including allowing the user to place the plaque off-centred from the tumor base ("plaque shift") and consideration of elliptical tumor base shapes were implemented and investigated. This enhanced SA algorithm was applied to anonymized clinical cases to verify the practicality of implementation into clinical scenarios, and possibility of improving clinical care.

4.2.2.1 Plaque shift and elliptical tumor base

Plaque shift

A plaque shift with respect to the tumor may be necessary when there are anatomical restrictions in placing the plaque during surgery (such as optic nerve), avoiding critical structures, or improving ease of placement. Typically for ease with performing the shift during insertion, the plaque is moved in its anterior-posterior direction with respect to the tumor along the eye surface by a distance defined by the user. In the Matlab code, this was done by rotating the seed coordinates about the shifted y-axis (of the seed coordinate system specified in TG-129 [10]) that passes through the center of the eye so that the seeds would shift along the x-axis, which is the anterior-posterior direction (Figure 4.2).

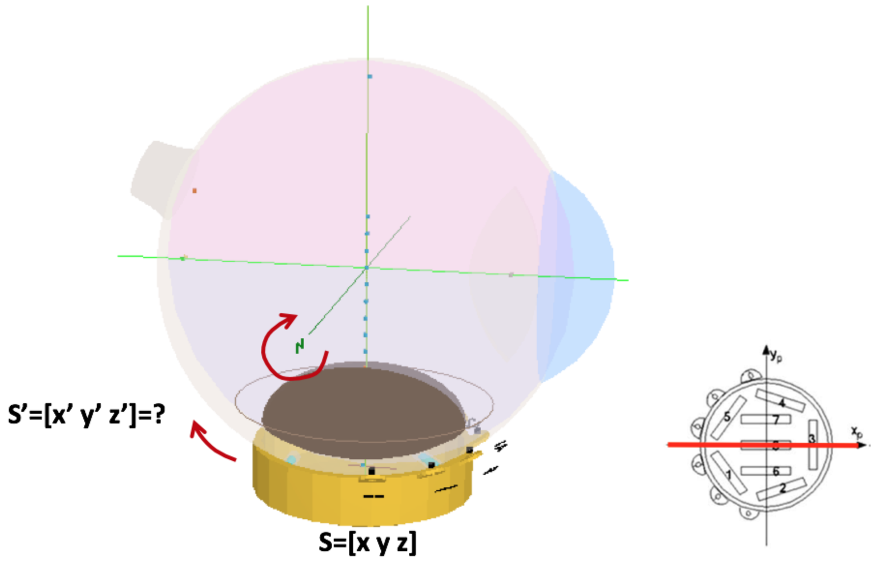

Figure 4.2 (Left) An example of a rotation of the original seed coordinates (**S**=[**x y z**]) about the axis passing through the eye's center to obtain the new shifted coordinates (**S′**=[**x′ y′ z′**]) (image reproduced from Eye Physics Ver. 6 User Guide. [11]). (Right) The anterior-posterior direction of the plaque is shown by the red line (image reproduced from Chiu-Tsao, et al. with permission from Medical Physics [10]).

Elliptical tumor base

Up to this point, tumors with a circular base were considered in all the problems. However, in general, basal tumor shapes are not perfectly circular and hence a tumor with an elliptical base was considered to approximate a variety of actual tumor base shapes. Therefore, a feature to construct and define basal points in an elliptical base by inputting basal dimensions was added to the SA optimization routine. First, points that make up the lower hemisphere of a sphere were defined using the equations of a sphere. The two inputs were a and b, the semi-major and semi-minor axes of the GTV base, respectively. A 2 mm margin was added to each number (say, a_{PTV} and b_{PTV}) to generate the PTV basal dimensions. Then, the radial distance of the ellipse was calculated using the equation of an ellipse in polar coordinates:

$$r_{ellip} = \frac{a_{PTV} b_{PTV}}{\sqrt{a_{PTV}^2 \sin^2 \theta + b_{PTV}^2 \cos^2 \theta}}, \qquad \text{(Eq. 4.5)}$$

where θ is the angle from the major axis [12]. For each z value of points on the sphere (collection of circles with different radii), the radius of the circle was calculated using the equation of a circle in Cartesian coordinates:

$$r_{sphere} = \sqrt{x^2 + y^2}, \qquad \text{(Eq. 4.6)}$$

where x and y are the position coordinates of a point on the circle [12]. r_{ellip} and r_{sphere} having equal values were matched and z for those matched points on the sphere were recorded (z_r). Lastly, the points on the sphere with $z > z_r$ (i.e., residual points sitting outside the elliptical base) were removed. The remaining points then make up an elliptical PTV base with the curvature of a sphere. These basal points were used as dose calculation points for full coverage of the PTV base. This process of constructing a PTV with elliptical base is shown in Figure 4.3.

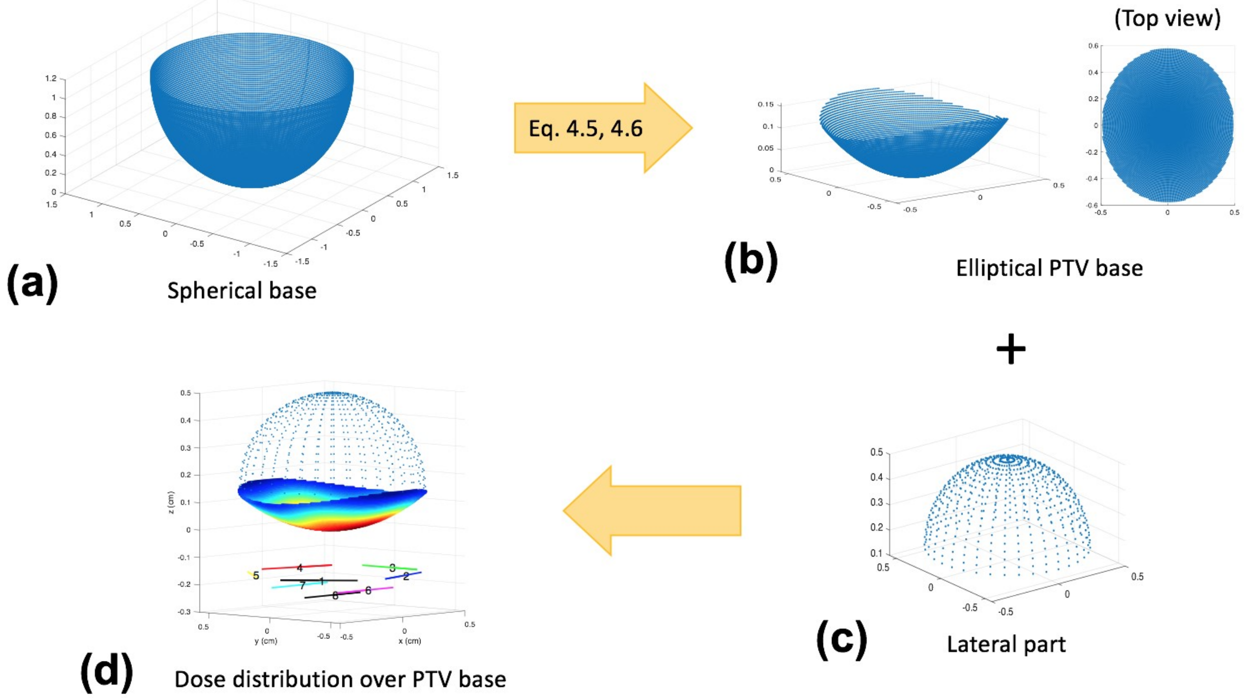

Figure 4.3 The process of constructing a PTV with elliptical base. (a) Points are defined to make up a lower hemisphere. (b) Using Eq. 4.5 and 4.6, an elliptical PTV base is constructed (3D structure is on the left and its top view is on the right). (c) The lateral part of the PTV is added. (d) The entire PTV is constructed with dose distribution shown over the base.

4.2.2.2 Application to clinical cases

The objective of developing this SA algorithm was eventually for use in clinical planning and therefore it is necessary to verify the practicality of implementation in clinical scenarios. In this section, the algorithm was applied to 10 anonymized clinical scenarios of previously treated patients (ethics approved). These cases were selected from a retrospective database of choroidal melanoma patients treated at the Cross Cancer Institute (CCI) in between 2011-2018. Patients were chosen if the PTV was within about 1 to 6 mm of the fovea and optic disc; if the critical structures were too proximal or too distal from the PTV, the case would not be ideal for conformal optimization. PTVs located between 1 and 6 mm from a critical structure offer the most potential to have their dose reduced below commonly accepted thresholds for complications. In Plaque Simulator, pre-existing retinal diagrams including the fundus photos of patients were opened. On each diagram, the GTV base, fovea, and optic disc had been previously located by an ophthalmologist specializing in ocular oncology. The tumor (GTV) basal dimensions and height were measured and a 2 mm margin was added to this base to generate the PTV. For the fovea and optic disc, distance from the GTV edge and also the distance between the two structures were measured. Using these distances, their angular locations relative to the GTV base were also calculated. This information was then input into the SA algorithm to mimic each clinical case. The measurements of the GTV dimensions, plaque size and shift, and locations of the critical structures for each case are shown in Table 4.1. The retinal diagrams showing the tumor, plaque, and critical structures for Cases 5 and 10 are shown in Figure 4.4. These two cases were chosen as they have different tumor and plaque sizes, with shifted and non-shifted plaques.

Table 4.1 Tumor dimensions, plaque size and shift, and locations of the critical structures of the 10 anonymized clinical cases.

Clinical case	GTV basal dimensions (mm)	Tumor height (mm)	Plaque size (mm)	Plaque shift (mm)	Distance from PTV edge (mm)		Distance between fovea and optic disc (mm)
					Fovea (POI 1)	Optic disc (POI 2)	
1	9.9 x 10.3	4.7	14	0	4.7	5.7	3.6
2	9.9 x 10.4	4.4	16	0	5.2	1.6	3.5
3	12 x 8	5.0	16	-0.7	3.6	1.2	4.2
4	11 x 10	6.0	16	0.0	2.0	5.5	4.1
5	11 x 10	6.0	18	-2.0	2.0	5.5	4.1
6	11 x 8	4.5	18	-0.8	3.7	2.7	4.0
7	13 x 12	5.3	18	-0.4	1.9	1.8	3.6
8	16 x 16	8.9	18	0.0	3.8	3.1	4.0
9	16 x 16	12.1	20	0.5	3.6	6.1	4.3
10	16 x 19	9.7	22	0.0	2.5	4.8	4.4

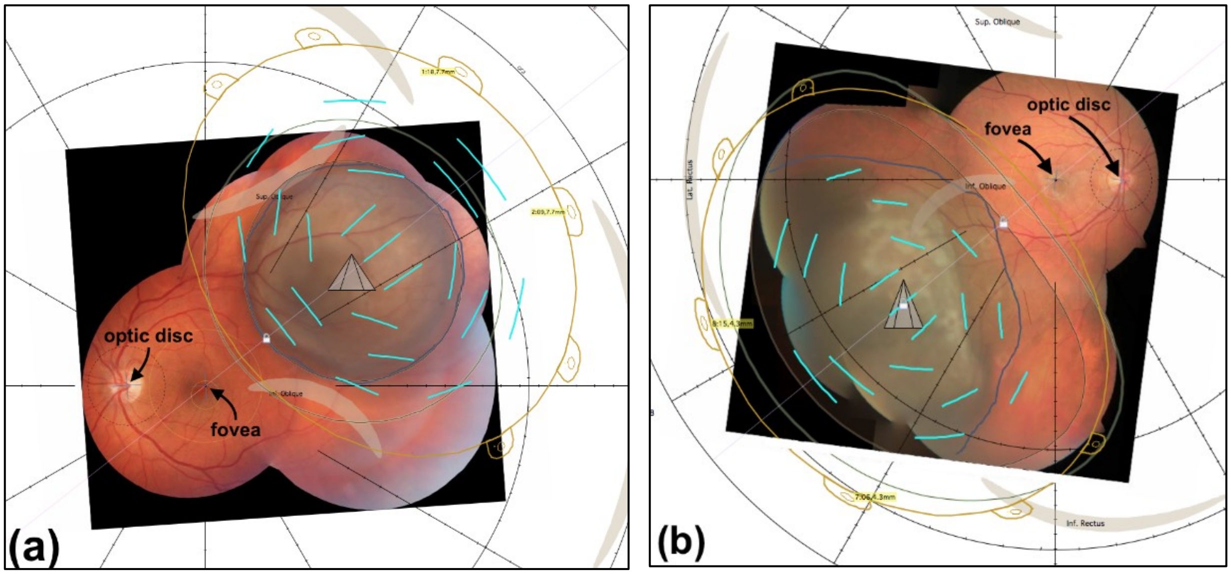

Figure 4.4 The retinal diagram from Plaque Simulator showing the fundus images for clinical cases (a) 5 and (b) 10: GTV (blue shaded region), PTV (grey line, 2mm margin added to GTV), plaque edge (yellow line), radioactive seeds (cyan lines), fovea, and optic disc.

With the input information, the algorithm was executed to find the differential strength for each seed that minimized dose to the critical structures while achieving the desired tumor coverage. These seed strengths were then manually input into Plaque Simulator to compare dose to each critical structure and also to the apex. When comparing doses, the shell collimation (attenuation of primary radiation emitted from a source by the plaque's outer shell) correction was not used in both Plaque Simulator and the SA algorithm. The presence of the plaque results in significant collimation and the dose starts to decrease in the penumbral regions near the lip (occurs outside the plaque diameter) relative to the dose for the same configurations of seeds in water [13]. Since the critical structures sit outside the plaque edge, they could be affected by the collimating effect of the lip and thus the shell collimation function in Plaque Simulator was turned off to maintain the same conditions in the two calculations.

4.3 Results and Discussion

4.3.1 Optimization of differential seed strengths to improve sparing of critical structures with tumor coverage

4.3.1.1 Optimization for single POI with and without re-injection of heat

The developed algorithm was run to optimize for a POI placed 1 mm away from the PTV edge. The average percent change (from three runs) in dose to the POI by using uniform seed strengths (i.e. equal S_{Ks} for all seeds that deliver the prescription dose to the apex without any POIs introduced in the optimization) and differential seed strengths without and with heat re-injection, as well as the average execution time for optimization are shown in Table 4.2. The resultant basal dose distributions for a 5 mm tall tumor with a 12 mm PTV diameter treated with a 12 mm plaque without and with heat re-injection are shown in Figure 4.5a and b, respectively. The dose profile along the PTV base at x=0 (along the y-axis) for each case is shown in Figure 4.5c. Also, the resultant seed strength distributions after optimization without and with using heat re-injection for a 12 mm plaque for various tumor heights is shown in Figure 4.6.

Table 4.2 Percent change in dose to POI from using uniform ($D(S_{k,uni})$) seed strengths to differential ($D(S_{k,diff})$) seed strengths with and without using re-injection of heat including the execution time for calculation.

Plaque size (mm)	Tumor height (mm)	$D(S_{k,uni})$ (Gy)	Without heat re-injection			With heat re-injection		
			$D(S_{k,diff})$ (Gy)	% Change	Execution time (s)	$D(S_{k,diff})$ (Gy)	% Change	Execution time (s)
12	3.5	52.8	49.4±0.1	-6.5±0.2	204.5±40.7	49.4±0.1	-6.6±0.1	192.7±68.1
	5	72.9	51.0±0.1	-30.0±0.2	139.3±30.2	51.1±0.1	-29.9±0.2	165.7±40.8
	8	139.8	99.3±0.2	-29.0±0.1	261.6±4.2	99.1±0.0	-29.1±0.0	255.1±10.2
16	3.5	52.6	51.0±0.2	-3.1±0.5	307.1±28.9	51.3±0.0	-2.5±0.0	295.5±21.8
	5	52.6	51.3±0.1	-2.4±0.2	269.0±4.7	51.3±0.1	-2.4±0.2	275.9±1.9
	8	92.2	55.7±0.4	-39.6±0.4	302.1±13.0	55.6±0.1	-39.7±0.1	274.8±57.4
22	3.5	57.6	57.4±0.1	-0.3±0.4	455.3±28.5	57.6±0.2	-0.1±0.2	480.1±33.6
	5	57.6	57.6±0.2	-0.1±0.4	416.8±15.6	57.6±0.2	-0.1±0.3	379.6±24.1
	8	57.6	57.6±0.1	-0.1±0.2	429.6±48.3	57.4±0.3	-0.4±0.5	428.9±7.0

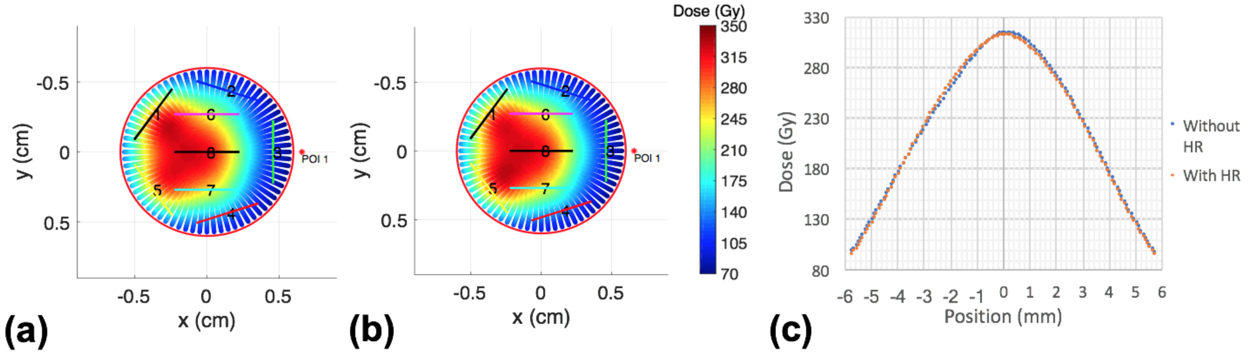

Figure 4.5 The basal dose distributions for a 5 mm tall tumor having 12 mm PTV basal diameter and treated with a 12 mm plaque (a) without and (b) with heat re-injection (HR) in the SA algorithm. The dose distribution is shown over the PTV base, the numbered lines (1-8) represent the seeds, the red line represents the plaque edge, and the star represents the point of interest (POI 1). Dose profiles along the PTV base at x=0 for (a) and (b) are shown in (c).

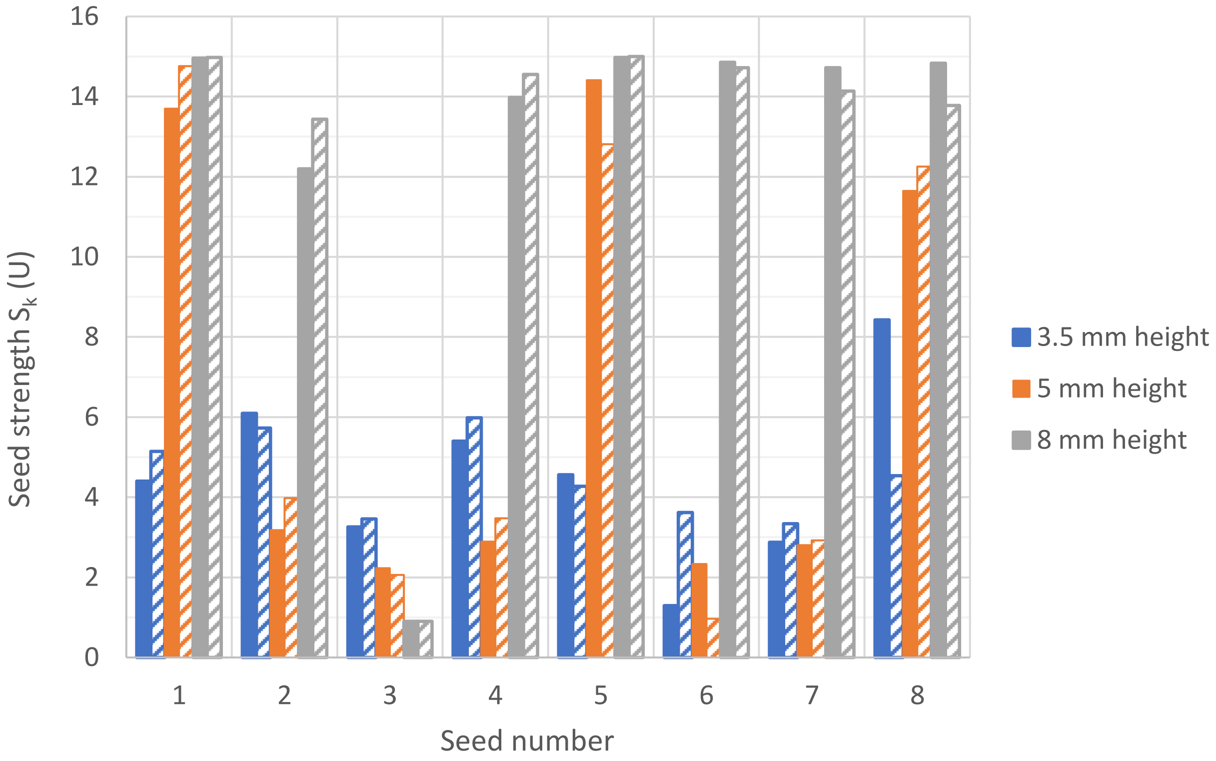

Figure 4.6 The resultant seed strength distributions after optimization for single POI without (hatched bars) and with (solid filled bars) heat re-injection for a 12 mm plaque for various tumor heights.

From Table 4.2, it can be confirmed that the algorithm worked properly by being able to reduce dose to the POI in a reasonable amount of time. For the 16 mm plaque, the dose reduction for the

8 mm tall tumor was quite high (about 40% for both methods). This is mainly because dose to the POI using uniform loading is very large (92.2 Gy). For uniform loading, the 70 Gy isodose line for this tumor height is perhaps pushed further beyond the POI to reach 70 Gy at the apex and thus a larger reduction can be achieved with differential loading by pulling in the 70 Gy line towards the PTV. However, for lower heights with the same plaque, the 70 Gy line is mostly just touching the PTV edge (and went beyond the apex), such that for covering the whole PTV edge with 70 Gy, further POI dose reduction is not possible with differential loading. Also, there was minimal POI dose reduction for the 22 mm plaque; since all tumor heights are relatively small compared to the large PTV basal diameter, the 70 Gy line went beyond the apex and just touched the PTV edge. Hence, dose to the POI that is very close to the tumor could not be reduced with differential loading. Moreover, it can be seen from Table 4.2 that, for both methods of without and with heat re-injection, % dose reduction and execution time for all scenarios are similar. The resultant dose distribution and seed strength distributions for each method in Figures 4.5 and 4.6 are also visually very similar, suggesting minimal effect of re-injecting heat in the system. Therefore, optimization with re-injection of heat was used for the rest of this work to keep the optimization routine more robust. In Figures 4.5 and 4.6, the seeds proximal to the POI (e.g. seed 3) have generally lower strengths to improve sparing of the POI. These lower strengths were compensated by other distal seeds (e.g. seeds 1 and 5) having higher strengths to deliver the minimum 70 Gy to the apex and the basal edge.

4.3.1.2 Optimization for two POIs with re-injection of heat

Figure 4.7 shows the case with the 2 POIs. POI 1 was introduced to represent the optic nerve and POI 2 to represent the fovea. The POIs were placed at a distance of 4 mm apart from each other, and at 1 mm from the PTV margin. The optimization objectives of POIs 1 and 2 were set to 60 Gy and 50 Gy, respectively, which are the tolerance doses for the optic nerve and fovea [14,15]. Equal importance weighting factors of 1 were used for both POIs. The average percent change (from three runs) in dose to POIs 1 and 2 by using differential seed strengths compared to using uniform seeds strengths, dose to apex (D_{apex}), basal maximum and minimum doses (D_{max} and D_{min}) are shown in Table 4.3. Also, the resulting basal dose distribution for a 5 mm tall tumor with 12 mm PTV basal diameter treated with a 12 mm plaque, an 8 mm tall tumor with 16 mm PTV basal diameter treated with a 16 mm plaque, and a 3.5 mm tall tumor with 22 mm PTV basal diameter treated with a 22 mm plaque are shown in Figure 4.7. In this figure, POIs 1 and 2 appear to be closer to the basal edge for larger tumor base; this is because for larger tumor base, POIs are located higher from the bottom of the base due to the curvature of the spherical surface. Furthermore, the resultant seed strength distributions after optimization for the two POIs with heat re-injection for a 12 mm plaque is shown in Figure 4.8.

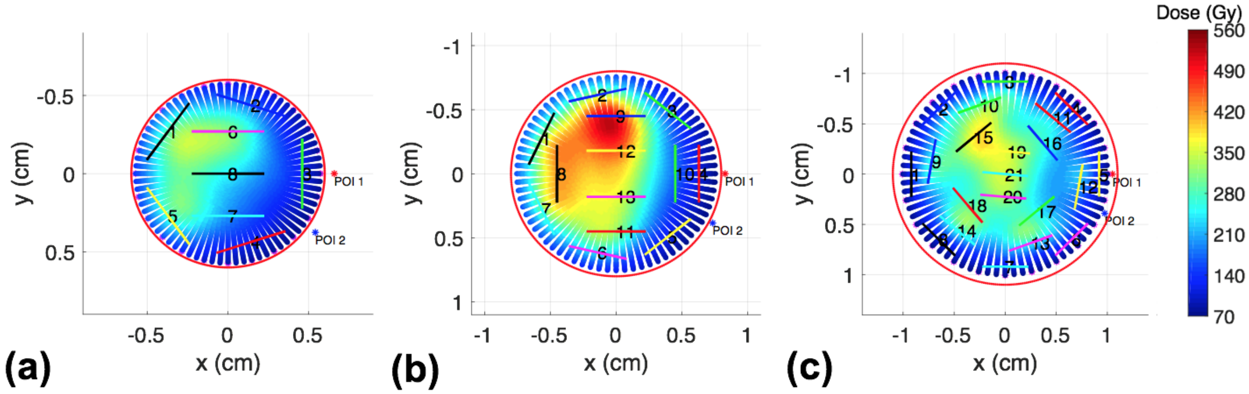

Figure 4.7 Basal dose distribution after optimization for two POIs (4 mm apart) for (a) 5 mm tall tumor having a 12 mm PTV basal diameter treated with a 12 mm plaque, (b) 8 mm tall tumor having a 16 mm PTV basal diameter treated with a 16 mm plaque, and (c) 3.5 mm tall tumor having a 22 mm PTV basal diameter treated with a 22 mm plaque.

Table 4.3 Percent change in dose to POIs 1 and 2 (placed 4 mm apart) from using uniform seed strengths ($D(S_{k,uni})$) to differential seed strengths ($D(S_{k,diff})$), D_{apex}, basal D_{max}, and basal D_{min}. Standard deviations of 0.0 represent values < 0.05.

Plaque size (mm)	Tumor height (mm)	POI 1 (optic disc)			POI 2 (fovea)			Using $S_{k,diff}$		
		$D(S_{k,uni})$ (Gy)	$D(S_{k,diff})$ (Gy)	% Change	$D(S_{k,uni})$ (Gy)	$D(S_{k,diff})$ (Gy)	% Change	D_{apex} (Gy)	D_{max} (Gy)	D_{min} (Gy)
12	3.5	52.8	53.0±1.0	+0.3±1.9	53.3	50.8 ±0.2	-4.6±0.3	73.1 ±4.2	223.5 ±29.4	69.2 ±0.1
	5	72.9	55.4±0.3	-24.0±0.4	73.5	52.7 ±0.1	-28.4 ±0.1	70.1 ±0.1	340.8 ±25.2	69.4 ±0.1
	8	139.8	99.0±0.0	-29.2±0.0	140.8	114.3 ±0.0	-18.8 ±0.0	70.0 ±0.0	615.3 ±0.1	131.0 ±0.0
16	3.5	52.6	51.9±0.7	-1.3±1.4	53.6	53.3 ±0.2	-0.5±0.4	95.6 ±7.2	222.6 ±24.1	69.9 ±0.1
	5	52.6	52.1±0.3	-1.1±0.5	53.6	53.4 ±0.1	-0.3±0.1	70.8 ±0.9	240.6 ±18.6	69.9 ±0.1
	8	92.2	57.8±1.4	-37.3±1.6	93.8	56.6 ±0.2	-39.6 ±0.2	70.1 ±0.1	517.2 ±23.1	69.7 ±0.1
22	3.5	57.6	58.0±0.1	+0.7±0.2	57.6	57.1 ±0.2	-0.8±0.3	165.8 ±15.8	387.7 ±47.7	69.8 ±0.1
	5	57.6	58.0±0.1	+0.7±0.2	57.6	57.3 ±0.2	-0.5±0.4	130.1 ±3.4	390.6 ±40.7	69.9 ±0.0
	8	57.6	58.2±0.4	+1.0±0.6	57.6	57.3 ±0.3	-0.5±0.6	82.6 ±2.4	393.5 ±10.7	69.9 ±0.1

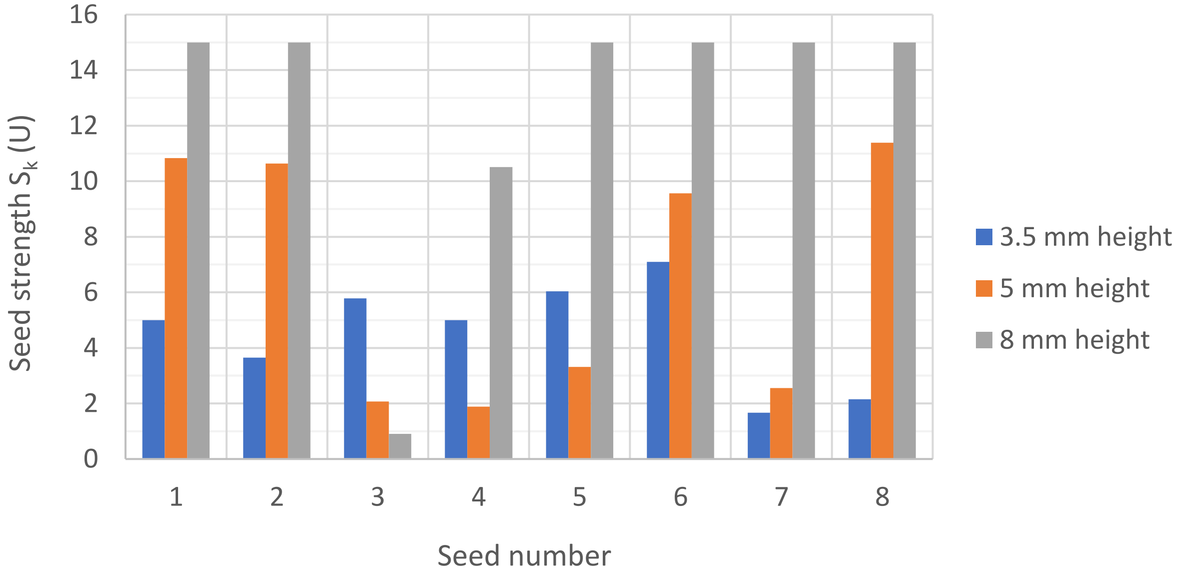

Figure 4.8 The resultant seed strength distributions after optimization for two POIs (4 mm apart) with using heat re-injection for a 12 mm plaque.

Table 4.3 shows that the algorithm was able to reduce doses to the two POIs while maintaining PTV coverage; the optimizer delivered the prescription dose of 70 Gy to the apex, as well as to the entire PTV base since D_{min} is nearly 70 Gy for all scenarios. The % reductions to the two POIs for different scenarios have a similar trend. As POI 2 has a lower objective dose of 50 Gy, it generally showed larger reductions in cases where the optimizer was able to achieve the objective dose for POI 1 (e.g. 12 mm plaque with 5 mm tumor height, and 16 mm plaque with 8 mm tumor height). These cases show that the optimizer responded to the objective values by pushing doses until reaching them and then stopping thereafter. However, if the user desires further reduction in the POI doses, it can be achieved using lower objective values. This will make the optimizer to continue reducing doses up to those objective values or up to the lowest possible doses (if the objective values are lower than achievable amounts). In addition, barely any reductions to the POIs are observed for some cases such as for the 16 mm plaque with 3.5 and 5 mm tumor heights, and 22 mm plaque (all heights). For POI 1, this is because the objective dose (60 Gy) was higher than the dose it started with (using uniform loading) such that the optimizer did not try to improve dose to POI 1. For POI 2, this is due to the same reason as discussed for the single POI case; the tumor heights are too low compared to the PTV basal diameters such that the 70 Gy isodose line went beyond the apex and just touched the PTV base. This can also be inferred by the fact that D_{apex} for these cases (e.g. 95.6 Gy for the 16 mm plaque with 3.5 mm tumor height) are higher than D_{min} (~70 Gy); after renormalizing dose to one of the points on the PTV edge (P_{edge} as defined earlier; used for renormalization if dose to that point is lower than dose to apex or other P_{edge} points), the 70 Gy line went beyond the apex while it touched the P_{edge} and therefore D_{apex} came out to be higher. For 22 mm plaque, all three tumor heights were low relative to the basal diameter and thus high D_{apex} values (> 70 Gy) are observed. For this plaque, D_{apex} is higher for lower tumor heights because the 70 Gy line (with full basal coverage) is somewhere at a height greater than 8 mm; so dose to apex decreases with height. This plaque was an extreme case where the tumor diameter is much larger than all tumor heights tested. Therefore, there was no significant change in dose to POI 2 (and likely to POI 1 also if the objective was set to a lower value) with differential loading, as well as basal coverage was only possible by allowing high doses to apex. Moreover, compared to a single POI (Table 4.2), % reductions for two POIs are generally lower because for single POI, the optimizer worked to achieve as low a dose as possible whereas for two POIs, doses were only reduced up to the objective doses. The D_{min} values for some scenarios are slightly less than 70 Gy;

this is because the points on PTV edge used for renormalization (P_{edge} as defined earlier), were defined at every 15 degrees so some dose calculation points sitting between these P_{edge} could receive a slightly lower dose than 70 Gy as they were not considered as renormalization points. Although this is a small difference from 70 Gy, improvements can be achieved by defining P_{edge} with a finer resolution (e.g. every 5 degrees), at the expense of a slightly longer execution time. Practically speaking, a dose difference of 0.5 Gy, corresponds to a physical distance of <0.05 mm, meaning the margin coverage is reduced from 2.00 mm to >1.95 mm. Given that these values will be transferred to Plaque Simulator for a final calculation, fine-tuning to this degree was not required at this stage.

Figure 4.7 shows that, as observed in Table 4.3, higher sparing of the two POIs was achieved for cases (a) and (b), but not for (c) due to the reason previously discussed. For cases (a) and (b), dose distributions are skewed toward the opposite side of the POIs to improve sparing of the POIs. Hence, for both cases, D_{max} appears in the hot region away from the POIs while D_{min} appears at the PTV edge very close to the POIs. In Figure 4.8, for the 5 mm tumor height, lower strengths for seeds 3, 4 and 7 are observed to better spare the POIs and higher strengths for the rest of the seeds; this is to compensate for the lower strengths since the seeds together need to deliver at least 70 Gy to the tumor apex and the base. A similar trend is observed for the 8 mm height, except most of the seeds are at the maximum strengths of 15 U to deliver the same 70 Gy to the apex deeper than 5 mm. For the 3.5 mm height, a more uniform distribution is observed since the apex is too close to the plaque.

To test if the developed optimization routine also works with different locations of POIs, POI 2 was moved to the opposite side of POI 1 (each POI still at 1 mm from the PTV edge). In addition, different objective doses and weightings on these POIs were tested to verify whether the optimizer responded to these different conditions. Using a 5 mm tall tumor with a 12 mm PTV basal diameter with a 12 mm plaque, optimization was done with three different scenarios: (a) equal objective dose of 60 Gy and equal weighting of 1, (b) different objective doses ($D_{obj,1} = 60$ Gy, $D_{obj,2} = 30$ Gy) and equal weighting of 1, and (c) equal objective dose of 50 Gy and different weightings ($w_1 = 0.2, w_2 = 0.8$). The resultant basal dose distribution for each case is shown in Figure 4.9.

The average percent change (from three runs) in dose to each POI from using uniform to differential seed strengths for each case is displayed in Table 4.4.

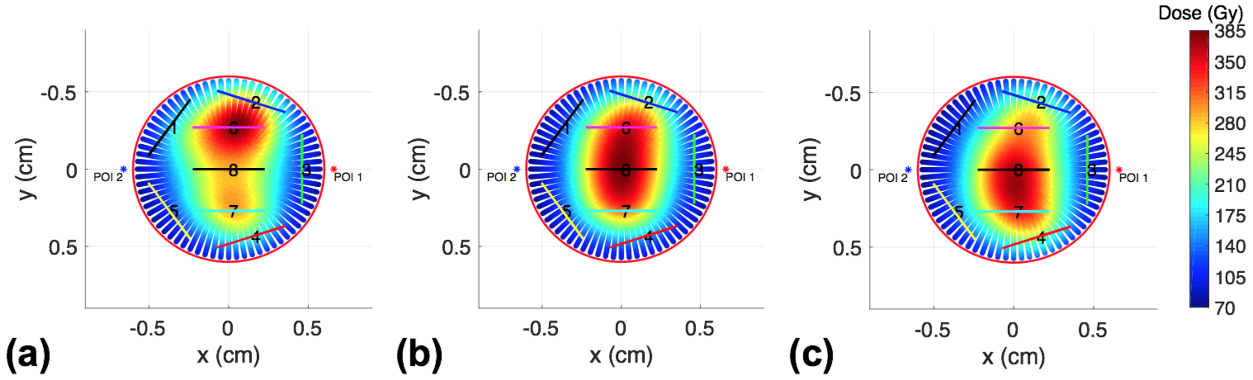

Figure 4.9 The basal dose distribution after optimization for a 5 mm tall tumor having a 12 mm PTV basal diameter treated with a 12 mm plaque and considering two POIs placed oppositely with (a) equal optimization objective doses of 60 Gy and weighting of 1, (b) different objective doses ($D_{obj,1}$=60 Gy, $D_{obj,2}$=30 Gy) and equal weighting of 1, and (c) equal objective doses of 50 Gy and different weightings ($w_1 = 0.2$, $w_2 = 0.8$).

From Figure 4.9a and Table 4.4, by using equal objectives and weightings on both POIs, the dose distribution was hotter towards the midline of the PTV base and dose reduction to each POI was fairly similar. For both POIs, the optimizer stopped reducing doses beyond the objective doses of 60 Gy from which we can confirm that it correctly responded to the objectives. In Figure 4.9b, the dose distribution was still hotter towards the midline of the base to spare both POIs. However, by putting a lower objective dose for POI 2, it was somewhat biased towards POI 1 for better sparing of POI 2; the dose reduction for POI 2 was also much higher than that for POI 1. The optimizer again stopped reducing dose further beyond the objective value for POI 1 and worked harder to improve sparing of POI 2. In Figure 4.9c, due to a higher weighting on POI 2, the dose distribution was biased towards POI 1 to better spare POI 2. This confirmed that the optimizer also responded to the weightings on the POIs. As such, the effect of objective doses and weightings are quite evident in all three scenarios; the optimizer reduced doses only up to the objective values when the objectives were achievable, and up to the lowest possible doses when the objectives were not achievable, as well as it yielded a larger reduction for POI with a higher weighting. Therefore, it was verified that the algorithm also worked properly with different locations of POIs and with different objective doses and weightings.

Table 4.4 Percent change in dose to POI 1 and POI 2 from using uniform seed strengths ($D(S_{k,uni})$) to differential seed strengths ($D(S_{k,diff})$), D_{apex}, basal D_{max}, and basal D_{min} for various combinations of objective doses and weightings on oppositely placed POIs.

$D_{obj,1}$ (Gy)	$D_{obj,2}$ (Gy)	w_1	w_2	POI 1			POI 2			Using $S_{k,diff}$		
				$D(S_{k,uni})$ (Gy)	$D(S_{k,diff})$ (Gy)	% Change	$D(S_{k,uni})$ (Gy)	$D(S_{k,diff})$ (Gy)	% Change	D_{apex} (Gy)	D_{max} (Gy)	D_{min} (Gy)
60	60	1	1	72.9	58.6±0.9	-19.7±1.2	70.8	58.6±0.7	-17.2±1.0	70.0±0.0	385.9±30.9	74.2±0.9
60	30	1	1	72.9	58.6±0.8	-19.6±1.2	70.8	52.6±0.0	-25.7±0.1	70.1±0.2	389.6±8.3	70.0±0.0
50	50	0.2	0.8	72.9	57.8±1.4	-20.7±1.9	70.8	52.7±0.2	-25.6±0.3	70.1±0.0	388.3±30.9	69.7±0.2

4.3.2 Additional investigation: plaque shift, elliptical tumor base, and application to clinical cases

4.3.2.1 Plaque shift and elliptical tumor base

Plaque shift

A 12 mm plaque was shifted by ±3 mm in the anterior (+ve) and posterior (-ve) directions (Figure 4.10) to optimize for two POIs separated by 4 mm for a 5 mm tall tumor with 12 mm PTV basal diameter. Optimization objectives to POIs 1 and 2 were set to 60 and 50 Gy, respectively, both with equal weightings of 1. The average percent change (from three runs) in dose to the POIs from using uniform seed strengths to differential seed strengths, D_{apex}, basal D_{max} and basal D_{min} are displayed in Table 4.5.

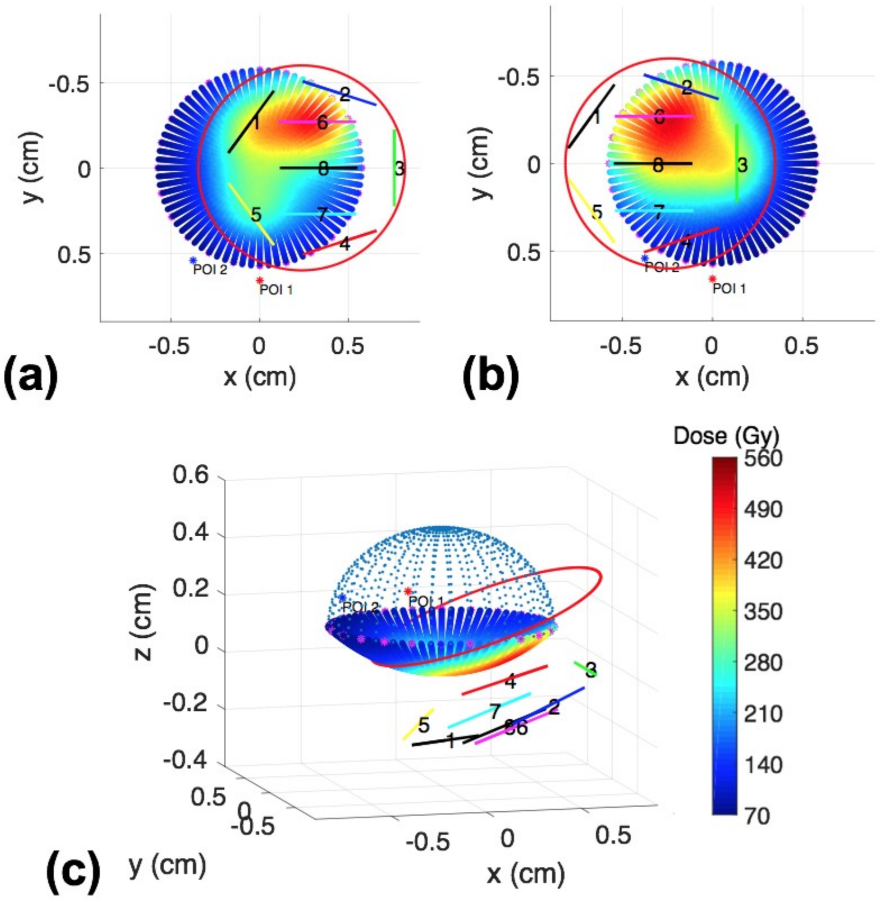

Figure 4.10 The basal dose distribution after optimization for two POIs with a 5 mm tall tumor with a 12 mm PTV basal diameter treated with a 12 mm plaque shifted by 3 mm in (a) anterior direction, and (b) posterior direction. The 3D view of (a) is shown in (c).

Table 4.5 Percent change in dose to the POIs from using uniform seed strengths ($D(S_{k,uni})$) to differential seed strengths ($D(S_{k,diff})$), D_{apex}, basal D_{max}, and basal D_{min} for a 5 mm tall tumor treated with a 12 mm plaque shifted in anterior and posterior directions.

Plaque shift (mm)	POI 1			POI 2			Using $S_{k,diff}$		
	$D(S_{k,uni})$ (Gy)	$D(S_{k,diff})$ (Gy)	% Change	$D(S_{k,uni})$ (Gy)	$D(S_{k,diff})$ (Gy)	% Change	D_{apex} (Gy)	D_{max} (Gy)	D_{min} (Gy)
3	106.4	72.2±3.3	-32.2±3.1	71.6	60.7±0.5	-15.3±0.7	92.3 ±11.5	523.1 ±45.6	69.9 ±0.0
-3	107.1	60.6±0.4	-43.5±0.3	175.9	83.4±0.9	-52.6±0.5	92.7 ±4.7	534.0 ±22.7	70.0 ±0.0

From Figure 4.10, it can be seen that, for both cases, the plaque was shifted correctly as desired along the x-axis, which is the anterior-posterior direction of the plaque. Also, it is shown in Table 4.5 that, even with a shift, the prescription dose of 70 Gy at minimum was delivered to the PTV since D_{apex} and D_{min} are greater than or equal to about 70 Gy. The basal D_{max} values are quite high (about 500 Gy) as the optimizer had to increase the S_{Ks} to deliver 70 Gy all the way at the PTV edge that is on the opposite side of the shifted plaque. The D_{apex} values (about 90 Gy) are somewhat greater than 70 Gy because dose in the hot region of the base is very high and most seeds contributing to these high doses (e.g. seeds 1, 2, and 6) may be closer to the apex than to the farthest P_{edge} and thus dose was renormalized to this P_{edge} instead of to the apex resulting in the basal D_{min} of 70 Gy and $D_{apex} > 70$ Gy. Moreover, in Figure 4.10a and b, as the distance of POI 2 from the plaque changes extensively for different shifts, dose to POI 2 with uniform loading and % reductions for POI 2 for different shifts also vary significantly compared to POI 1, which do not show as varied a change due to its placement on the mid-line (x=0) of the shifts. Also, for the case of posterior shift (Figure 4.10b), POI 2 is inside the plaque and thus higher doses (e.g. 175.9 Gy for $D(S_{k,uni})$) are observed. This was done to test the robustness in movement of the plaque and the ability of the algorithm to perform optimization in extreme scenarios.

Elliptical tumor base

With the two POIs placed at 4 mm apart (POI 1 at 1 mm from PTV edge, and POI 2 approximately at 1 mm from PTV edge), optimization was performed for a 8 x 6 mm GTV base, 5 mm tumor height, treated with a 12 mm plaque (Figure 4.11a), as well as for a 10 x 12 mm GTV base, 8 mm tumor height, treated with a 16 mm plaque (Figure 4.11b,c). For the GTV bases, the 2 mm margin was again added. As before, optimization objective doses to POIs 1 and 2 were set to 60 and 50

Gy, respectively, both with equal weightings of 1. The average percent change (from three runs) in dose to the POIs from using uniform seed strengths to differential seed strengths, D_{apex}, basal D_{max} and basal D_{min} are displayed in Table 4.6.

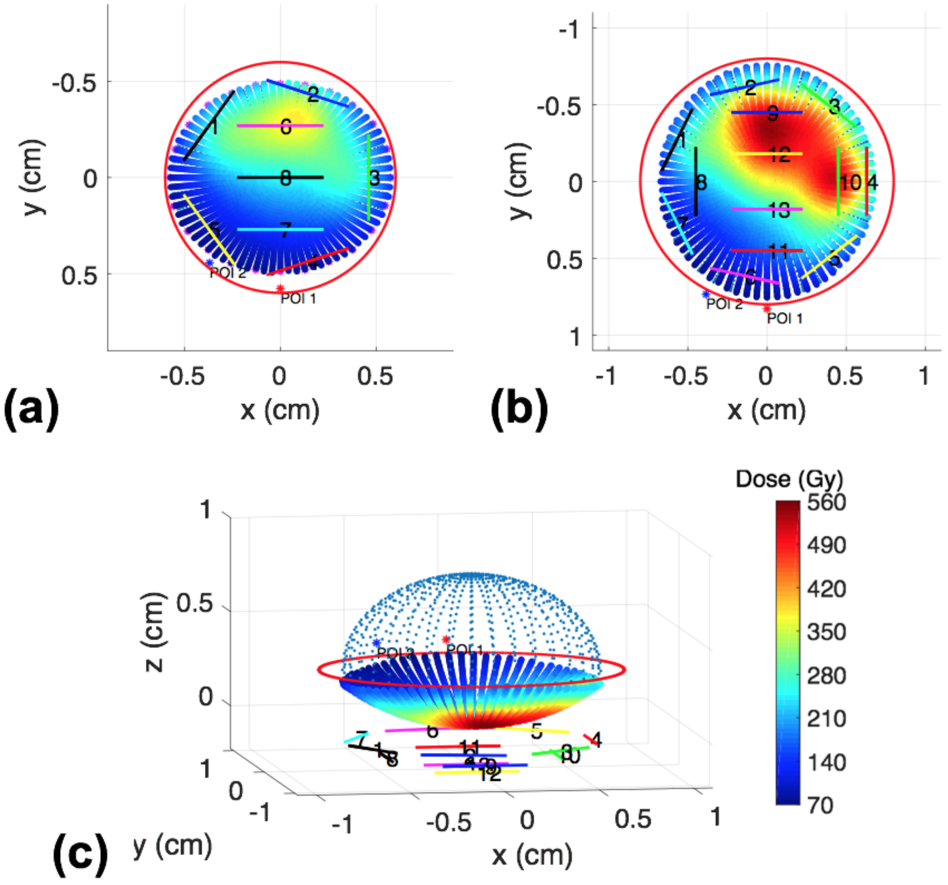

Figure 4.11 The basal dose distribution after optimization for two POIs for (a) an 8 x 6 mm GTV base, 5 mm tumor height, treated with a 12 mm plaque, and (b) a 10 x 12 mm GTV base, 8 mm tumor height, treated with a 16 mm plaque. The 3D view of (b) is shown in (c). The dose distribution is shown over the PTV base.

Table 4.6 Percent change in dose to the POIs from using uniform seed strengths ($D(S_{k,uni})$) to differential seed strengths ($D(S_{k,diff})$), D_{apex}, basal D_{max}, and basal D_{min} for elliptical tumor bases (dim indicates dimension).

Plaque size (mm)	Tumor height (mm)	GTV basal dim (mm)	POI 1			POI 2			Using $S_{k,diff}$		
			$D(S_{k,uni})$ (Gy)	$D(S_{k,diff})$ (Gy)	% Change	$D(S_{k,uni})$ (Gy)	$D(S_{k,diff})$ (Gy)	% Change	D_{apex} (Gy)	D_{max} (Gy)	D_{min} (Gy)
12	5	8x6	110.4	58.4±0.7	-47.1± 0.7	110.1	59.6±0.0	-45.9± 0.0	70.1±0.0	404.6±26.1	69.0±0.1
16	8	10x12	95.6	59.3±0.6	-38.0± 0.6	94.8	53.5±0.4	-43.6± 0.4	70.0±0.0	550.8±8.2	70.0±0.0

Figure 4.11 shows that elliptical tumor shapes were correctly generated with dose distributions shown over the PTV base. For both cases shown, the dose distributions are skewed to the opposite side of the POIs as the optimizer strengthened the seeds in that region to improve sparing of the POIs. The improvements in doses to the POIs are quite large as can be seen in Table 4.6; the dose objective for POI 1 (60 Gy) was met and also large reductions (about 45%) on POI 2 were achieved in both scenarios with differential loading. Similar to the discussion earlier, with uniform loading, the 70 Gy line reached the apex and went beyond the POIs, which explains the large doses to the POIs of about 100 Gy; differential loading pulled this 70 Gy line extensively towards the PTV edge near the POIs and thereby reduced doses to the POIs by large amounts. The prescription dose of 70 Gy was delivered to the entire PTV as both the apex and the base have received at least 70 Gy. D_{max} values are quite large as there was no maximum limit for basal doses; the optimizer mostly increased strengths to the seeds in the hot region until they were sufficient to deliver 70 Gy to the apex and to the PTV edge close to the POIs, which is the coldest region receiving D_{min}.

Plaque shift and elliptical tumor base

In this part, the tumor with elliptical basal shape was treated with a shifted plaque to verify the effects of both features. With the two POIs placed at 4 mm apart as before, a 6 x 8 mm GTV base with 5 mm tumor height was treated with a 16 mm plaque shifted by 3 mm anteriorly for one case (Figure 4.12a, b). For the other case, a 14 x 12 mm GTV base with 8 mm tumor height was treated with a 22 mm plaque shifted by 3 mm posteriorly (Figure 4.12c, d). For the GTV bases, the 2 mm margin was again added. Dose objectives for POIs 1 and 2 were set to 60 and 50 Gy, respectively, both with equal weightings of 1. The average percent change (from three runs) in dose to the POIs from using uniform seed strengths to differential seed strengths, D_{apex}, basal D_{max} and basal D_{min} are shown in Table 4.7.

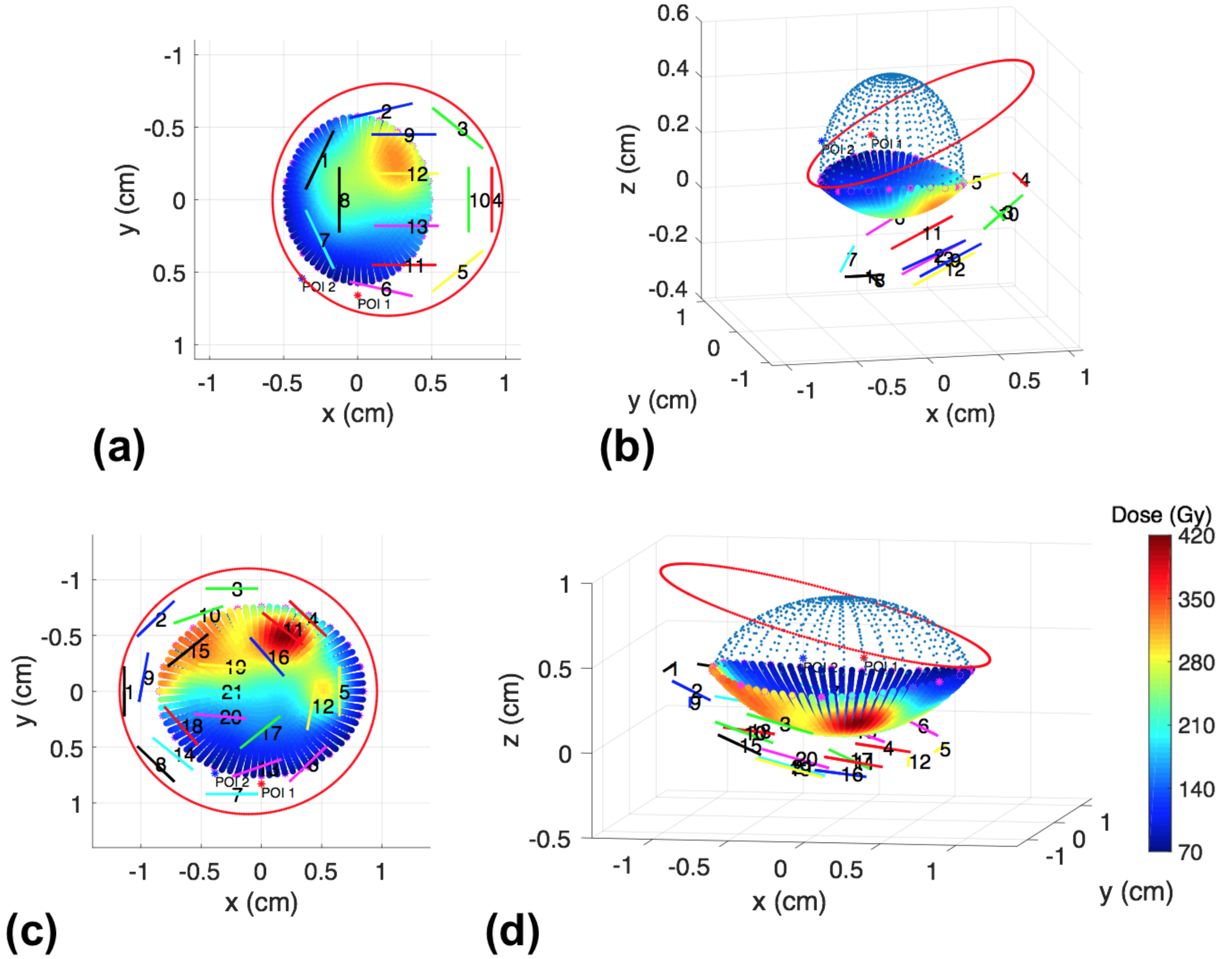

Figure 4.12 2D and 3D views of the basal dose distribution after optimization for two POIs for (a,b) a 6 x 8 mm GTV base, 5 mm tumor height, treated with a 16 mm plaque shifted by 3 mm anteriorly; and (c,d) a 14 x 12 mm GTV base, 8 mm tumor height, treated with a 22 mm plaque shifted by 3 mm posteriorly.

Figure 4.12 shows, for both scenarios, that the shifting of the plaque as well as the construction of the elliptical tumor model were performed correctly as programmed. From Table 4.7, the prescription dose of 70 Gy was delivered to the entire PTV since both the apex and the base have received 70 Gy or more. For the case with 16 mm plaque, D_{max} is >70 Gy since dose was renormalized to a P_{edge} (on the base) as it was receiving lower dose than the apex. Also, for this case, dose objectives were achieved for both POIs, which shows that the optimizer stopped reducing doses once these objectives were met. For 22 mm plaque, very high doses to both POIs are observed using uniform loading because the plaque is fully loaded and the POIs are very close to some of the seeds (sitting right below the POIs in the 2D view). Hence, this led to very large

Table 4.7 Percent change in dose to the POIs from using uniform seed strengths ($D(S_{k,uni})$) to differential seed strengths ($D(S_{k,diff})$), D_{apex}, basal D_{max}, and basal D_{min} for elliptical tumors (dim indicates dimension) treated with shifted plaques.

Plaque size (mm)	Plaque shift (mm)	Tumor height (mm)	GTV basal dim (mm)	POI 1			POI 2			Using $S_{k,diff}$		
				$D(S_{k,uni})$ (Gy)	$D(S_{k,diff})$ (Gy)	% Change	$D(S_{k,uni})$ (Gy)	$D(S_{k,diff})$ (Gy)	% Change	D_{apex} (Gy)	D_{max} (Gy)	D_{min} (Gy)
16	3	5	6x8	97.1	59.6±0.4	-38.6± 0.4	61.0	49.4±0.5	-19.0± 0.9	71.4±1.2	304.9±12.7	70.0±0.0
22	-3	8	14x12	141.1	59.5±1.2	-57.8± 0.8	174.7	68.5±3.4	-60.8± 1.9	70.0±0.0	383.0±28.0	69.7±0.9

dose reductions (about 60%) for both POIs by the optimizer lowering strengths to the seeds near the POIs and increasing strengths to the seeds farther away from the POIs. This essentially pulled in the 70 Gy line towards the PTV edge close to the POIs to deliver the D_{min} of ~70 Gy. Therefore, this test verified that optimization by the algorithm works properly with both a shifted plaque and elliptical tumor base.

4.3.2.2 Application to clinical cases

To verify the practicality of clinical implementation of seed optimization, the developed algorithm was applied to anonymized clinical cases (n = 10). The differential seed strengths obtained by the SA algorithm were then manually input into Plaque Simulator to compare dose to the critical structures and to the apex. Percent difference in dose to the fovea (POI 1), optic disc (POI 2), and apex between SA algorithm and Plaque Simulator using uniform and differential loading for each clinical case are shown in Table 4.8. In addition, to characterize the dose falloff from the PTV edge, dose (relative to dose at PTV edge) using uniform loading for Cases 4 and 10, as a function of distance from the PTV edge along the x-axis (at y=0) is plotted in Figure 4.13. Also, the resultant dose distribution using the SA algorithm and Plaque Simulator for each clinical case are shown in Figure 4.14.

Table 4.8 Percent difference in dose to the fovea (POI 1), optic disc (POI 2), and apex between SA algorithm (SAA) and Plaque Simulator (PS) using uniform and differential loading for various clinical cases.

Clinical case		% difference between dose in SAA and PS		
		POI 1	POI 2	Apex
1	$S_{k,uni}$	0.2	0.9	1.8
	$S_{k,diff}$	1.0	0.5	2.4
2	$S_{k,uni}$	2.4	3.9	5.1
	$S_{k,diff}$	1.2	2.1	4.8
3	$S_{k,uni}$	1.2	3.8	2.5
	$S_{k,diff}$	0.9	1.8	2.3
4	$S_{k,uni}$	0.2	3.3	4.5
	$S_{k,diff}$	0.9	2.0	4.4
5	$S_{k,uni}$	6.9	5.7	4.2
	$S_{k,diff}$	5.2	4.6	3.8
6	$S_{k,uni}$	1.3	4.3	2.4
	$S_{k,diff}$	1.2	3.5	2.4
7	$S_{k,uni}$	2.2	1.5	3.4
	$S_{k,diff}$	0.0	2.1	0.6
8	$S_{k,uni}$	0.8	3.3	2.0
	$S_{k,diff}$	1.4	3.6	1.8
9	$S_{k,uni}$	4.1	6.0	4.9
	$S_{k,diff}$	0.2	2.8	3.4
10	$S_{k,uni}$	0.3	0.8	1.8
	$S_{k,diff}$	3.3	1.8	3.3

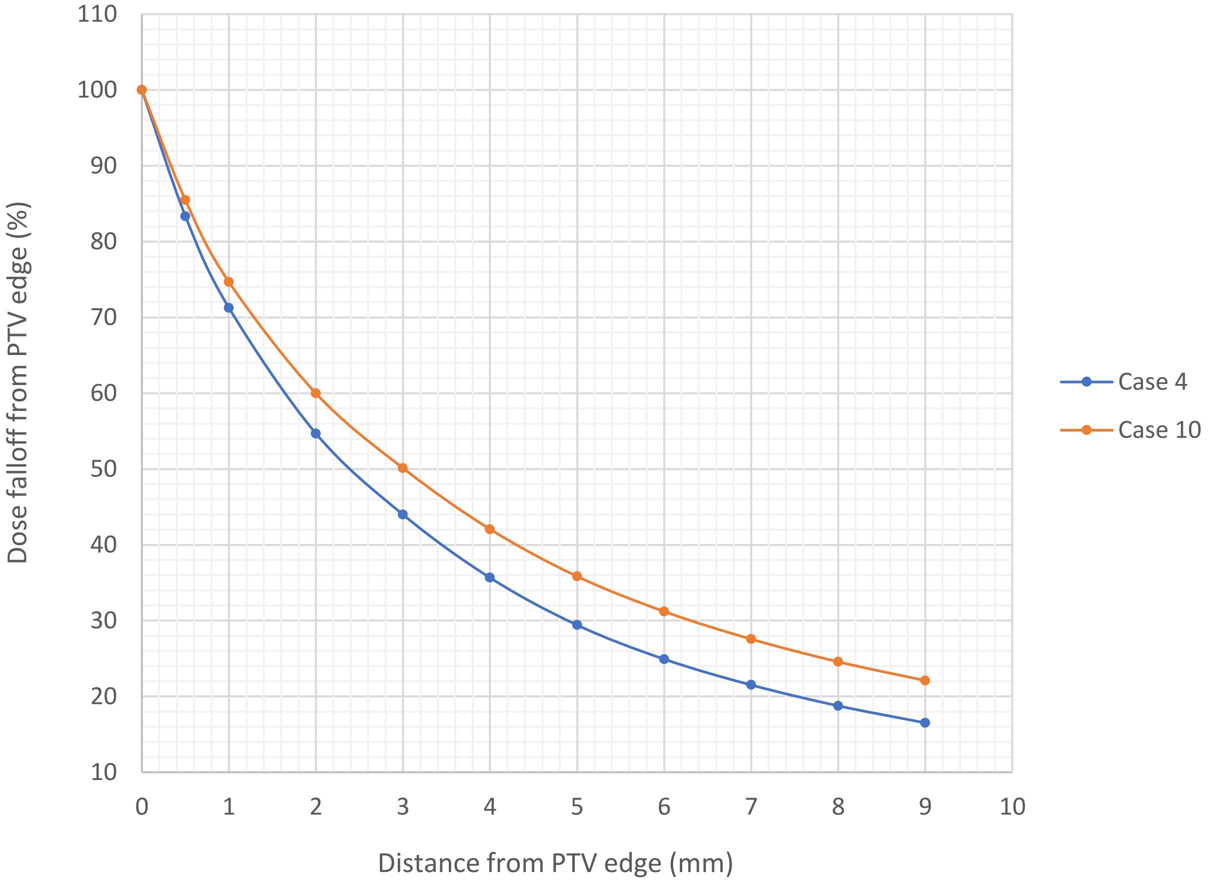

Figure 4.13 Dose falloff relative to dose at PTV edge as a function of distance from PTV edge along the x-axis (at y=0) for Clinical cases 4 (16 mm plaque and $S_{k,uni}$ = 5.68 U) and 10 (22 mm plaque and $S_{k,uni}$ = 6.87 U) using uniform loading.

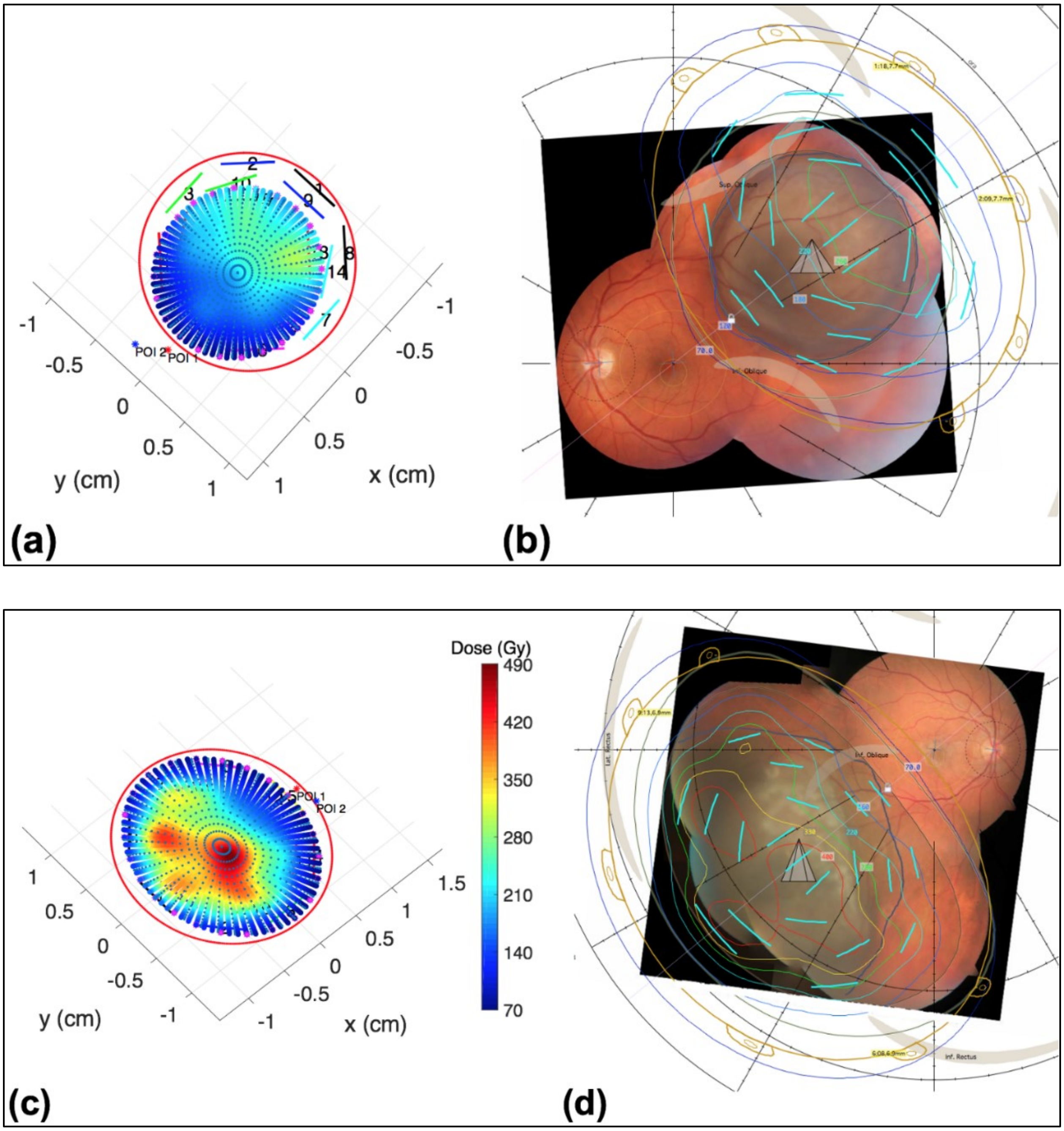

Figure 4.14 The basal dose distribution using the SA algorithm (a,c) and Plaque Simulator (b,d) for Clinical cases (a,b) 5 and (c,d) 10. In Figure 4.14(b) and (d), the indigo line represents the 70 Gy isodose line.

Table 4.8 shows that % differences are mostly within 5%. The potential source of difference is due to the fact that the geometry of the tumor and the critical structures may not have been captured as accurately as in Plaque Simulator. To input the geometry into the SA algorithm, the distance to each critical structure from the PTV edge and the distance between structures were measured using the ruler tool in Plaque Simulator that has an estimated uncertainty of about ±0.05 mm. In addition, since there is a steep dose falloff from the plaque, even a small difference (e.g. 0.1 mm) in distance measurement can cause a large difference in dose to a point. This can be seen in Figure 4.13; for Case 4, the fovea and optic disc is located 2 and 5.5 mm away from the PTV edge, respectively. From Figure 4.13, 0.2 mm represents about 2% (equivalent to 2.1 Gy) difference for the fovea, and about 1% (equivalent to 1.1 Gy) difference for the optic disc. Similarly, for Case 10, the fovea and optic disc is located 2.5 and 5.9 mm away from the PTV edge, respectively. From Figure 4.13, 0.2 mm represents about 2% (equivalent to 2.5 Gy) difference for the fovea, and about 1% (equivalent to 1.2 Gy) difference for the optic disc. This quantitatively shows how sensitively dose changes with distance and therefore the uncertainty in distance measurements may have led to the differences observed in Table 4.8. In Figure 4.14, it can be observed that, for both cases shown, the dose distributions obtained in Plaque Simulator are conformal, covering the entire PTV. Also, the patterns of dose distributions obtained using the SA algorithm are evident in Plaque Simulator. For both methods, the dose distributions are biased towards the opposite side of the critical structures' locations in both cases. Moreover, in Figure 4.14b, the 260 Gy isodose line (green) has an elongated shape and this is also shown for the SA algorithm in Figure 4.14a. The 220 (cyan) and 180 (blue) Gy lines in Plaque Simulator are also visually similar to those obtained by the algorithm. In Figure 4.14d, the distinctive shape of the 400 Gy line (red) matches that for the algorithm in Figure 4.14c. The 220 Gy line (cyan) that is round and wavy towards the POIs is also observed for the algorithm.

In conclusion, the problem of improving sparing of the critical structures of the eye with achieving the full tumor coverage by using differential loading for plaque brachytherapy inverse planning has been investigated. The SA algorithm was applied to solve this particular problem that was tested and verified for various scenarios. First, the developed algorithm was used to reduce dose to a single POI, and then two POIs representing the critical structures; the algorithm was found to be able to reduce doses, to a degree that depends on the tumor and plaque size used. The algorithm was then further developed to handle shifted plaques and elliptical tumor base shapes in its modelling, which have been verified by benchmarking each feature as well as the two together in optimization. Furthermore, by applying the algorithm to numerous clinical scenarios, it was verified that implementing the developed optimization routine into clinical cases is practical.

4.4 References

[1] Wagner A, Chen A, Cook T, Faber D, Winward K, Sause W. Outcomes and control rates for I-125 plaque brachytherapy for uveal melanoma: A community-based institutional experience. *ISRN Ophthalmol.* 2014;2014:1-7.

[2] Jonas RA, Wang YX, Yang H, et al. Optic disc-fovea distance, axial length and parapapillary zones. the beijing eye study 2011. *PloS One*. 2015;10(9):e0138701. doi:10.1371/journal.pone.0138701.

[3] Yao R, Templeton AK, Liao Y, Turian JV, Kiel KD, Chu JC. Optimization for high-dose-rate brachytherapy of cervical cancer with adaptive simulated annealing and gradient descent. *Brachytherapy*. 2014;13(4):352-360.

[4] Ren J, Menon G, Sloboda R. Comparative evaluation of two dose optimization methods for image-guided, highly-conformal, tandem and ovoids cervix brachytherapy planning. *Phys Med Biol*. 2013;58(7):2045-2058.

[5] Wu Q, Mohan R, Niemierko A, Schmidt-Ullrich R. Optimization of intensity-modulated radiotherapy plans based on the equivalent uniform dose. *Int J Radiation Oncology Biol Phys*. 2002;52(1):224-235.

[6] Sauer OA, Shepard DM, Mackie TR. Application of constrained optimization to radiotherapy planning. *Med Phys*. 1999;26(11):2359-2366.

[7] Dowsland KA. Some experiments with simulated annealing techniques for packing problems. *European Journal of Operational Research*. 1993;68(3):389-399.

[8] Azizi N, Zolfaghari S. Adaptive temperature control for simulated annealing: A comparative study. *Computers and Operations Research*. 2004;31(14):2439-2451.

[9] Schneider JJ, Puchta M. Investigation of acceptance simulated annealing — A simplified approach to adaptive cooling schedules. *Physica A: Statistical Mechanics and its Applications*. 2010;389(24):5822-5831.

[10] Chiu-Tsao ST, Astrahan MA, Finger PT, et al. Dosimetry of ^{125}I and ^{103}Pd COMS eye plaques for intraocular tumors: Report of Task Group 129 by the AAPM and ABS. *Med Phys.* 2012;39(10): 6161-6184.

[11] Eye Physics Ver. 6 User Guide. Plaque Simulator. https://www.eyephysics.com/PS/Index.html.

[12] Stewart J. *Essential calculus: Early transcendentals.* 7th ed. Belmont, CA: Thomson Higher Education; 2007.

[13] Thomson RM, Taylor R, Rogers D. Monte carlo dosimetry for I 125 and pd 103 eye plaque brachytherapy. *Med Phys*. 2008;35(12):5530-5543.

[14] Durkin SR, Roos D, Higgs B, Casson RJ, Selva D. Ophthalmic and adnexal complications of radiotherapy. *Acta Ophthalmol Scand*. 2007;85(3):240-250.

[15] Puusaari I, Heikkonen J, Kivela T. Effect of radiation dose on ocular complications after iodine brachytherapy for large uveal melanoma: Empirical data and simulation of collimating plaques. *Invest Ophthalmol Vis Sci*. 2004;45(10):3425-3434.

Chapter 5 Summary, conclusions, and future work

Ocular melanoma, with an incidence rate of about 6 cases per million person-years, is a life threatening cancer due to potential local failures or metastatic spread [1]. Historically, up until 1980s, enucleation was the most common management of ocular melanomas [2]. However, in 1985, the Collaborative Ocular Melanoma Study (COMS) group first provided the standardized methods for administering ocular plaque brachytherapy for treatments of ocular melanomas, and subsequently showed equal survival rates of patients treated with plaque brachytherapy and enucleation [3,4]. As plaque brachytherapy also offered benefits of eye preservation and possible vision retention, it gained favor and started to be used more commonly than enucleation.

In plaque brachytherapy, a metal disc (or plaque) with radioactive seeds is surgically sutured in close proximity to the tumor on the external surface of the eye to irradiate the tumor for a predetermined time period to deliver the required prescription dose. Among various radionuclides available for treatment, low-energy photon emitters such as I-125, are the common choice for plaque brachytherapy treatments due to the low penetration of photons in the surrounding healthy tissues. The work in this thesis was performed using the model IAI-125A seed (IsoAid LLC, Port Richey, FL). Also, this work used the COMS eye plaques, which are constructed such that the radioactive seeds are sandwiched between a gold outer backing and an inner plastic seed carrier (Silastic) [3]. The treatment planning for plaque brachytherapy is performed through several steps. Initially, the tumor dimensions and its position in the eye are determined using various imaging modalities including fundus photography, ultrasound, and CT (or MRI). Information from these images are then input into the treatment planning system (TPS) to generate a treatment plan that calculates the radioactive seed strengths needed to deliver the desired minimum prescription dose, typically to the tumor apex [3,5]. The assembled plaque is then surgically sutured to the eye surface, which is left on for the predetermined treatment time.

Currently plaque brachytherapy planning is performed using the TPS known as Plaque Simulator. When the user inputs into Plaque Simulator the plaque size and placement, prescription depth, prescription dose, and treatment duration, it outputs the required equal seed strength for all seeds to achieve the prescription dose at the tumor apex. As such, in Plaque Simulator, treatment plans are conventionally generated using uniform seed strengths for all seeds within a plaque. However, treating with such a uniformly and fully loaded plaque can result in high doses to the critical structures which may lead to undesirable clinical outcomes. Hence it is often required to modify the treatment plan manually by adjusting the individual seed strengths and locations in the plaque such that the critical structures are spared as much as possible, while still delivering the prescription dose to the tumor. This process requires planning expertise, can be time-consuming, and may not always lead to the best possible plan. The work performed in this thesis aims to provide improvements in plaque brachytherapy treatment planning by applying an automated dose optimization algorithm to overcome the above mentioned challenges. This algorithm will calculate optimal differential seed strengths that can minimize doses to the critical structures while achieving the full tumor coverage. Thus, treatment plans created by the algorithm will provide the potential to increase the chance of preserving the eye as well as vision sparing compared to the conventional manual planning option.

The concept of dose optimization in plaque brachytherapy is addressed in Chapter 2. The American Association of Physicists in Medicine Task Group 43 (TG-43) formalism, which is the consensus standard for photon brachytherapy dose calculations, is described along with the correction factors for plaque heterogeneities [6,7]. Among various optimization methods currently used in radiotherapy, a stochastic method known as simulated annealing (SA) was used in this work, which has the strong advantage of having the capability to escape local minima (e.g. re-injecting heat) in the search for a solution [8]. A general description of the SA algorithm is provided, as well as the past applications of the algorithm in radiotherapy.

The first implementation of the SA algorithm in plaque brachytherapy planning is explored in Chapter 3. To be able to run simulations in the software, tumor and seed geometry were first modelled. Prior to solving the final problem, the SA algorithm was first verified by approaching two general problems: 1) dose optimization using uniform loading, and 2) maximizing dose uniformity across tumor base with differential loading. The first problem allowed to verify the correct implementation of the tumor and seed geometry, dose calculation, and the general steps of the SA algorithm. Using the SA algorithm, uniform seed strengths were obtained and were manually input into Plaque Simulator to compare the resulting dose to apex for various tumor and plaque sizes. The difference in dose to apex between the two systems were found to agree within 4.5% for all scenarios. This difference can be explained by the differences in the values of the TG-43 dosimetry parameters and the COMS seed coordinates used in both systems. The values for the TG-43 dosimetry parameters used in this work are believed to be more accurate due to reasons such as the use of Monte Carlo simulations for every parameter and the fact that the data were taken with a finer resolution. Moreover, the second problem allowed to verify that the algorithm can find minima in the energy function with using differential seed strengths. The algorithm from the first problem was modified to find differential seed strengths that can maximize dose uniformity across the tumor base. Standard deviation in the planning target volume (PTV; tumor + 2 mm margin) basal dose that resulted from using uniform strengths and differential strengths were compared for various tumor dimensions and plaque sizes. Averaging over different plaque sizes, the reduction in basal dose variation for 3.5, 5 and 8 mm heights were found to be 33.1%, 33.3%, and 27.1%, respectively. It was also confirmed from the basal dose distributions, that the basal dose uniformity was significantly improved by using differential loading. For verification, the differential seed strengths obtained by the algorithm were manually input into Plaque Simulator to compare the resulting dose profiles (along the PTV base) and dose to apex. For both systems, the dose profiles were observed to be very similar, as well as doses to apex were close to the prescription dose of 70 Gy (within 0.14 - 5.95%). Therefore, this test problem demonstrated that the algorithm is able to handle differential seed strengths for finding the minima in the energy function, perform dose renormalization for desired dose at tumor apex, as well as impose limits on seed strengths. With these confirmations, the algorithm was considered acceptable for incorporating more complexities to solve the final problem of sparing critical structures with achieving desired tumor coverage.

The final problem of finding differential seed strengths to reduce doses to the critical structures while maintaining desired tumor coverage is investigated in Chapter 4. The SA algorithm was modified to be applied for this particular problem, and the details for the development of the algorithm were provided including the introduction of points of interest (POIs; to represent the critical structures), objective function, and cooling schedule. Up to two POIs were introduced to the system to represent the optic disc and fovea. For having two POIs, the objective function was defined to incorporate an optimization objective dose and weighting factor for each critical structure. This objective function can easily be expanded in the algorithm to optimize for an arbitrary number of POIs. The cooling schedule was set to exponentially decrease with periodic re-injections of heat. For the case of single POI, the algorithm was tested both with and without re-injection of heat. Compared to using uniform strengths, dose to POI was reduced significantly by using differential strengths for the 12 mm plaque size with 5 and 8 mm tumor heights, and 16 mm plaque size with 8 mm tumor height (-29.1±0.0 to -39.7±0.1%). For the rest of the cases tested, reductions were within about 6%; this was because, for these cases, the PTV basal diameter was too large relative to the tumor height such that the 70 Gy isodose line that was just touching the PTV edge could not be pulled further in towards the edge by differentially loading the plaque. When calculating using either with or without re-injection of heat, no difference was observed in the resulting dose reductions and execution times of the algorithm. Hence, optimization with re-injection of heat was used for the rest of this work to keep the algorithm more robust. For the case of two POIs, POIs were placed 4 mm apart from each other and 1 mm from the PTV edge. Similarly, dose to each POI was reduced significantly by using differential strengths for the 12 mm plaque size with 5 and 8 mm tumor heights, and 16 mm plaque size with 8 mm tumor height (-18.8±0.0 to -39.6±0.2%). For the rest of the cases tested, reductions were within about 5%, which was due to the same reason discussed. It was also confirmed that the algorithm is able to work with POIs placed at different locations with respect to the PTV, and with different objective doses and weighting factors for the POIs. With two oppositely placed POIs, the algorithm responded to the user-defined objective doses and weightings by reducing doses only up to the objective values (or up to the lowest possible values when objectives were not achievable), and by yielding a larger reduction for POI with a higher weighting, respectively.

To further improve the capabilities of the optimization routine, additional features including allowing the user to place the plaque off-centre from the tumor base (“plaque shift”) and modelling elliptical tumor base shapes were introduced in the routine. These two features were tested individually, as well as together for optimization. Based on the generated 3D plots of PTV and plaque, correct shifting of the plaque and construction of elliptical tumor base were confirmed. When the two features were tested together, there were significant dose reductions to the two POIs by using differential loading (-19.0±0.9 to -60.8±1.9%), as well as delivery of the minimum prescription dose to the entire PTV.

Finally, in order to verify the practicality of implementation in clinical scenarios, the SA algorithm was applied to 10 anonymized clinical scenarios of previously treated ocular brachytherapy patients. The tumor dimensions and distances of the critical structures relative to the tumor were extracted and input into the algorithm to simulate each case. The differential strengths calculated by the algorithm were then manually input into Plaque Simulator to compare dose to each critical structure and to the apex, and to verify simulation accuracy. For most of the cases tested, the optic disc and fovea doses from Plaque Simulator agreed within 5% to the SA results; there was uncertainty in capturing the geometry of the tumor and the critical structures as accurately as in Plaque Simulator. The PTV basal dose distribution from each system were also found to be visually very similar.

As demonstrated in this study, applying an automated dose optimization algorithm for plaque brachytherapy treatments can improve planning by finding optimal, differential seed strengths that reduce doses to the critical structures of the eye with achieving desired tumor coverage. In the future, this work can be further improved in several aspects. The modelling part of the optimization routine can be improved by further refinements including: enabling it to model non-spherical globes since this work assumed a perfect sphere for the eye, allowing it to import patient CT scans or fundus photos to directly extract the patient geometry, and allowing it to use different plaque and seed types and seed models other than just the COMS plaques and IAI-125A seeds. Dose calculations can be improved by accounting for the air interface in front of the eye and tissue heterogeneities. Moreover, the optimizer can be improved by using a more sophisticated objective function. For example, it can be defined to include multiple optimization objectives for the same POI, such as assigning the optic disc objectives of 60 and 50 Gy, with the former having a larger weight. This way, even if the optimizer achieves the first objective, it would not terminate the optimization but would continue to achieve the second objective. An objective function can also be defined to include more than just POI objectives, such as objectives to minimize basal dose variation, maximum basal dose, or total area bounded by a given isodose line to reduce radiation to the surrounding healthy tissues. Since the optimizer only works with the information provided by the user, if there are other clinical concerns other than just doses to tumor and critical structures (e.g. maximum basal dose), that information will also need to be built into the objective function. Therefore, although using this optimizer does not require as much expertise as the conventional manual planning, choosing objectives and weights for the objective function will still require some expertise. Furthermore, the way the program for the SA algorithm interacts with Plaque Simulator in general can also be improved. Instead of manually extracting patient geometry and inputting seed strengths from the algorithm into Plaque Simulator, this process can also be automated in the future which can eliminate human error, as well as reduce planning time.

A SA algorithm has been developed for automated ocular brachytherapy treatment planning using differential seed strengths. This algorithm and the associated dose calculation model has been benchmarked and characterized. Clinical applicability has been demonstrated, with further future refinements possible.

5.1 References

[1] Weis E, Salopek TG, McKinnon JG, et al. Management of uveal melanoma: a consensus-based provincial clinical practice guideline. *Curr Oncol*. 2016;23(1):e57-64.

[2] Mahendraraj K, Lau C, Lee I, Chamberlain RS. Trends in incidence, survival, and management of uveal melanoma: A population-based study of 7,516 patients from the surveillance, epidemiology, and end results database (1973–2012). *Clinical Ophthalmology*. 2016;10:2113-2119.

[3] Collaborative Ocular Melanoma Study Group. Ch 12: Radiation therapy. In: *COMS manual of procedures.* National Technical Information Service, Springfield, VA; 1995.

[4] Collaborative Ocular Melanoma Study (COMS) Group. The COMS randomized trial of iodine 125 brachytherapy for choroidal melanoma: V. Twelve-year mortality rates and prognostic factors: COMS report no. 28. *Arch Ophthalmol*. 2006;124(12):1684–1693.

[5] The American Brachytherapy Society - Ophthalmic Oncology Task Force. The American brachytherapy society consensus guidelines for plaque brachytherapy of uveal melanoma and retinoblastoma. *Brachytherapy*. 2014;13(1):1-14.

[6] Nath R, Anderson LL, Luxton G, Weaver KA, Williamson JF, Meigooni AS. Dosimetry of interstitial brachytherapy sources: recommendations of the AAPM Radiation Therapy Committee Task Group No. 43. American Association of Physicists in Medicine. *Med Phys.* 1995;22(2):209-234.

[7] Chiu-Tsao ST, Astrahan MA, Finger PT, et al. Dosimetry of ^{125}I and ^{103}Pd COMS eye plaques for intraocular tumors: Report of Task Group 129 by the AAPM and ABS. *Med Phys.* 2012;39(10): 6161-6184.

[8] Kirkpatrick S, Gelatt CD, Vecchi MP. Optimization by simulated annealing. *Science*. 1983;220(4598):671-680.

Bibliography

Acar H, Chiu-Tsao ST, Ozbay I, Kemikler G, Tuncer S. Evaluation of material heterogeneity dosimetric effects using radiochromic film for COMS eye plaques loaded with 125I seeds (model I25.S16). *Med Phys*. 2013;40(1):011708.

Alberta Health Services Uveal melanoma clinical practice guideline CU-015 version 1. ; 2014:1-28.

American Cancer Society. Laser therapy for eye cancer. https://www.cancer.org/cancer/eye-cancer/treating/laser-therapy.html. Updated 2016. Accessed June, 2018.

Aryal P, Molloy JA, Rivard MJ. A modern monte carlo investigation of the TG-43 dosimetry parameters for an 125I seed already having AAPM consensus data. *Med Phys*. 2014;41(2):021702.

Astrahan MA. Improved treatment planning for COMS eye plaques. *Int J Radiat Oncol Biol Phys*. 2005;61(4):1242.

Azizi N, Zolfaghari S. Adaptive temperature control for simulated annealing: A comparative study. *Computers and Operations Research*. 2004;31(14):2439-2451.

Bartlema YM, Oosterhuis JA, Journée-De Korver JG, Tjho-Heslinga RE, Keunen JE. Combined plaque radiotherapy and transpupillary thermotherapy in choroidal melanoma: 5 years' experience. *Br J Ophthalmol*. 2003;87(11):1370-1373.

Beaulieu L, Tedgren AC, Carrier JF, et al. Report of the task group 186 on model-based dose calculation methods in brachytherapy beyond the TG-43 formalism: Current status and recommendations for clinical implementation. *Med Phys*. 2012;39(10):6208-6236.

Bechrakis NE, Petousis V, Willerding G, et al. Ten-year results of transscleral resection of large uveal melanomas: Local tumour control and metastatic rate. *Br J Ophthalmol*. 2010;94(4):460-466.

Bell DJ, Wilson MW. Choroidal melanoma: natural history and management options. *Cancer Control.* 2004;11(5):296-303.

Bortfeld T. Optimized planning using physical objectives and constraints. *Semin Radiat Oncol*. 1999;9(1):20-34.

Canadian Cancer Society. Cancerous tumours of the eye. http://www.cancer.ca/en/cancer-information/cancer-type/eye/eye-cancer/cancerous-tumours/?region=on. Accessed June, 2018.

Canadian Cancer Statistics Advisory Committee. Canadian Cancer Statistics 2018. Toronto, ON: Canadian Cancer Society; 2018. Available at: cancer.ca/Canadian-Cancer-Statistics-2018-EN (accessed [October, 2018]).

Cancer.Net. Cancer types-statistics, https://www.cancer.net/cancer-types, Accessed October, 2018.

Cancer.Net. Eye cancer: Treatment options. https://www.cancer.net/cancer-types/eye-cancer/treatment-options. Updated 2015. Accessed June, 2018.

Chamberland M, Taylor R, Rogers D, Thomson RM. Egs_brachy: A versatile and fast monte carlo code for brachytherapy. *Phys Med Biol*. 2016;61(23):8214-8231.

Char DH, Miller T, Crawford JB. Uveal tumour resection. *Br J Ophthalmol*. 2001;85(10):1213-1219.

Chiu-Tsao ST, Astrahan MA, Finger PT, et al. Dosimetry of ^{125}I and ^{103}Pd COMS eye plaques for intraocular tumors: Report of Task Group 129 by the AAPM and ABS. *Med Phys.* 2012;39(10): 6161-6184.

Collaborative Ocular Melanoma Study (COMS) Group. The COMS randomized trial of iodine 125 brachytherapy for choroidal melanoma: V. Twelve-year mortality rates and prognostic factors: COMS report no. 28. *Arch Ophthalmol*. 2006;124(12):1684–1693.

Collaborative Ocular Melanoma Study Group. Ch 12: Radiation therapy. In: *COMS manual of procedures.* National Technical Information Service, Springfield, VA; 1995.

DeWerd LA, Ibbott GS, Meigooni AS, *et al*. A dosimetric uncertainty analysis for photon-emitting brachytherapy sources: Report of AAPM task group no. 138 and GEC-ESTRO *Med Phys*. 2011;38(2):782-801.

Dias J, Rocha H, Ferreira B, Lopes Mdo C. Simulated annealing applied to IMRT beam angle optimization: A computational study. *Phys Med*. 2015;31(7):747-756.

Dithmar S. Transpupillary thermotherapy. In: Age-related macular degeneration. Springer, Berlin, Heidelberg; 2004:159-167.

Dowsland KA. Some experiments with simulated annealing techniques for packing problems. *European Journal of Operational Research*. 1993;68(3):389-399.

Du KL, Swamy M. Simulated annealing. In: *Search and optimization by metaheuristics.* Switzerland: Birkhäuser; 2016:29-36.

Durkin SR, Roos D, Higgs B, Casson RJ, Selva D. Ophthalmic and adnexal complications of radiotherapy. *Acta Ophthalmol Scand*. 2007;85(3):240-250.

Eckert & Ziegler BEBIG GmbH. Ru-106 eye applicators. https://www.bebig.com/fileadmin/bebig_neu/user_uploads/Products/Ophthalmic_Brachytherapy/Fact_sheet_Ru-106_Eye_Applicators_Rev.05_English.pdf. Accessed October, 2018.

Edge SB, Byrd DR, Compton CC, Fritz AG, Greene FL, Trotti A et al. (eds). Malignant melanoma of the uvea. In: *AJCC Cancer Staging Manual*, 7th edn. Springer: New York, NY, USA, 2010, pp 547–559.

Emami B. Tolerance of normal tissue to therapeutic Radiation. *Rep Radiother Oncol.* 2013;1(1):123-127.

Eye Physics Ver. 6 User Guide. Assembling the ROPES Plaque. https://www.eyephysics.com/PS/PS5/UserGuide/AssembleROPES.html. Accessed October, 2018.

Eye Physics Ver. 6 User Guide. BEBIG plaque information. https://www.eyephysics.com/PS/PS6/UserGuide/BEBIGPlaquesMenu.html. Accessed October, 2018.

Eye Physics Ver. 6 User Guide. Plaque Simulator. https://www.eyephysics.com/PS/Index.html. Accessed May, 2019.

Ezzell GA. Optimization in brachytherapy. *Ch22, AAPM Brachytherapy Society Summer School*, July 2005, Seattle WA; 415-34.

Geman S, Geman D. Stochastic relaxation, gibbs distributions, and the bayesian restoration of images. *Ieee Transactions on Pattern Analysis and Machine Intelligence*. 1984;6(6):721-741.

Georgopoulos M, Zehetmayer M, Ruhswurm I, Toma-Bstaendig S, Segur-Eltz N, Sacu S, Menapace R. Tumour regression of uveal melanoma after Ruthenium-106 brachytherapy or stereotactic radiotherapy with gamma knife or linear accelerator. *Ophthalmologica*. 2003;217(5): 315-319.

Gonsalves CF, Eschelman DJ, Thornburg B, Frangos A, Sato T. Uveal Melanoma Metastatic to the Liver: Chemoembolization With 1,3-Bis-(2-Chloroethyl)-1-Nitrosourea. *AJR Am J Roentgenol.* 2015;205(2):429-433.

Hungerford JL, Foss A, Whelahan I, Errington RD, Kacperek A, Kongerud J. Side effects of photon and proton radiotherapy for ocular melanoma. *Front Radiat Ther Oncol*. 1997;30:287-293.

Jacob D, Raben A, Sarkar A, Grimm J, Simpson L. Anatomy-based inverse planning simulated annealing optimization in high-dose-rate prostate brachytherapy: Significant dosimetric advantage over other optimization techniques. *Int J Radiat Oncol Biol Phys*. 2008;72(3):820-827.

Jonas RA, Wang YX, Yang H, et al. Optic disc-fovea distance, axial length and parapapillary zones. the beijing eye study 2011. *PloS One*. 2015;10(9):e0138701. doi:10.1371/journal.pone.0138701.

Khan FM, Gibbons JP. *Khan's the physics of radiation therapy.* Philadelphia (USA): Williams & Wilkins; 2014. Print.

Kirkpatrick S, Gelatt CD, Vecchi MP. Optimization by simulated annealing. *Science*. 1983;220(4598):671-680.

Krintz A, Hanson WF, Ibbott GS, Followill DS. Verification of plaque simulator dose distributions using radiochromic film [abstract]. *Med Phys*. 2002;29(6):1220-1221.

Kubicky CD, Yeh BM, Lessard E, et al. Inverse planning simulated annealing for magnetic resonance imaging-based intracavitary high-dose-rate brachytherapy for cervical cancer. *Brachytherapy*. 2008;7(3):242-247.

Lessard E, Pouliot J. Inverse planning anatomy-based dose optimization for HDR-brachytherapy of the prostate using fast simulated annealing algorithm and dedicated objective function. *Med Phys*. 2001;28(5):773-779.

Lin AJ, Rao YJ, Acharya S, Schwarz J, Rao PK, Grigsby P. Patterns of care and outcomes of proton and eye plaque brachytherapy for uveal melanoma: Review of the National Cancer Database. *Brachytherapy.* 2017;16(6):1225-1231.

Mahendraraj K, Lau C, Lee I, Chamberlain RS. Trends in incidence, survival, and management of uveal melanoma: A population-based study of 7,516 patients from the surveillance, epidemiology, and end results database (1973–2012). *Clinical Ophthalmology*. 2016;10:2113-2119.

Metropolis N, Rosenbluth AW, Rosenbluth MN, Teller AH, Teller E. Equation of state calculations by fast computing machines. *Journal of Chemical Physics*. 1953;21(6):1087-1092.

Moler CB. *Numerical computing with MATLAB.* Philadelphia: SIAM; 2004.

Morrill SM, Lam KS, Lane RG, Langer M, Rosen II. Very fast simulated reannealing in radiation-therapy treatment plan optimization. *Int J Radiat Oncol Biol Phys*. 1995;31(1):179-188.

Morrison H, Menon G, Larocque MP, *et al.* Initial evaluation of advanced collapsed cone engine dose calculations in water medium for I-125 seeds and COMS eye plaques. *Med Phys*. 2018;45(3):1276-1286.

Morrison H, Menon G, Larocque MP, Veelen B, Niatsetsk Y, Weis E, Sloboda RS. Advanced Collapsed cone Engine dose calculations in tissue media for COMS eye plaques loaded with I-125 seeds. *Med Phys.* 2018;45(7):3349-3360.

Nag S, Quivey JM, Earle JD, Followill D, Fontanesi J, Finger PT; American Brachytherapy Society. The American Brachytherapy Society recommendations for brachytherapy of uveal melanomas. *Int J Radiat Oncol Biol Phys*. 2003;56(2):544-555.

Nath R, Anderson LL, Luxton G, Weaver KA, Williamson JF, Meigooni AS. Dosimetry of interstitial brachytherapy sources: recommendations of the AAPM Radiation Therapy Committee Task Group No. 43. American Association of Physicists in Medicine. *Med Phys.* 1995;22(2):209-234.

NUDAT 2.7, National Nuclear Data Centre, Brookhaven National Laboratory. http://www.nndc.bnl.gov/chart/decaysearchdirect.jsp?nuc=125I&unc=nds. Accessed September, 2018.

Ober M, Servodidio CA, Abramson D. Ocular complications due to cancer treatment. In *Survivors of Childhood and Adolescent Cancer: A Multidisciplinary Approach*. Edited by Schwartz CL, Hobbie WL, Constine LS, Ruccione KS. Heidelberg: Springer; 2005**:**81–94.

Perez BA, Mettu P, Vajzovic L, Rivera D, Alkaissi A, Steffey BA, Cai J, Stinnett S, Dutton JJ, Buckley EG, Halperin E, Marks LB, Mruthyunjaya P, Kirsch DG. Uveal melanoma treated with iodine-125 episcleral plaque: An analysis of dose on disease control and visual outcomes. *Int J Radiat Oncol Biol Phys.* 2014;89(1):127-136.

Poder J, Annabell N, Geso M, Alqathami M, Corde S. ROPES eye plaque dosimetry: commissioning and verification of an ophthalmic brachytherapy treatment planning system. *J Phys: Conf Ser.* 2013;444(1) 012102.

Podgorsak EB. *Radiation oncology physics: A handbook for teachers and students.* Vienna (Austria): International Atomic Energy Agency; 2005. Print.

Puusaari I, Damato B, Kivela T. Transscleral local resection versus iodine brachytherapy for uveal melanomas that are large because of tumour height. *Graefes Arch Clin Exp Ophthalmol*. 2007;245(4):522-533.

Puusaari I, Heikkonen J, Kivela T. Effect of radiation dose on ocular complications after iodine brachytherapy for large uveal melanoma: Empirical data and simulation of collimating plaques. *Invest Ophthalmol Vis Sci*. 2004;45(10):3425-3434.

Radiological Society of North America. Introduction to cancer therapy (radiation oncology). https://www.radiologyinfo.org/en/info.cfm?pg=intro_onco. Updated 2017. Accessed June, 2018.

Rao YJ, Sein J, Badiyan S, Schwarz JK, DeWees T, Grigsby P, Rao PK. Patterns of care and survival outcomes after treatment for uveal melanoma in the post-coms era (2004-2013): a survelliance, epidemiology, and end results analysis. *J Contemp Brachytherapy.* 2017;9(5):453-465.

Ren J, Menon G, Sloboda R. Comparative evaluation of two dose optimization methods for image-guided, highly-conformal, tandem and ovoids cervix brachytherapy planning. *Phys Med Biol*. 2013;58(7):2045-2058.

Ren J. *Implementation of MR image-guided adaptive brachytherapy for cervix cancer* [master's thesis]. Edmonton, Alberta: University of Alberta; 2011.

Rivard MJ, Butler WM, DeWerd LA, *et al*. Supplement to the 2004 update of the AAPM task group no. 43 report. *Med Phys*. 2007;34(6):2187-2205.

Rivard MJ, Chiu-Tsao ST, Finger PT, *et al*. Comparison of dose calculation methods for brachytherapy of intraocular tumors. *Med Phys*. 2011;38(1):306-316.

Rivard MJ, Coursey BM, DeWerd LA, *et al*. Update of AAPM task group no. 43 report: A revised AAPM protocol for brachytherapy dose calculations. *Med Phys*. 2004;31(3):633-674.

Rogers K. *The eye: The physiology of human perception (the human body), 1st ed.* New York, NY: Britannica Educational Publishing; 2011.

Sauer OA, Shepard DM, Mackie TR. Application of constrained optimization to radiotherapy planning. *Med Phys*. 1999;26(11):2359-2366.

Schneider JJ, Puchta M. Investigation of acceptance simulated annealing — A simplified approach to adaptive cooling schedules. *Physica A: Statistical Mechanics and its Applications*. 2010;389(24):5822-5831.

Scoccianti S, Detti B, Gadda D, Greto D, Furfaro I, Meacci F, Simontacchi G, Brina LD, Bonomo P, Giacomelli I, Meattini I, Mangoni M, Cappelli S, Cassani S, Talamonti C, Bordi L, Livi L. Organs at risk in the brain and their dose-constraints in adults and in children: A radiation oncologist's guide for delineation in everyday practice. *Radiother Oncol.* 2015;114(2):230-238.

Shepard D. IMRT optimization algorithms. *The American Association of Physicist in Medicine (AAPM)* [Available: https://www.aapm.org/meetings/amos2/pdf/49-14369-92189-877.pdf]. 2007.

Shields JA, Shields CL. *Intraocular tumors: An atlas and textbook, 3rd ed.* Philadelphia, PA: Wolters Kluwer, Lippincott Willians & Wilkins; 2015.

Sloboda RS. Optimization of brachytherapy dose distributions by simulated annealing. *Med Phys*. 1992;19(4):955-964.

Solberg TD, DeMarco JJ, Hugo G, Wallace RE. Dosimetric parameters of three new solid core I-125 brachytherapy sources. *J Appl Clin Med Phys*. 2002;3(2):119-134.

Stannard C, Sauerwein W, Maree G, Lecuona K. Radiotherapy for ocular tumours. *Eye (Lond)*. 2012;27(2):119-27.

Stewart J. *Essential calculus: Early transcendentals.* 7th ed. Belmont, CA: Thomson Higher Education; 2007.

Tarlan B, Kıratlı H. Uveal Melanoma: Current Trends in Diagnosis and Management. *Turk J Ophthalmol*. 2016;46(3):123-137.

Taylor REP, Rogers DWO. An EGSnrc Monte Carlo-calculated database of TG-43 parameters. *Med Phys*. 2008;35:4228–4241.

Taylor REP, Rogers DWO. The CLRP TG-43 parameter database for brachytherapy. http://www.physics.carleton.ca/clrp/seed_database. Accessed March 31, 2019.

The American Brachytherapy Society - Ophthalmic Oncology Task Force. The American brachytherapy society consensus guidelines for plaque brachytherapy of uveal melanoma and retinoblastoma. *Brachytherapy*. 2014;13(1):1-14.

Thomson RM, Taylor R, Rogers D. Monte carlo dosimetry for I 125 and pd 103 eye plaque brachytherapy. *Med Phys*. 2008;35(12):5530-5543.

University of California, San Francisco (UCSF), Department of Radiation Oncology. Inverse planning simulated annealing (IPSA). https://radonc.ucsf.edu/inverse-planning-simulated-annealing-ipsa. Updated 2015. Accessed January 23, 2019.

Wagner A, Chen A, Cook T, Faber D, Winward K, Sause W. Outcomes and control rates for I-125 plaque brachytherapy for uveal melanoma: A community-based institutional experience. *ISRN Ophthalmol.* 2014;2014:1-7.

Webb S. Optimization by simulated annealing of three- dimensional conformal treatment planning for radiation fields defined by a multileaf collimator. *Phys Med Biol*. 1991;36(9):1201-1235.

Weis E, Salopek TG, McKinnon JG, et al. Management of uveal melanoma: a consensus-based provincial clinical practice guideline. *Curr Oncol*. 2016;23(1):e57-64.

Weisstein EW. *CRC concise encyclopedia of mathematics * 2nd ed. CRC Press; 2002:875-876.

Wilson MW, Hungerford JL. Comparison of episcleral plaque and proton beam radiation therapy for the treatment of choroidal melanoma. *Ophthalmology*. 1999;106(8):1579-1587.

Wu Q, Mohan R, Niemierko A, Schmidt-Ullrich R. Optimization of intensity-modulated radiotherapy plans based on the equivalent uniform dose. *Int J Radiation Oncology Biol Phys*. 2002;52(1):224-235.

Yaghini M. Simulated annealing part 1: Basic concepts. http://webpages.iust.ac.ir/yaghini/Courses/AOR_881/Simulated%20Annealing_01.pdf. Updated 2009. Accessed March 30, 2019.

Yang J, Manson DK, Marr BP, Carvajal RD. Treatment of uveal melanoma: where are we now?. *Ther Adv Med Oncol*. 2018;10:1758834018757175. Published 2018 Feb 21. doi:10.1177/1758834018757175.

Yao R, Templeton AK, Liao Y, Turian JV, Kiel KD, Chu JC. Optimization for high-dose-rate brachytherapy of cervical cancer with adaptive simulated annealing and gradient descent. *Brachytherapy*. 2014;13(4):352-360.

Zhang H, Davidorf F, Qi Y, Comparison of 16 mm OSU-Nag and COMS eye plaques. *J Appl Clin Med Phys.* 2012;13(3):166-178.

Zhang H, Martin D, Chiu-Tsao ST, Meigooni A, Thomadsen BR. A comprehensive dosimetric comparison between 131Cs and 125I brachytherapy sources for COMS eye plaque implant. *Brachytherapy*. 2010;9(4):362-372.

Zimmermann LW, Amoush A, Wilkinson DA. Episcleral eye plaque dosimetry comparison for the Eye Physics EP917 using Plaque Simulator and Monte Carlo simulation. *J Appl Clin Med Phys*. 2015;16(6):226-239.